Hydrogen Storage Performance of Graphitic Carbon Nitride(g-C_3N_4) Nanotubes

by

Ruiran Guo

A thesis submitted for the Degree of

Master of Engineering

School of Materials Science and Engineering

Faculty of Science

the University of New South Wales

January 2021

Thesis Title

Hydrogen Storage Performance of Graphitic Carbon Nitride(g-C_3N_4) Nanotubes

Thesis Abstract

21st century is the hydrogen century. However, to realize hydrogen economy the safe and effective hydrogen storage remains one of the main challenges. In this work, graphitic carbon nitride (g-C_3N_4) nanotubes were synthesised through a convenient one-step calcination method. The physical, chemical and hydrogen storage properties were examined. For comparison, multiwall carbon nanotubes (MWCNTs) and g-C_3N_4 nanosheets and bulk g-C_3N_4 were also studied. While the MWCNTs were purchased from Shenzhen Nanotech Port Co., Ltd, China, bulk g-C_3N_4 was synthesised by calcined melamine at 550 °C following a route in the literature. A novel and facile high temperature calcination method was proposed and developed here to synthesize g-C_3N_4 nanosheets.

All the g-C_3N_4 materials (nanotubes, nanosheets and bulk) possessed better performance in hydrogen storage than the MWCNTs. The hydrogen storage capacities of the materials studied were obtained at 25 °C (room temperature) and under a hydrogen pressure of 3.7 MPa. For g-C_3N_4 nanotubes, the hydrogen storage capability has improved by up to 70% (from 0.46 wt.% for MWCNTs to 0.78 wt.%. The 25 °C hydrogen storage capacity of bulk g-C_3N_4 (0.51 wt.%) was also higher than that of MWCNTs. The capacity of g-C_3N_4 nanosheets (0.73 wt.%) was higher than that of bulk g-C_3N_4, but lower than the capacity of g-C_3N_4 nanotubes. The higher calculated isosteric heat of adsorption (Q_{st}) for the three g-C_3N_4 materials (8.5 kJ/mol for bulk, 10.5 kJ/mol for nanosheets and 12.5 kJ/mol for nanotubes) as compared to that of MWCNTs (6 kJ/mol) implies that the high storage capacities could be attributed to the strong interaction between hydrogen and the g-C_3N_4 materials. Besides, Q_{st} of g-C_3N_4 nanotubes was higher than Q_{st} of g-C_3N_4 nanosheets and bulk g-C_3N_4, suggesting that g-C_3N_4 nanotubes could form a much stabler bond with hydrogen. This finding can be used to explain the highest storage capacity of g-C_3N_4 nanotubes as compared with that of g-C_3N_4 nanosheets and bulk g-C_3N_4. Temperature Programming Desorption (TPD) was also applied to study the four samples. Strong signals were detected for the chemisorbed hydrogen in g-C_3N_4 materials, suggesting except physisorption, chemisorption should also play an important role in the great hydrogen storage performance of them.

In the second part of this work, nickel was used in the fabrication of g-C_3N_4 nanotubes, in an attempt to further improve the hydrogen storage performance. The samples were synthesized by calcining melamine, cyanuric acid, and nickel together. The obtained g-C_3N_4 nanotubes possessed a highly defective and porous nanotube structure. Consequently, the specific surface area and pore volume have largely improved. Compared with g-C_3N_4 nanotubes synthesized without using nickel, the 25 °C storage capacity of g-C_3N_4 nanotubes synthesized by nickel-assisted approach has further increased by 50% (from 0.78 wt.% to 1.17 wt.%). As confirmed by hydrogen desorption study and Temperature Programming Desorption (TPD) experiments, the improved capacity could be attributed to the increased physisorption and chemisorption of hydrogen in the nanotubes. Based on this finding, it could be concluded that the created defects and pores provided extra strong adsorption sites for hydrogen, which enabled more hydrogen to be adsorbed, either physically or chemically.

In summary, this work is one of the first to study g-C_3N_4 nanotubes for hydrogen storage through the experimental methods. Evidence showed that g-C_3N_4 nanotubes could be a potential material for hydrogen storage application at room temperature. A facile, one step fabrication method was disclosed in this work which could be used to synthesize porous g-C_3N_4 nanosheets with high specific surface area and pore volume. The as synthesized g-C_3N_4 nanosheets not only had the advantage for hydrogen storage, but also could be expected to have good performance in other fields like photocatalyst. In addition, this research reported a nickel based modification method to create defects and pores on g-C_3N_4 nanotubes. This methodology should pave a new avenue to modify g-C_3N_4 based materials for advanced applications like photocatalyst, solar cell and lithium battery.

Acknowledgement

Firstly, I want to thank my supervisor Prof. Sammy Chan who offered me this opportunity to do the wonderful research project on the topic" Fabrication and Characterization of Hydrogen Storage Materials Made by Graphitic Carbon Nitride Nanotubes" so that I could learn a lot of new knowledge and master new research skills. I am also truly grateful to him for the support throughout my study. Without his precious guidance, advice, and patience, I cannot finish my research and complete this thesis. I am really thankful to him.

Secondly, I am deeply grateful to my family especially my mother and father. My mother called me almost every day, so I did not feel lonely. They always support me, love me, and encourage me throughout my life.

Thirdly, I would like to thank Yin and Richard from EMU, UNSW Sydney who helped me with the operation of SEM and TEM. I also want to thank associate professor Jason Anthony Scott from UNSW Sydney, for his kind assistance on the temperature programming desorption (TPD) experiment.

My thanks also go to my group members: Johnson, Ghazal, Ilizel, Yansong, Zhaoyue, Xin , Yaming for the experimental assistants and encouragement. I would like to thank Ilizel, Zhaoyue and Johnson especially for their kind advice and help on the operation of PCI machine and the data interpretation.

Finally, I would like to thank my friend and roommate Jiawen. Without his accompanying, I would not have accomplished my master study successfully.

This thesis is dedicated to my family.

Abstract

21st century is the hydrogen century. However, to realize hydrogen economy the safe and effective hydrogen storage remains one of the main challenges. In this work, graphitic carbon nitride (g-C_3N_4) nanotubes were synthesised through a convenient one-step calcination method. The physical, chemical and hydrogen storage properties were examined. For comparison, multiwall carbon nanotubes (MWCNTs) and g-C_3N_4 nanosheets and bulk g-C_3N_4 were also studied. While the MWCNTs were purchased from Shenzhen Nanotech Port Co., Ltd, China, bulk g-C_3N_4 was synthesised by calcined melamine at 550 °C following a route in the literature. A novel and facile high temperature calcination method was proposed and developed here to synthesize g-C_3N_4 nanosheets.

All the g-C_3N_4 materials (nanotubes, nanosheets and bulk) possessed better performance in hydrogen storage than the MWCNTs. The hydrogen storage capacities of the materials studied were obtained at 25 °C (room temperature) and under a hydrogen pressure of 3.7 MPa. For g-C_3N_4 nanotubes, the hydrogen storage capability has improved by up to 70% (from 0.46 wt.% for MWCNTs to 0.78 wt.%. The 25 °C hydrogen storage capacity of bulk g-C_3N_4 (0.51 wt.%) was also higher than that of MWCNTs. The capacity of g-C_3N_4 nanosheets (0.73 wt.%) was higher than that of bulk g-C_3N_4, but lower than the capacity of g-C_3N_4 nanotubes. The higher calculated isosteric heat of adsorption (Q_{st}) for the three g-C_3N_4 materials (8.5 kJ/mol for bulk, 10.5 kJ/mol for nanosheets and 12.5 kJ/mol for nanotubes) as compared to that of MWCNTs (6 kJ/mol) implies that the high storage capacities could be attributed to the strong interaction between hydrogen and the g-C_3N_4 materials. Besides, Q_{st} of g-C_3N_4 nanotubes was higher than Q_{st} of g-C_3N_4 nanosheets and bulk g-C_3N_4, suggesting that g-C_3N_4 nanotubes could form a much stabler bond with hydrogen. This finding can be used to explain the highest storage capacity of g-C_3N_4 nanotubes as compared with that of g-C_3N_4 nanosheets and bulk g-C_3N_4. Temperature Programming Desorption (TPD) was also applied to study the four samples.

Strong signals were detected for the chemisorbed hydrogen in g-C_3N_4 materials, suggesting except physisorption, chemisorption should also play an important role in the great hydrogen storage performance of them.

In the second part of this work, nickel was used in the fabrication of g-C_3N_4 nanotubes, in an attempt to further improve the hydrogen storage performance. The samples were synthesized by calcining melamine, cyanuric acid, and nickel together. The obtained g-C_3N_4 nanotubes possessed a highly defective and porous nanotube structure. Consequently, the specific surface area and pore volume have largely improved. Compared with g-C_3N_4 nanotubes synthesized without using nickel, the 25 $^{\circ}$C storage capacity of g-C_3N_4 nanotubes synthesized by nickel-assisted approach has further increased by 50 % (from 0.78 wt.% to 1.17 wt.%). As confirmed by hydrogen desorption study and Temperature Programming Desorption (TPD) experiments, the improved capacity could be attributed to the increased physisorption and chemisorption of hydrogen in the nanotubes. Based on this finding, it could be concluded that the created defects and pores provided extra strong adsorption sites for hydrogen, which enabled more hydrogen to be adsorbed, either physically or chemically.

In summary, this work is one of the first to study g-C_3N_4 nanotubes for hydrogen storage through the experimental methods. Evidence showed that g-C_3N_4 nanotubes could be a potential material for hydrogen storage application at room temperature. A facile, one step fabrication method was disclosed in this work which could be used to synthesize porous g-C_3N_4 nanosheets with high specific surface area and pore volume. The as synthesized g-C_3N_4 nanosheets not only had the advantage for hydrogen storage, but also could be expected to have good performance in other fields like photocatalyst. In addition, this research reported a nickel based modification method to create defects and pores on g-C_3N_4 nanotubes. This methodology should pave a new avenue to modify g-C_3N_4 based materials for advanced applications like photocatalyst, solar cell and lithium battery.

Table of Contents

Chapter 1 Introduction

1.1 Introduction

Hydrogen, which possesses a high gravimetric energy density and produces energy with zero carbon dioxide emission, is regarded as a potential alternative to fossil fuels. However, to realize a hydrogen economy, we must solve the challenging problems associated with effective hydrogen storage. [1]. Until now, the most common three methods to store hydrogen are: high pressure hydrogen storage; liquifying hydrogen and storing hydrogen in solid-state materials. For the first two methods, safety issue and temperature limit exist [2] and promote intense research on suitable materials to store hydrogen efficiently. Among these materials, metal-based materials like AB_2, AB_3 and AB_5, which form metal hydride, are reported to have a large storage capacity for hydrogen. For example, magnesium and its alloys can even store hydrogen to above 7 wt.% [3]. However, the low kinetic of hydrogen sorption and high temperature (>300 ℃) required for hydrogen release still severely limit their practical use as a hydrogen storage material [4,5].

Carbon nanotubes (CNTs) with a unique 1D structure has been largely studied as a potential hydrogen storage material. It has been found that CNT could store hydrogen above 5 wt.% at 77 K under 20 bar [6]. But the hydrogen storage capacity at room temperature is very low because of the low isosteric heat of adsorption (normally 5 kJ/mol) [7]. One way to improve the storage capacity is to introduce heteroatom nitrogen, which could increase the binding energy between hydrogen molecule/atom and the adsorbent [8]. One of the theories to explain why nitrogen could increase binding energy is that nitrogen reduces the energy barrier of dissociative adsorption of hydrogen [9,10]. Another theory is that heteroatom induces the dipole moment in the hydrogen then the interaction between hydrogen and storage materials is strengthened [11-13]. It should be noted that the doped nitrogen on carbon materials were usually

below 30 wt.% for most of reported research. Thus, it would be of interest to see if an increase in nitrogen content > 30 % would give rise to better results in hydrogen storage.

Graphitic carbon nitride (g-C_3N_4) nanotubes having a graphitic tubular structure like CNT, is widely used in the field of photocatalyst, lithium battery and solar cell [14-16]. Because of the high concentration of nitrogen (57 % in theory), g-C_3N_4 nanotubes can be expected to have good performance in hydrogen storage. Another advantage of g-C_3N_4 nanotubes is their porous structure. Compared with carbon materials, there is nitrogen induced defects (about 0.7 nm) on the graphitic structure of g-C_3N_4 materials [17]. Figure 1 shows the nanostructure of g-C_3N_4 nanotubes and nanosheets which have lots of nanopores. Koh et al. reported that these nanopores could allow hydrogen to get into the interior of nanotubes, thus increased the specific surface area and stored hydrogen within [17]. In addition, the doubly bonded nitrogen at the nanopores can be strong physical or chemical sites for hydrogen adsorption. The theoretical hydrogen storage capacity of g-C_3N_4 nanotubes has been calculated to be 5.45 wt.% [17]. It is to my knowledge that the hydrogen storage performance of g-C_3N_4 nanotubes has not been widely studied by experiment method. Therefore, a comprehensive experimental research is needed to investigate the potential of g-C_3N_4 nanotubes as hydrogen storage materials.

For most of studies, g-C_3N_4 nanotubes were synthesised through a two-step condensation method [18-20]. To be more specific, melamine or the mixture of melamine and cyanuric acid are subjected to hydrothermal reaction firstly, then the products after hydrothermal reaction are calcined at a certain temperature. However, this method always suffers from the shortcomings such as low yield and time consuming. Other fabrication routes such as solvothermal treatment, catalyst-assembly, template, or chemical vapor deposition have been reported [21-24]. However, they have many drawbacks including unstable yield and quality, harsh synthesis conditions, using toxic chemicals, complicated procedures, and high cost [25]. Thus, an easy to handle, high yield and environmental-friendly method is needed to fabricate g-C_3N_4 nanotubes. Recently,

Wang et al. successfully synthesised g-C_3N_4 nanotubes through a convenient route by heating cyanuric acid and melamine together. The as-synthesised materials have perfect nanotube structure and high yield [26]. Therefore, the reported method has been employed here to fabricate samples for hydrogen storage study, with a minor adjustment which is discussed in detail in Chapter 3.

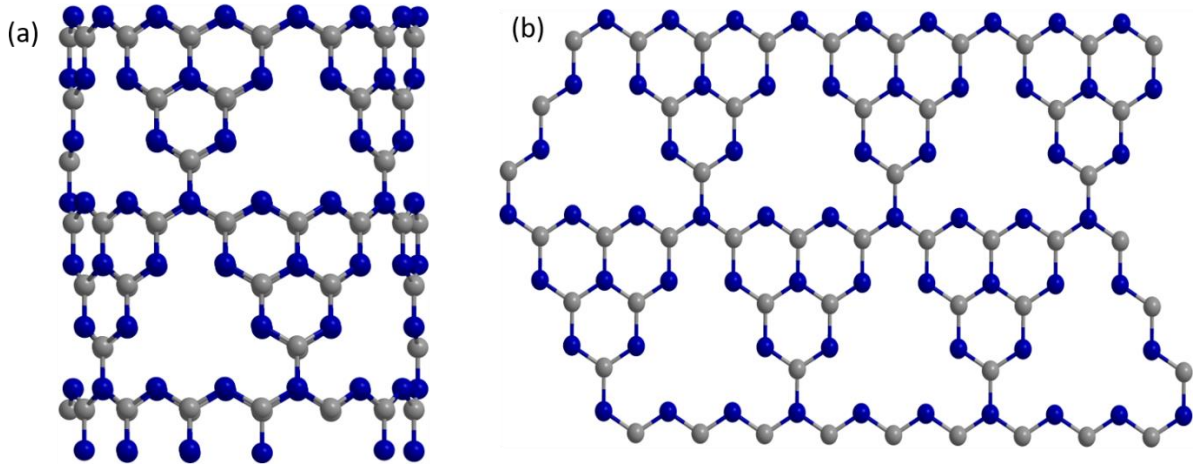

Figure 1.1. nanostructure of (a) g-C_3N_4 nanotubes and (b) g-C_3N_4 nanosheets.

According to Wang's study, the precursor materials melamine and cyanuric acid started to form nanorod structure at about 400 ˚C during the synthesis process, then the nanorod structure transformed to g-C_3N_4 nanotubes at about 550 ˚C by removing the -NH_2 groups on the edge of tri-s-triazine [26,27]. Since the removing process can release toxic NH_3 gas, it is necessary to improve the synthesis method to reduce the release of NH_3 gas. Decomposing NH_3 gas seems to be a plausible way to achieve this. Here nickel nitride could be synthesised through the reaction between nickel (Ni) and NH_3 [28-31] following the reaction $6Ni+2NH_3=2Ni_3N+3H_2$. Thus, using nickel should be a good way to reduce the released NH_3 gas. There is another benefit of using nickel to decompose NH_3. H_2 produced by this reaction could have the chance to react with oxygen and form H_2O molecules. The size of H_2O molecules (0.25 nm) is smaller than the interlayer distance of g-C_3N_4 (0.324 nm) [32]. It is easy

for H_2O to intercalate into the walls of g-C_3N_4 nanotubes and trigger the C/N-reforming reactions: $CN+2H_2O=CO+2H_2+NO$ [32,33], which can create defects on g-C_3N_4 nanotubes. Thus, the surface area largely increases accordingly. It is apparent that the surface area of synthesized g-C_3N_4 nanotubes in most reported research was not very high, and the reported method to fabricate high surface area nanotubes was very complex [18-24]. Until now, this easy modification method was not applied to g-C_3N_4 nanotubes yet. Therefore, it is very important to investigate whether the addition of nickel is beneficial in modifying the structure of g-C_3N_4 nanotubes.

1.2 Objectives

In this work, g-C_3N_4 nanotubes was synthesized through a convenient one-step thermal polycondensation method by directly heating melamine and cyanuric acid with a specific mass ratio. Multiwall carbon nanotubes (MWCNTs), bulk g-C_3N_4 and g-C_3N_4 nanosheets have been studied for comparison. The morphology was studied by transmission electron microscopy (TEM) and scanning electron microscopy (SEM). The structure information was collected on X-ray diffraction (XRD). The surface information was studied by N_2 adsorption/desorption isotherms. The chemical composition was studied by X-ray photoelectron spectroscopy (XPS) and Fourier transform Infrared (FTIR) spectra. The hydrogen storage performance was investigated at different temperatures and at 3.7 MPa. The isosteric heat of adsorption (Q_{st}) was calculated and temperature programming desorption (TPD) was applied to study chemisorption in the materials. There are three specific objectives for the study of hydrogen storage performance on g-C_3N_4 nanotubes and the three comparative materials g-C_3N_4 nanosheets, bulk g-C_3N_4 and MWCNTs:

1. To study the hydrogen adsorption/desorption on g-C_3N_4 nanotubes, g-C_3N_4 nanosheets, bulk g-C_3N_4 and MWCNTs at different temperature.

2. To determine the hydrogen adsorption mechanisms of g-C_3N_4 nanotubes, g-C_3N_4 nanosheets, bulk g-C_3N_4 and MWCNTs.

3. Using the chemical and structure information obtained from characterizations and the relative adsorption mechanisms, to explain the hydrogen adsorption/desorption performance of g-C_3N_4 nanotubes, g-C_3N_4 nanosheets, bulk g-C_3N_4 and MWCNTs.

Nickel was used to fabricate g-C_3N_4 nanotubes. The microstructure, chemical composition, surface information and hydrogen storage performance of the Ni-g-C_3N_4 nanotubes were studied. There are three specific objectives for the study of Ni-g-C_3N_4 nanotubes:

1. To do the comparative study on the microstructure, chemical composition, and specific surface area/pore volume of Ni-g-C_3N_4 nanotubes and normal g-C_3N_4 nanotubes fabricated without using nickel.

2. To do the comparative study on the hydrogen adsorption/desorption behaviour on Ni-g-C_3N_4 nanotubes and normal g-C_3N_4 nanotubes at different temperature.

3. To determine the hydrogen adsorption mechanisms of Ni-g-C_3N_4 nanotubes.

4. Using the obtained information (chemical composition, microstructure, specific surface area/pore volume and adsorption mechanisms) to explain the hydrogen adsorption/desorption performance of Ni-g-C_3N_4 nanotubes.

1.3 Thesis Structure

Chapter 1: This chapter is the introduction of the work which presents the challenge of achieving hydrogen economy; the reason of studying g-C_3N_4 nanotubes for hydrogen storage and the method(s) chosen to fabricate g-C_3N_4 nanotubes. The objectives of the research, as well as the scope, have been identified.

Chapter 2: It is the chapter on literature review, giving the background information of this research and details on hydrogen storage technology. The fabrication and the hydrogen storage applications of g-C_3N_4 nanotubes are also discussed.

Chapter 3: Chapter 3 describes the experimental of the present work. It provides a detailed description on the fabrication method of bulk g-C_3N_4, g-C_3N_4 nanotubes, g-C_3N_4 nanosheet and Ni-g-C_3N_4 nanotubes. It also discusses the characterization methods used in this study, and the work principle of high-pressure Sievert instrument for hydrogen storage.

Chapter 4: Experiment results and discussion are discussed in this chapter. The morphology, microstructure, chemical composition, surface information of g-C_3N_4 nanotubes MWNCTs, bulk g-C_3N_4 and g-C_3N_4 nanosheets were presented. The hydrogen storage performances of g-C_3N_4 nanotubes Ni-g-C_3N_4 nanotubes were studied, compared, and discussed. The adsorption mechanism behind they hydrogen storage was proposed.

Chapter 5: This part is the conclusion of this study. Future work is also provided.

Chapter 2 Literature Review

2.1 Introduction

Energy, which can be found from water, soil, or fire, is the requirement for the development of human being. Many years ago, people knew how to roast meat with fire. This is the original way by which people got and used energy. In eighteenth century, Watt improved and spread steamers which could transform thermal energy to kinetic energy. By burning coals or fossil fuels, water receives enough heat and reaches the boiling point so it becomes steam, the steam then pushes the pistons to drive other machines. This marvellous innovation helped people have a better live since it improved the efficiency. And it was the first-time people began to use energy from fossil fuels effectively for development. After eighteenth century, the use of other fossil fuels like natural gas and oil started.

Energy is essential for civilization. Today nations' development relies heavily on energy especially from fossil fuels. Fossil fuels includes coal, oil, and natural gas. The more advanced and developed countries are, the more energy they need to extract mostly from fossil fuels which will be used for cooking, heating, and other parts of people's life [34]. For example, the developed countries in North America or Europe input and excavate cheap coals or oil to support the technology development and daily consumption in transportation and electricity. So, there will be a higher rate of energy consumption and demand for fossil fuels. For other less developed countries like African countries or some Asian countries, they rely less on fossil fuels to support machines, vehicles, or infrastructures. So, there is less demand for energy or

for fossil fuels. However, developing countries such as China and India are having one of the highest rate of consumption of fossil fuels owing to their large population.

Figure 2.1 shows the world primary energy consumption from 1950 to 2050 [35]. The growing population and increasing standard of lifestyle have caused a growing rate of consumption of fossil fuels or other energy from 1950. It can be clearly seen that the consumption of fossil fuels such as oil, natural gas and coal is below 2000 million metric ton of oil equivalent (Mtoe)in 1950 but reaches 4000,7900 and 12000 Mtoe in 2010, respectively. 2035 Mtoe was predicted to be the turning point when the demand of fossil fuel starts to decrease. Now, many countries has begun to consider solutions for energy security since fossil fuels are non-renewable energy [2]. Fossil fuels will be used up, even if there is still large reserves of available coals or natural gas. It is unlikely to happen in the next fifty years. However, according to the research, if countries keep the high rate of consumption, the reserves of coal or natural gas will only last for about 200 and 70 years, respectively. Oil will be exhausted earlier [36].

Another issue about widely harnessing and using fossil fuels is greenhouse gas emission. Scientists have concerned about the large amount of CO_2 emission and the influence of CO_2

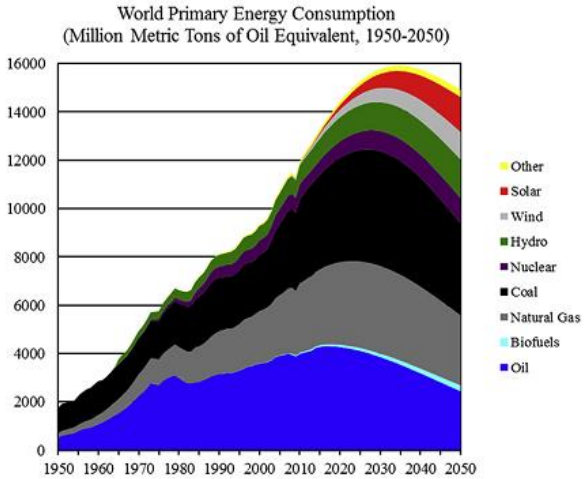

Figure 2.1. World primary energy consumption [2].

on our environment. The large amount of CO_2 will lead to greenhouse effect which can cause global warming [34,37]. The ice at polar regions has already begun to melt because of global warming and resulted in the increase of sea level at an alarming rate, causing a serious threat to the island countries. The main contribution of the emission of CO_2 is due to the burning of fossil fuels. Therefore, for the reason of sustainable development, the research on renewable and clean energy which can act as the alternatively energy for fossil fuels is urgently needed.

Until now, there have been a large amount of research about clean and renewable energy such as solar, tidal, wind and geothermal energy [38]. Solar and wind energy are two types of energy that have been studied for many years. Some relative applications also appeared before public. In Holland, government has already set lots of windmills which can gather wind energy and supply electricity for household applications. The solar energy-based power equipment has been used in some countries. Tidal energy is gotten from ocean whereas geothermal energy is harnessed from the magma or hot liquid within the earth crust. Even if all of them are renewable energy, some fatal drawbacks truly limit their wide application. For solar energy and wind energy, they largely depend on the weather condition. And for tidal and geothermal energy, they can only be harnessed at certain locations. More important, it is very hard to transport and store the four types of energy [39].

For these reasons, scientists have been focusing on the research of hydrogen fuelled technology in recent years. Toyota has developed cars driving by hydrogen, Figure 2.2 shows the picture of the cars [40,41]. Hydrogen is promising energy and has been regarded as one of the best alternatives for fossil fuels in the future. There are some advantages why hydrogen is ideal and expected:

1. The element of hydrogen is very common and abundant in nature. The current technologies enable us to extract hydrogen easily from water or other chemicals by means of

electrolysis and pyrolysis [42].

2. The energy density of hydrogen is higher than 120 MJ/kg which is five times higher than gasoline. According to the calculation, five-kilogram hydrogen can drive a light-duty car for about five hundred kilometres [43-45].

3. Hydrogen is non-toxic and gives no influence on the environment. After combustion of hydrogen, the products are water and heat. The water produced can be reused to get hydrogen .

4. Compared with solar, wind, tidy and geothermal energy, it is much easy to use the energy in hydrogen since hydrogen can be stored and transport [46].

Figure 2.2, The car driving by hydrogen made by Toyota[40,41].

2.2 Hydrogen Storage Technology

There are three aspects of hydrogen economy including hydrogen production, hydrogen storage and hydrogen transportation [34]. However, the bottleneck of hydrogen economy is the deficiency in safe and effective hydrogen storage technology. The U.S. Department of Energy

(DOE) benchmark of hydrogen storage system in vehicle applications is illustrated in Figure 2.3 [47]. This target is focused on the demand of applications instead of the projected capacities of storage technologies. One challenge is to overcome a driving range of 500 km for most light-duty vehicles [48]. More details related to the target of on-board hydrogen storage system can be found elsewhere [49].

Currently there are three main methods to store hydrogen: (1) compress hydrogen at high pressure, (2) liquefy hydrogen at low temperature, (3) store hydrogen as atoms or molecule in solid state materials[50,51].The following sections will elaborate the three kind of storage technology.

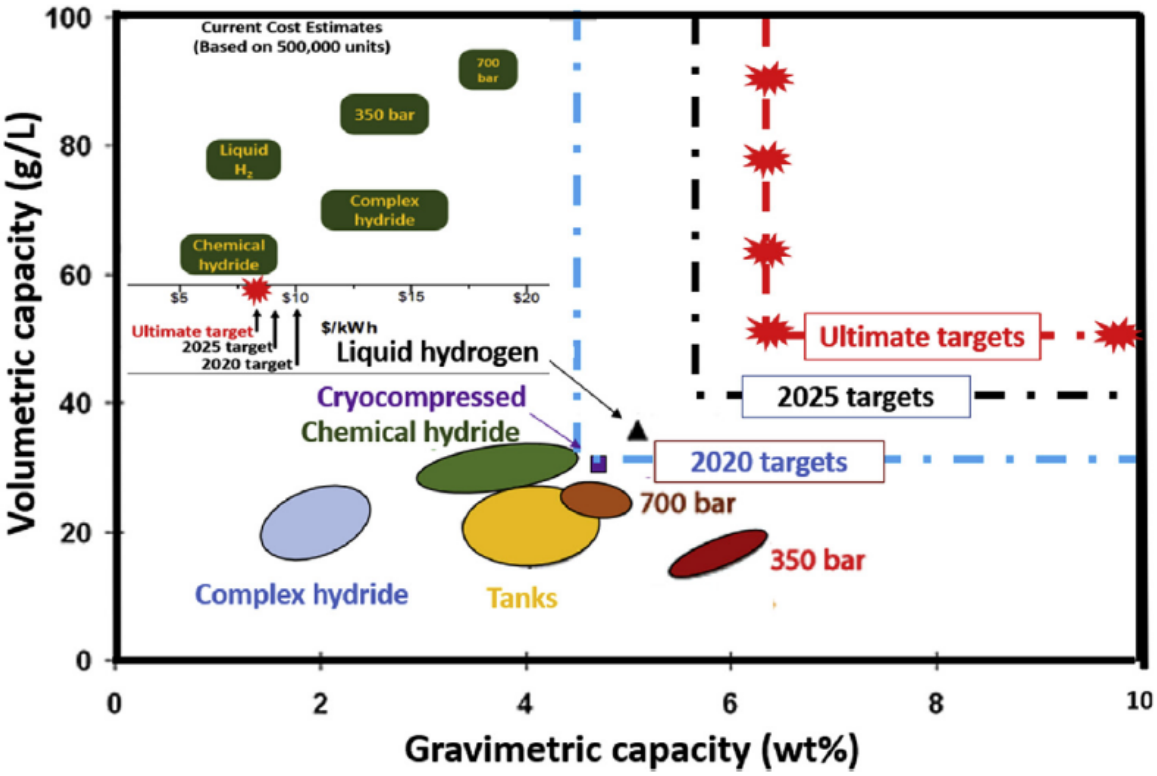

Figure 2.3. Performance target for on-board hydrogen storage systems [47].

2.2.1 Compressed with High Pressure

Since hydrogen has a very low density of 0.089 g/L, a spherical container with the diameter of 5 m is needed to store 6 kg hydrogen at atmospheric pressure [2]. Therefore, hydrogen is usually compressed at high pressure for storage in the smaller space. Figure 2.4 shows that the volume of the container decreases with the increase of pressure [52]. So far, hydrogen fuel cell cars produced by Toyota adopt this technology to store hydrogen. 700 bar tank is applied to store 4.5 wt.% hydrogen which meets the DOE target set for 2020 (Figure 2.1) [40,41]. However, some problems should not be neglected. It is not safe to handle high pressure hydrogen since a minor impact can cause hydrogen explosion. Plus, to withstand high pressure, the tank is fabricated by carbon fibre-reinforced plastic which is expensive. Another problem is the weight of the tank. According to the information given by Toyota, the tank is about 100 kg which is not suitable for family cars. Finally, hydrogen embrittlement will occur which will create cracks on the tank thus resulting in the leakage of hydrogen [2,38].

2.2.2 Liquefied with Cryogenic Temperature

Liquefying hydrogen is another mature technology for hydrogen storage (Figure 2.4). Compared with high pressure compression, liquefying is relative cheap and does not need very high pressure. The gravimetric capacity is about 6.5 wt.%. However, extremely low temperature is needed to keep hydrogen in liquid form since its boiling point is only 20 K [53]. Any form of energy input will result in hydrogen boil-off. [54,55].

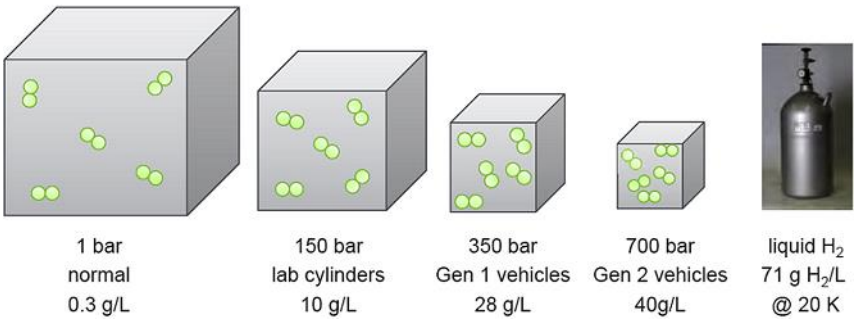

Figure 2.4. Compressed hydrogen and liquefied hydrogen [2].

2.2.3 Storing Hydrogen in Solid State Materials

To solve the problem of storing hydrogen and achieve the goal of hydrogen economy, solid state materials can be a good solution [56]. This technology allows hydrogen to be stored at a large volume with low temperature and pressure. Figure 2.3 shows the hydrogen storing ability of some solid-state materials. It can be found that the gravimetric capacity of chemical hydrides is 4.5 wt.% which approaches DOE target 2020 but does not reach the ultimate target. The storage capacity of complex hydride $LiBH_4$ has reached 18 wt.%, which is above the ultimate target [2].

Figure 2.5 displays the mechanisms of storage materials. The hydrogen binds with the storage materials either in the form of molecule on the surface of materials or in the form of atoms within the materials. Depending on the binding energy, the adsorption mechanisms can be classified as physisorption or chemisorption [34].

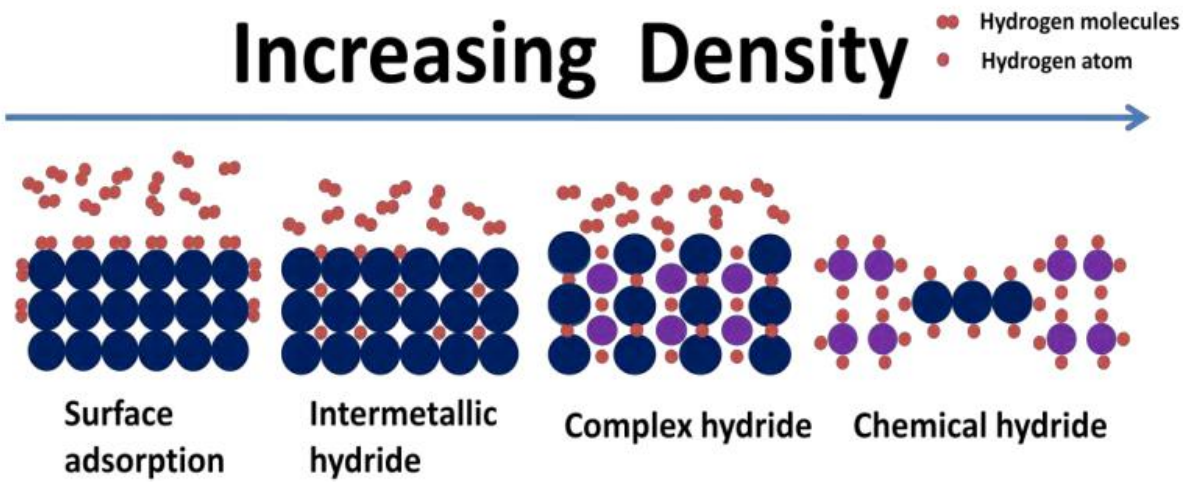

Figure 2.5. Hydrogen storage mechanisms [34].

For physisorption-based materials like porous materials or MOF materials, hydrogen will bind with materials in the form of molecule. The binding energy is very weak which is between 4-10 kJ/mol [2]. So, the bond between hydrogen and storage materials is usually Van der Waal force. The factors that influence the hydrogen storing capacity are surface area, the number of pores and the diameter of the pores [57,58]. Figure 2.6 shows the relationship between the hydrogen adsorption capacity at 77 K and BET surface areas of MOFs. With larger BET surface area and high porosity, the materials will have larger hydrogen storage capacity [59]. In addition, the adsorption of hydrogen by the means of physisorption is always engaged at cryogenic temperature. Most of the physisorption-based materials only exhibit high hydrogen storage capacity at low temperature and high pressure. At room temperature, the capacity decreases significantly [60]. Therefore, enabling physisorption-based materials to store considerable amount of hydrogen at room temperature and low pressure is the research focus.

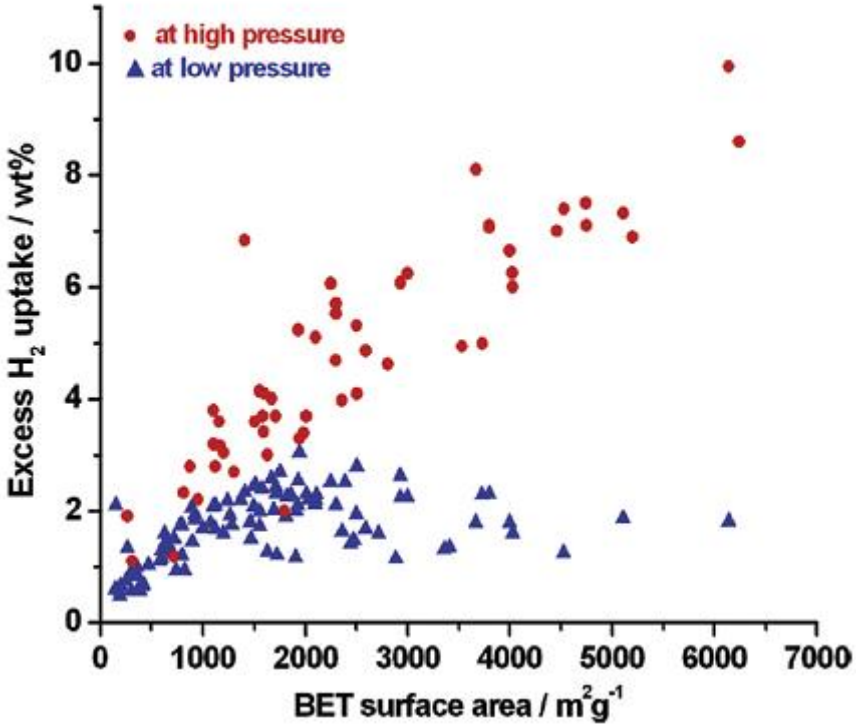

Figure 2.6 the relationship between hydrogen absorption capacity and BET surfaces of MOFs at 77 K. Low pressure is 1 bar and high pressure is between 10-90 bar [2].

Compare with physisorption, chemisorbed hydrogen binds strongly with the storage materials with binding energy of > 50 kJ/mol [2]. For chemisorption, chemical reaction occurs between hydrogen and storage materials, forming hydrogen rich compounds like complex hydrides and metal hydrides. Usually, chemisorption of hydrogen involves several steps: the molecules of hydrogen decompose at the surface of the materials, then the hydrogen atoms bind to the storing materials on the surface or diffuse into the storage materials and occupy the free space of the lattice [3]. There is a problem with chemisorption-based materials. Hydrogen binds with adsorption materials through exothermic reaction accompanying with the release of heat. Furthermore, the process of releasing hydrogen is endothermic reaction that needs extra heat input to break the bonds. So, to release hydrogen from materials for application, high temperature and low pressure are required. For examples, some light metal hydride like MgH_2 possesses high hydrogen capacity of 7.6 wt.%. However, releasing hydrogen from MgH_2

requires temperature of 573 K [2]. The high temperature requirement makes MgH_2 unattractive for moderate temperature application. Recently modification strategies including nanosizing, catalyst additions and chemical modification have been introduced to tune the reaction thermodynamic and kinetics [61-64]. .

Based on the spillover effect of metal particles, it is possible to further improve the hydrogen storage capacity of porous materials at room temperature by using some metal catalysts like Pd, Pt, Ni to decompose hydrogen molecules. During absorption process, the metal particles on the surface of materials will dissociate hydrogen molecules. After that, hydrogen atoms will move into porous materials with a very low activation energy (< 10 kJ/mol) and be adsorbed [65,66]. Figure 2.7 shows the whole process of spillover on porous materials [66].

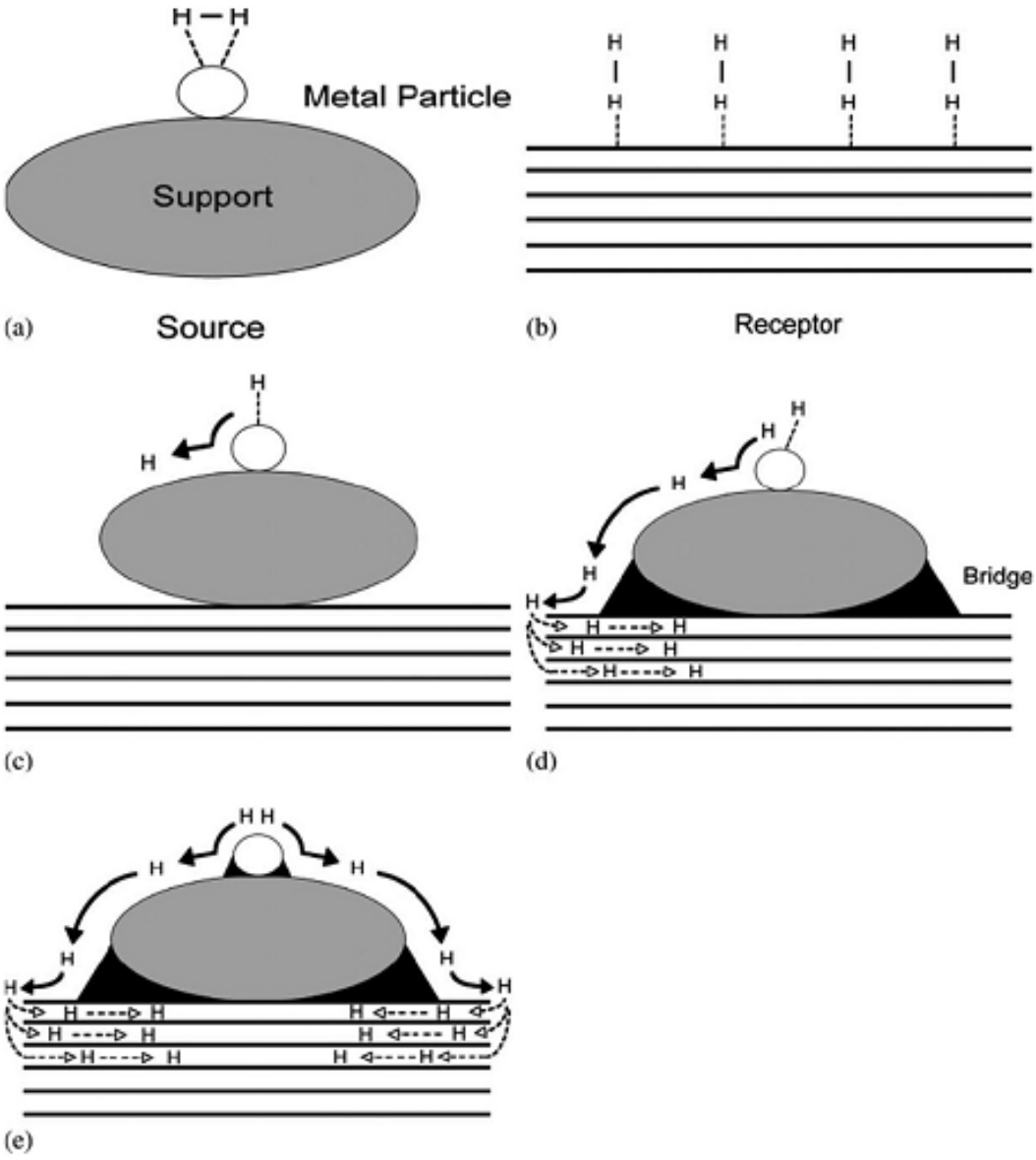

Figure 2.7 Spillover of hydrogen with catalyst on porous materials [62].

2.3 Hydrogen Storage Materials Made by Graphitic Carbon Nitride(g-C_3N_4) Nanotubes

After first found in 1834, carbon nitride has been widely used in electronic field, coating and catalyst since its amazing physical and chemical properties [67]. In these years, the research

about carbon nitride used for photocatalyst has been reported widely due to the appropriate band gap(2.7 eV) [68]. Depending on the C to N ratio and the arrangement of C and N atoms, carbon nitride can exist in lots of forms [69]. Among these forms, the heptazine based and graphite like carbon nitride with C_3N_4 stoichiometry (g-C_3N_4) is thought to be stable and promising for application (Figure 2.8) [27]. The specific surface area of g-C_3N_4 is very small (10 m^2/g) and researches on improving the specific surface area has been reported by using two-step condensation method and morphology controlling method [20]. For all the methods, morphology controlling by fabricating g-C_3N_4 in the form of nanotubes or nanowire is thought to be effective to enhance the specific surface area [20]. So far, the researchers used single precursors including C_2H_2 and N_2 gas, cyanuric chloride, melamine, and cyanuric acid to synthesis g-C_3N_4 nanotubes [70]. Moreover, the synthesis methods of g-C_3N_4 nanotubes have been explored as well, including template and template free method [70]. In this section, the fabrication methods of g-C_3N_4 nanotubes according to the commonly used precursors are introduced and discussed in detail. The application of g-C_3N_4 nanotubes in hydrogen storage is also discussed.

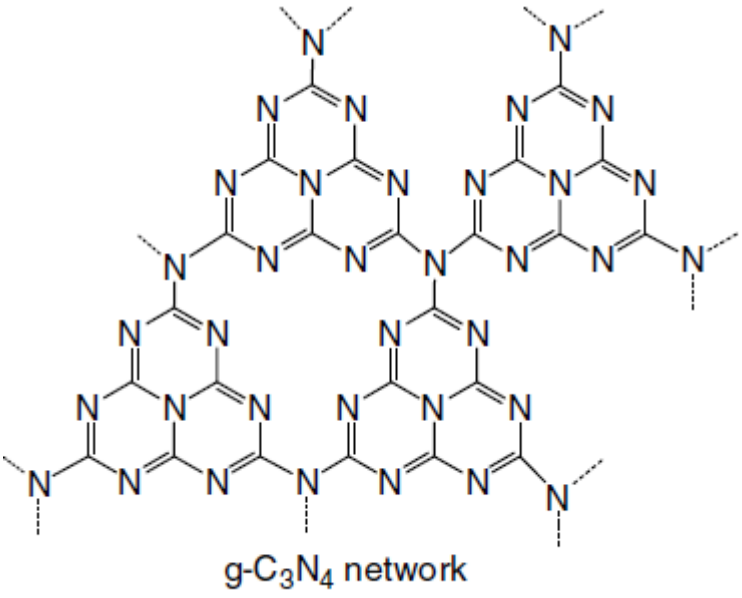

Figure 2.8 The structure of g-C_3N_4 [27].

2.3.1 Synthesis of Graphitic Carbon Nitride(g-C_3N_4) Nanotubes

g-C_3N_4 nanotubes can be synthesized by using gases as the precursors. Sung et al reported a method to synthesis g-C_3N_4 nanotubes using C_2H_2 and N_2 as precursors [71]. In this study, a porous alumina membrane (50-80 μm thick) was used as the hard template. Figure 2.9 (a) shows the formation process of carbon nitride nanotubes. In the electron cyclotron resonance chemical vapor deposition system, a huge amount of C_2H_2 and H_2 were dissociated thus a high plasma density was generated at low temperature. In the presence of a negative dc bias and a graphitic holder acting as the cathode, the flow of massive ion fluxes (CN, NH, CH, H, N_2, N_2^+, N and N^+) were guided to through the straight channel of the alumina template and to be adsorbed physically on the channel walls. The -OH groups on the curved surface of the channel walls were highly reactive which enabled the physisorbed radicals to transform to chemisorbed carbon. This unique environment made the nucleation and growth of g-C_3N_4 nanotubes with a diameter of 250 nm on the porous alumina substrate (Figure 2.9 (c) and (d)). It should be noted that when the nanotubes grew thicker and deeper, a continuous dark layer was form which covered the channel pore entries and stopped the flux passing through the channels (Figure 2.9 (a) and (b)). Thus, the size (length, wall thickness) of g-C_3N_4 nanotubes could be controlled by the flow conditions of the ion fluxes. Dc bias played an important role in the formation of carbon nitride nanotubes. Without the dc bias, the ion fluxes would only deposit on the top surface of the template resulting in the failure of the growth of the nanotube structure (Figure 2.9 (b)). If the positive dc bias was applied, an intense electric shock would happen which shorted the dc power supply. Nanotubes with high crystallinity and a uniform size could always be obtained through this method. However, there is a serious problem with this fabrication method. It is necessary to use chemical etchant to dissolve the alumina template

after fabrication. Not only this dissolving process cannot remove the template completely, but the structure and morphology of the nanotubes can also be destroyed by the chemical etchant. Therefore, a mild and effective template removing technique is required for this fabrication method.

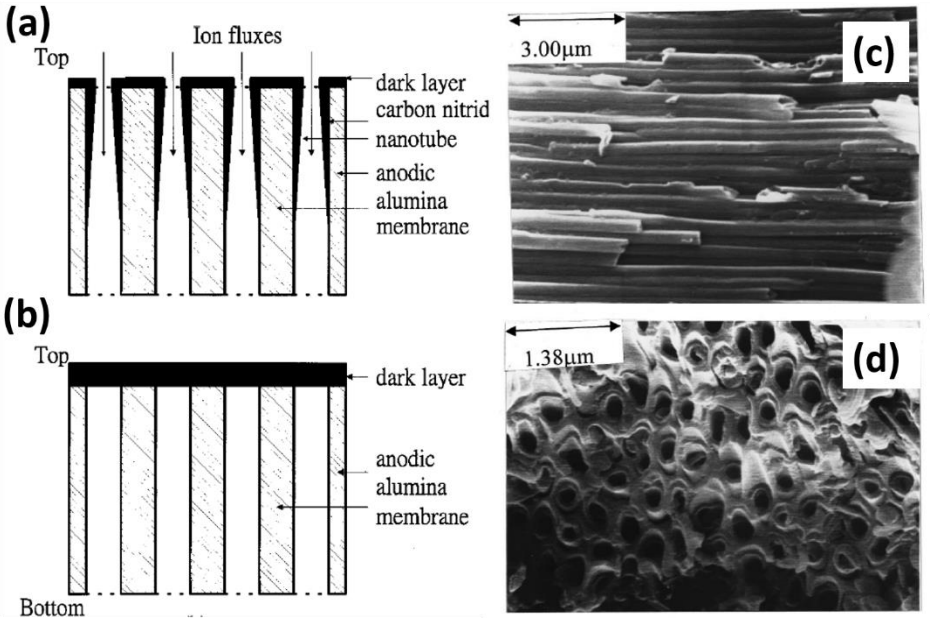

Figure 2.9. Schematic of the formation of g-C_3N_4 nanotubes on the porous alumina membrane (a) with and (b) without the dc bias. (c)(d) the morphology of synthesized g-C_3N_4 nanotubes [71].

Cyanuric chloride can also be used to fabricate g-C_3N_4 nanotubes. Guo et al. first reported a direct synthesis method to fabricate carbon nitride nanotubes by using cyanuric chloride as the precursor [72]. In this study, cyanuric chloride, NaN_3 and benzene were put into a Teflon-lined autoclave with flowing nitrogen as protecting gas. Then the chemicals in the autoclave was subjected to the solvothermal reaction which was conducted at 220 ˚C for 15 h. The product was washed by distilled water and dried in vacuum. The obtained nanotubes after drying had the length ranged from hundreds of nanometres to about two micrometres, with a diameter of

about 50-100 nm and a wall thickness of 20-50 nm. It should be noted that fabricated nanotubes did not have open ends (Figure 2.10 (a)). The synthesised materials possessed C_3N_4 stoichiometry. Cao et al. also reported a method of using cyanuric chloride to synthesis nanotubes [22]. Cao used cyclohexane instead of benzene as the solvent. According to their report, $NiCl_2$, cyclohexane and Na were put into a stainless-steel autoclave and heated at 230 ˚C for 6 h. After cooling down, cyanuric chloride was added. The autoclave was sealed again and heated at 230 ˚C for 10 h. The products were washed and dried in vacuum. The obtained carbon nitride nanotubes had the length ranged from several micrometres to a few tens of micrometres, with the diameter of 50-100 nm (Figure 2.10 (b) and (c)). The C/N ratio of the products was 1.00 which was higher than the theorical C/N ratio of g-C_3N_4 (0.75). Therefore, the synthesised nanotubes through Cao's method might not have C_3N_4 stoichiometry but had CN stoichiometry, suggesting the nanotubes formed were not g-C_3N_4 nanotubes. Different from carbon nitride nanotubes synthesised through Guo's method, the nanotubes obtained through Cao's method had open ends.

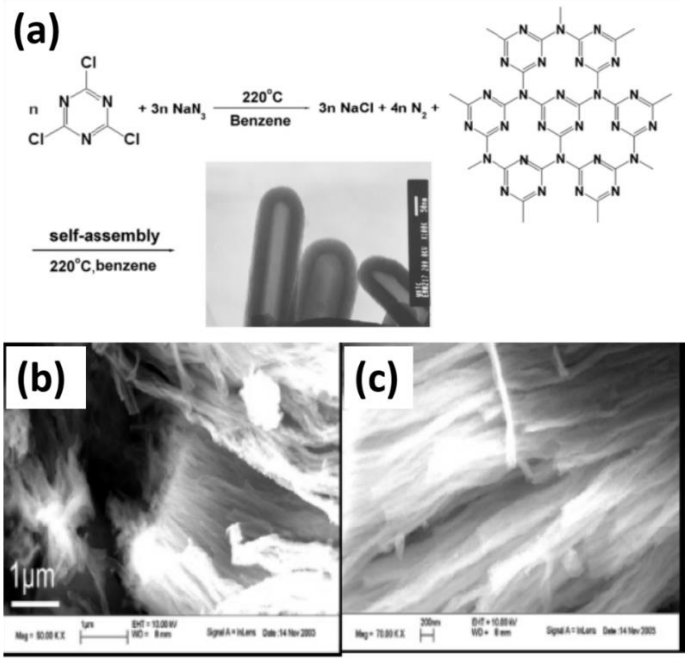

Figure 2.10. (a) illustration of the g-C_3N_4 nanotubes synthesis process via Guo's method [72]. (b) the morphology of carbon nitride nanotubes obtained through Cao's method [22].

Using melamine to synthesis g-C_3N_4 nanotubes is safer than that of cyanuric chloride. In addition, the synthesized carbon nitride nanotubes had the graphitic structure and C_3N_4 stoichiometry which are stable and promising [27]. Li et al. reported a solvothermal treatment method to fabricate carbon nitride nanotubes (g-C_3N_4 nanotubes) by using melamine as the precursor materials [21]. In this study, bulk carbon nitride (g-C_3N_4) was synthesized by calcined melamine at 550 ˚C in the first step. After that, the bulk g-C_3N_4 was dispersed in ethanol by a strong ultrasonic crasher and subjected to solvothermal treatment. The dispersion process would peel of the bulk g-C_3N_4 and thus graphitic carbon nitride(g-C_3N_4) nanosheets were obtained. In solvothermal treatment, the -OH groups of ethanol would replace the -NH_2 groups on the surface of g-C_3N_4 nanosheets. The condensation of -OH groups on nanosheets' surface resulted in the formation of g-C_3N_4 nanotubes. The inner diameter was 60 nm while the outer diameter was 80 nm for the synthesised g-C_3N_4 nanotubes, respectively. The wall thickness was 10 nm (Figure 2.11 (a) and (b)).

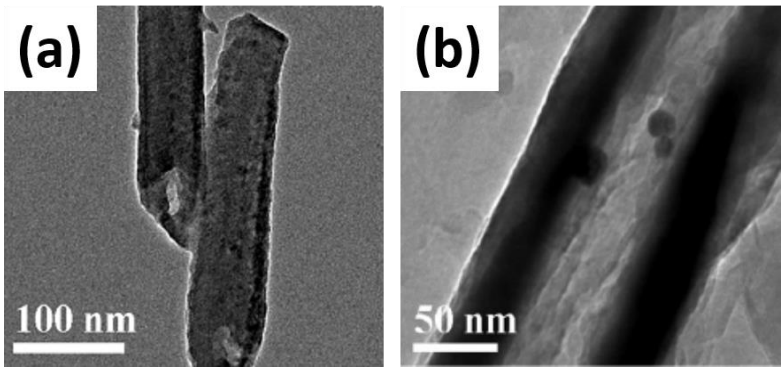

Figure 2.11. (a) (b) the morphology of graphitic carbon nitride (C_3N_4) nanotubes obtained through Li's method [21].

There is another way to synthesize g-C_3N_4 nanotubes by using melamine. Jin et al. reported a two-step condensation treatment to synthesize g-C_3N_4 nanotubes [20]. The first step of this method was hydrothermal reaction while the second step was calcination. To be more specific, in the first step melamine was dissolved in deionized water and heated at 200 ˚C in a Teflon-lined autoclave (hydrothermal reaction), then the product was heated in an alumina crucible at 550 ˚C (calcination). The authors synthesized bulk g-C_3N_4 obtained by calcining melamine for comparison. The hydrothermal reaction played a vital role in the formation of nanotube structure. Figure 2.12 shows the SEM and TEM images of bulk g-C_3N_4 and g-C_3N_4 nanotubes. Bulk g-C_3N_4 only possessed bulk and sheet-like structure, while the products after two-step condensation had tubular structure. The author also studied the influence of heating time of the hydrothermal reaction on the morphology of g-C_3N_4 nanotubes. They found that the longer heating time (24 h) resulted in a smaller diameter and wall thickness of nanotubes than that obtained from shorter heating time (12 h).

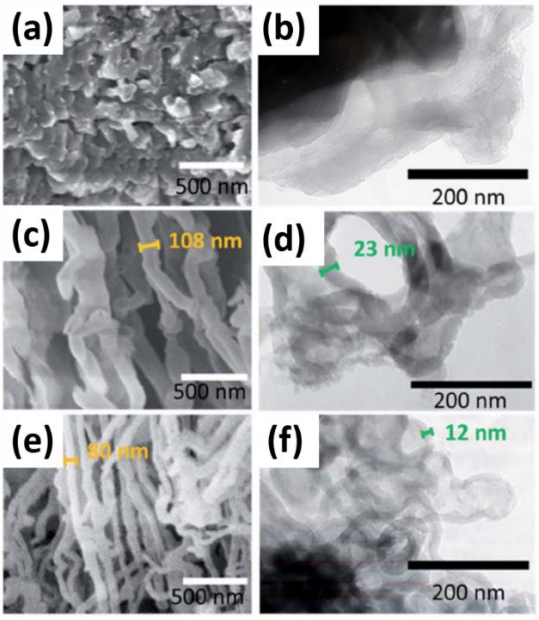

Figure 2.12. The SEM and TEM images of (a) (b): bulk g-C_3N_4. (c)(d): g-C_3N_4 nanotubes obtained at 12 h hydrothermal reaction. (e)(f): g-C_3N_4 nanotubes obtained at 24 h hydrothermal reaction [20].

Zhou et al. also reported a two-step condensation method which could synthesize tube-like g-C_3N_4 with the large scale [73]. Different from the method reported by Jin [20], in Zhou's work, melamine was dissolved in distilled water at 90 ˚C and not at room temperature before hydrothermal reaction. As a result, the clear solution could be obtained due to improved solubility of melamine at higher temperature, which should be the key to improve the yield of g-C_3N_4 nanotubes. Zhou also studied the formation mechanism of the tube-like g-C_3N_4 (Figure 2.13 (a)). They found melamine partly transformed to cyanuric acid in water during hydrothermal reaction. Then melamine formed melamine-cyanuric acid (MCA) precursor complex which had plate structure. Water molecule further helped the MCA plates transformed into rods. These rods with the length of 20-50 μm and the diameter of 1-2 μm would finally transform to g-C_3N_4 with tubular structure in the second step (calcination) by the sublimation of inner parts of the rods. This formation mechanism was also reported by Zhao et al. [19]. In Zhao's study, the transformation from melamine to cyanuric acid was accompanied with the release of NH_3. The rod-like intermediate, which were referred to MCA complex in Zhou's study [73], were formed by the self-assembly of melamine and cyanuric molecules via hydrogen bond. Each melamine molecule could form three hydrogen bonds with cyanuric acid and similarly cyanuric acid could form three hydrogen bonds with melamine molecules. The released NH_3 should play a role in the formation of the intermediates.

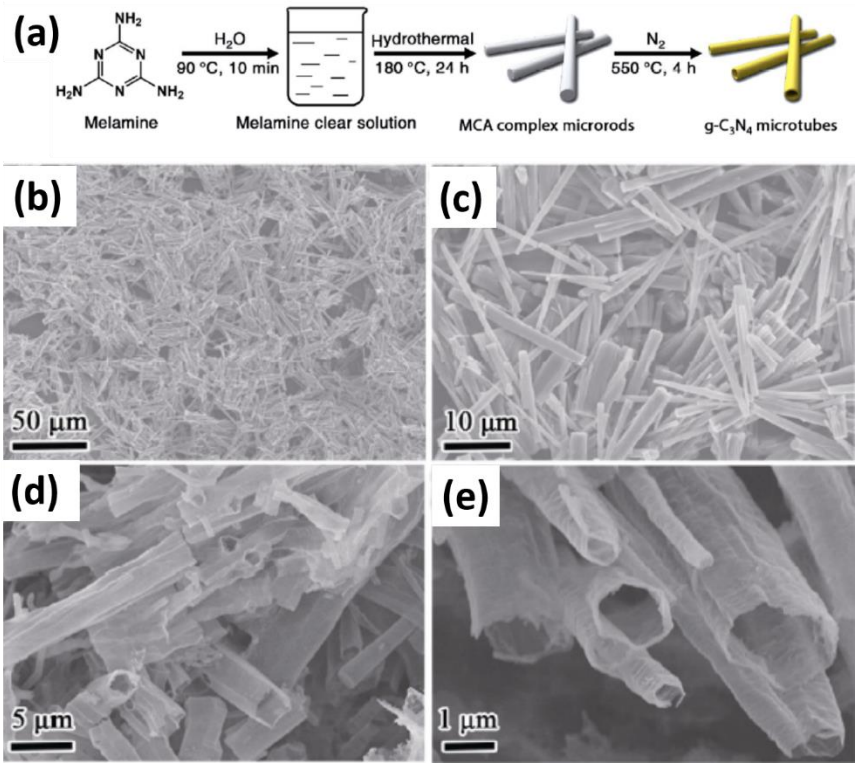

Figure 2.13. (a) Schematic illustration of the formation process of g-C_3N_4 nanotubes (b)-(e): the morphology of g-C_3N_4 nanotubes obtained [73].

Other than using melamine as the single precursor, mixed melamine with cyanuric acid has been used as the started materials. Tong et al. reported a two-step condensation method to synthesize tubular g-C_3N_4 by using the mixture of melamine and cyanuric acid [18]. In this study, melamine and cyanuric acid with the molar ratio of 1:1 was hydrothermally treated. During hydrothermal reaction, melamine formed complex with cyanuric acid through hydrogen bond and π- π bond. The complex was called CA.M complex in the article. Then the CA.M complex was calcined and transformed to g-C_3N_4 nanotubes. This g-C_3N_4 microtubes formation mechanism was similar to that synthesized by using only melamine [19,20,73]. Open-ended microtubes with the length of tens of micrometres and the width of 2 μm were obtained. It should be noted that lots of macropores could be observed on the tube body (Figure 2.14). Jordan et al. also reported a two-step condensation method using melamine and cyanuric acid

as starting materials to synthesize g-C_3N_4 nanotubes [74]. They found caffeine could help the tube structure formation. Caffeine could form two hydrogen bonds with cyanuric acid-melamine (CM) complex and thereby induce the CM complex to twist during the calcination process resulting in tubelike structure (Figure 2.15). Wang et al. reported a facile one-step polycondensation method to fabricate g-C_3N_4 nanotubes by using melamine and cyanuric acid [26]. They calcined melamine and cyanuric acid with a specific ratio. Figure 2.16 (a) shows the schematic of the formation of g-C_3N_4 nanotubes. During heat treatment, melamine and cyanuric acid started to form nanorod structure at about 400 ˚C. As the temperature increased to 550 ˚C, the nanorod gradually transformed to nanotube structure. As a result, g-C_3N_4 nanotubes with open ends were obtained. The nanotube diameter, wall thickness and length were approximately 150 nm, 15 nm and 200-800 nm, respectively. It should be noted that lots of mesopores with the size of 5-20 nm could be found on the nanotube body (Figure 2.16 (b)). Compared with two-step method which is complex and time-consuming, this facile method is more promising as it can produce g-C_3N_4 nanotubes at a higher yield and in a shorter time.

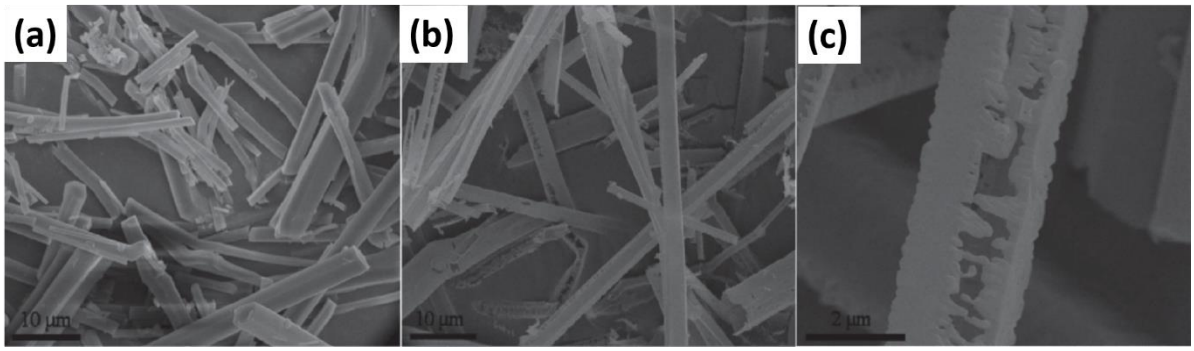

Figure 2.14. The SEM images of g-C_3N_4 microtubes. Macropores could be observed on the tube body [18].

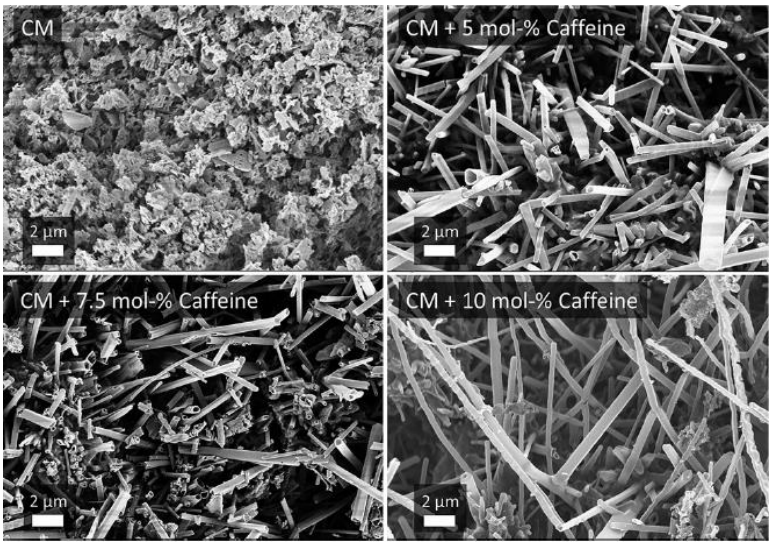

Figure 2.15. The SEM images of g-C_3N_4 microtubes synthesized with and without caffeine [74].

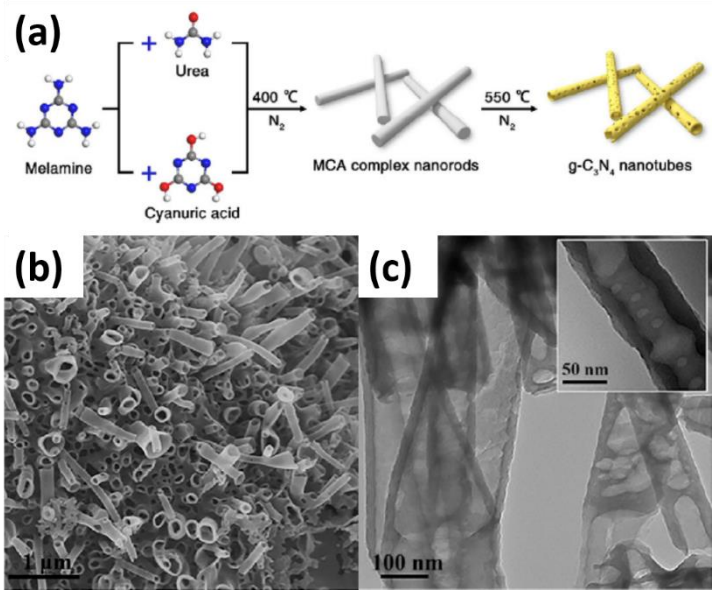

Figure 2.16. (a) schematic of the formation of g-C_3N_4 nanotubes. (b)(c): The SEM and TEM images of g-C_3N_4 nanotubes [26].

2.3.2 Hydrogen storage application of Graphitic Carbon Nitride(g-C_3N_4) Nanotubes

Graphitic carbon nitride(g-C_3N_4) nanotubes can be a good candidate for hydrogen storage. Koh et al. studied the hydrogen storage performance of g-C_3N_4 nanotubes [17]. The monolayer form of g-C_3N_4 was studied for comparison (Figure 2.17 (a)). The research was conducted by first principal calculation which was based on density function theory. According to this study, g-C_3N_4 nanotubes possessed two advantages for hydrogen storage. The first advantage was the nitrogen-induced nanopores (0.7 nm) on the nanotube body which allowed hydrogen to be stored within the nanotubes. The second reason was the doubly bonded nitrogen atoms at the edge of the nanopores provided active sites for hydrogen chemisorption and physisorption. Each nitrogen atoms could chemisorb one hydrogen atom. Hydrogen molecules could be easily adsorbed either at the centre of the nanopores or within the nanotubes. The energy barrier for hydrogen molecules accessing to the interior of the nanotubes was only 0.54 eV, implying a fast hydrogen uptake rate at relative low temperature and pressure. The calculated binding energy for one H atom was lower for g-C_3N_4 nanotubes (-0.24 eV--0.31 eV) than for g-C_3N_4 monolayer (-0.14 eV), suggesting adsorbed hydrogen was stable in g-C_3N_4 nanotubes (Figure 2.17 (b)). The authors also found the size of nanotubes influence the binding energy. The smaller nanotubes were, the higher binding energy nanotubes possessed. The nanotubes with the diameter of 0.8 nm had the binding energy for one H atom of -0.31 eV while only -0.24 eV for the nanotubes with the diameter of 2.3 nm. The calculated hydrogen storage capacity was about 4.66 wt.% (1.57 wt.% for chemisorption, 3.09 wt.% for physisorption) when hydrogen was adsorbed on both sides of the nanotubes (Figure 2.17 (c)). The capacity could be further improved to 5.45 wt.% if the nanotubes were arranged in the form of a bulk bundle due to the increased availability of space among the nanotubes (Figure 2.17 (d)). In addition, the doubly bonded nitrogen atoms could be easily functionalized with single metal which had a good

affinity to molecule hydrogen. The author found that hydrogen molecules could be only adsorbed on the outer nanotube surface due to the high energy barrier (9.7 eV) for hydrogen to pass through the interior of the nanopores if g-C_3N_4 nanotubes were functionalized by Ti. The molecules were bonded over Ti atoms with an average binding energy of -0.23 eV. This energy was lower than the physisorption binding energy of hydrogen molecules (-0.09 eV) in g-C_3N_4 nanotubes without metal functionalization, suggesting hydrogen storage capacity could be further improved with metal doping.

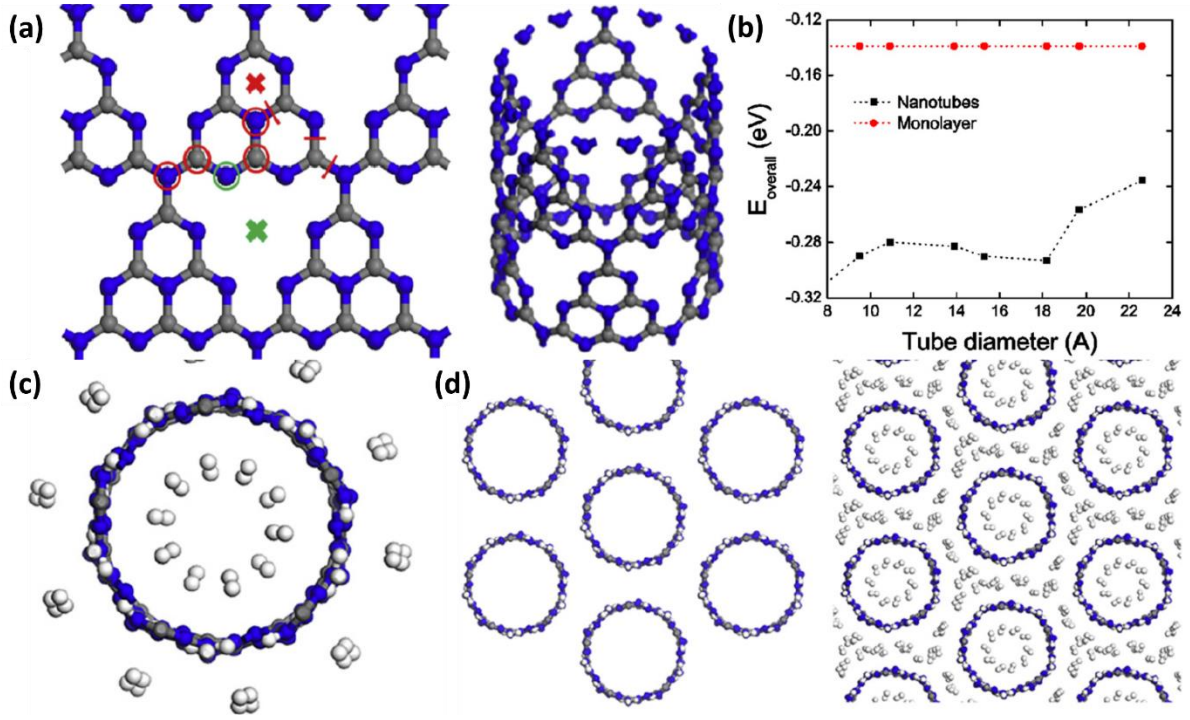

Figure 2.17. (a) g-C_3N_4 monolayer and nanotube. (b) binding energy of g-C_3N_4 nanotubes and monolayer. (c) Hydrogen was adsorbed in the single g-C_3N_4 nanotubes. (d) hydrogen was adsorbed in the g-C_3N_4 nanotube bundles [17].

Kim et al. studied the hydrogen storage performance of double-walled g-C_3N_4 nanotubes by both experiment and theoretical calculation [75]. In this study, g-C_3N_4 nanotubes with 0.6 nm

nanopores were synthesised through a microwave plasma-enhanced CVD (PE-CVD). The starting materials were CH_4, N_2, H_2 and O_2. The authors found that hydrogen could be adsorbed firmly between the walls of g-C_3N_4 nanotubes (Figure 2.18 (a)). The calculated physisorption energy of hydrogen molecules adsorbed on the outside of nanopores in the double-walled g-C_3N_4 nanotubes was -0.12 eV, which was lower than the energy of hydrogen molecules adsorbed on the outer surface of double-walled carbon nanotubes. The barrier (0.31 eV) was also low for hydrogen penetration through nanopores from the outside to the inside of g-C_3N_4 nanotubes, compared with the barrier of hydrogen passing through the hexagon ring of carbon nanotubes (16.5eV). Indeed, hydrogen was adsorbed firmly between two nanopores with the adsorption energy of -0.17 eV, which was lower than the energy (-0.1eV) of hydrogen adsorbed between the perfect walls (without pores) of double-walled carbon nanotubes (Figure 2.18 (b)). Therefore, hydrogen could either adsorb firmly on the surface of g-C_3N_4 nanotubes or easily pass through the nanopores and be stored firmly between the walls of g-C_3N_4 nanotubes. 0.36-0.50 eV was needed to discharge the hydrogen adsorbed between the walls which was consistent with the experimental Temperature Programming Desorption (TPD) results(Figure 2.18 (c)). The authors predicted 7 wt.% hydrogen could be achieved in g-C_3N_4 nanotubes.

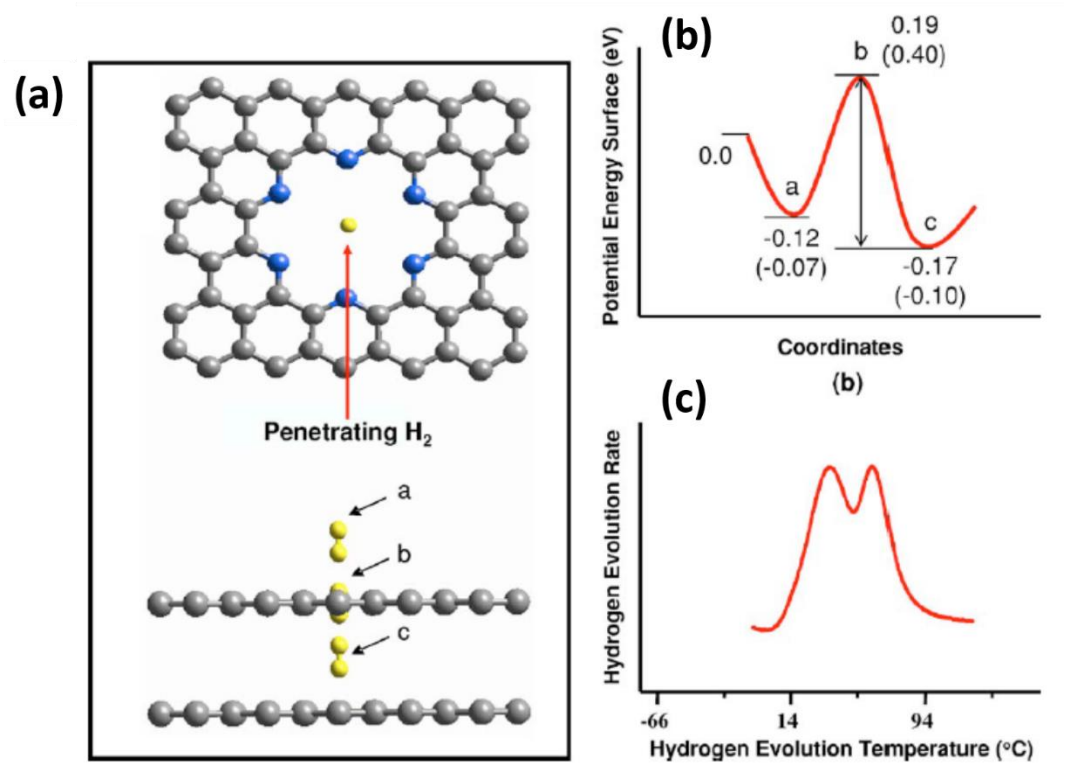

Figure 2.18. (a) Schematic of hydrogen adsorbed between the walls. (b) adsorption energy of hydrogen adsorbed on the surface and between the walls in g-C_3N_4 nanotubes. (c) Temperature Programming Desorption (TPD) spectra obtained from the nanotubes with the diameter of 40 nm [75].

To the best of our knowledge that the number of publications on hydrogen storage performance of g-C_3N_4 nanotubes studied through the experimental method is extremely scarce, let alone the study of hydrogen storage performance of other g-C_3N_4 materials (bulk g-C_3N_4, carbon nitride nanobells) [76-78] and the study of g-C_3N_4 nanotubes through theoretical calculation [17,75]. Hence, this study aims to make up for the lack of experimental research of g-C_3N_4 nanotubes for hydrogen storage in the literatures as well as the detailed discussions of the possible mechanism involved during the hydrogen adsorption and desorption process.

Chapter 3 Experimental Methodology

The fabrication methods of g-C_3N_4 materials (bulk g-C_3N_4, g-C_3N_4 nanotubes and g-C_3N_4 nanosheets) and Ni-g-C_3N_4 nanotubes are introduced. The characterizations used are also described in the following chapters.

3.1 Sample Preparation

3.1.1 Fabrication of g-C_3N_4 Nanotubes

The fabrication of g-C_3N_4 nanotubes was followed the method proposed by Wang et al. [26], with a minor adjustment as described later. Commercially melamine powders (⩾ 99 %, IMCD Australia Limited, Australia) and cyanuric acid powders (≥ 98 %, Merck Pty Limited, Germany) were used. In the synthesis of g-C_3N_4 nanotubes, 1 g melamine was ground with 5 g cyanuric acid for 10 minutes by using an agate mortar. Then the ground powders were put into an alumina crucible for the heat treatment.

In Wang's work, the heat treatment was done in the tube furnace with nitrogen as protecting gas [26]. However, in this study, the heat treatment was conducted in the muffle furnace in air. There is one reason for this: Using the tube furnace is time-consuming. The furnace in UNSW needs to be filled with nitrogen first before increasing the temperature. The filling process takes about 30 minutes. After calcination, the furnace needs about 12 hours to cool down before the products can be safely removed. It will be much easier (no filling process) to use and quicker to cool down (3 h) if the samples is calcined in air in the muffle furnace.

The following heat treatment was done at 550 °C for 4 hours with a heating rate of 5 °C /min. Yellow and light powders (g-C_3N_4 nanotubes) were obtained and was termed C-550.

Before the heat treatment, the crucible was wrapped and sealed by aluminium foil to prevent the loss of final products g-C_3N_4 nanotubes.

3.1.2 Fabrication of g-C_3N_4 Nanosheets

The synthesis of g-C_3N_4 nanosheets is similar to the synthesis of g-C_3N_4 nanotubes, except the calcination temperature is higher. Here 1 g melamine and 5 g cyanuric acid (ground for 10 minutes in the agate mortar) were loaded in the foil wrapped alumina crucible, heated from room temperature (25 $^{\circ}$C) to 620 $^{\circ}$C and kept at 620 $^{\circ}$C for 4 hours, with the heating rate of 5 $^{\circ}$C /min. The heat treatment was also conducted in the muffle furnace in air. The as-prepared samples were labelled as C-620.

3.1.3 Fabrication of bulk g-C_3N_4

The fabrication of bulk g-C_3N_4 is the same as the fabrication of C-550 except only melamine was used. The compared bulk g-C_3N_4 sample was prepared by directly heating 1 g melamine powders in the muffle furnace in air at 550 $^{\circ}$C for 4 hours, with the heating rate of 5 $^{\circ}$C /min.

3.1.4 Comparative Multiwall Carbon Nanotubes (MWCNTs)

For comparison study, multiwalled carbon nanotubes (MWCNTs) were purchased from Shenzhen Nanotech Port Co., Ltd, China, the vendor used chemical vapor deposition (CVD) for the fabrication of MWCNTs. The as-received MWCNTs had a purity > 95 % and a length of 5-15 μm. The diameter was 60-100 nm.

3.1.5 Fabrication of Ni-g-C_3N_4Nanotubes

In the fabrication, 0.01-0.12 g nickel powders with an average size of 10 μm (Merck KGaA, Germany) were mixed with 1 g melamine and 5 g cyanuric acid powders by the agate mortar. Then the mixture (which is called MCN complex in following discussion) was transferred to the foil wrapped crucible and calcined at 550 ˚C for 4 hours, with a heating rate of 5 ˚C /min. The heat treatment was conducted in the muffle furnace in air. Yellow and grey powders which were the mixture of nickel nitride and g-C_3N_4 nanotubes were obtained. The obtained samples were then washed by deionised (DI) water to remove impurities nickel nitride. The washed samples were labelled as xC-550 respectively, where x stands for the mass of used nickel (0.01-0.12 g) in the fabrication. The washing procedures were:

1. Dispersing samples in DI water by ultrasonication for 10 minutes. During ultrasonication, black precipitates (nickel nitride) sank to the bottom of the beaker while g-C_3N_4 nanotubes dispersed in DI water. The upper dispersion was poured to another beaker while the black precipitates at the bottom were disposed.

2. Recollecting g-C_3N_4 nanotubes from the dispersion through filtration.

3. Drying the collected g-C_3N_4 nanotubes in the oven at 70 ˚C for 6 h.

3.2. Characterization

The powder X-ray diffractometer (XRD) patterns were collected on a Philips X'pert Multipurpose XRD system operated at 40 mA and 45 kV, with Cu Kα radiation (λ=1.5406 Å). The spectra were acquired from 10 ° to 70° or 10° to 80°.

Field emission scanning electron microscopy was conducted on a FEI Nova NanoSEM 450 or 230 microscope. Spectra was obtained with a beam voltage of 5-15 kV and a working distance of 5 mm. For SEM examinations, the samples were dispersed in ethanol by ultrasonication for about 30 minutes, and then dropped onto a silicon wafer. After fully dried, the samples on the wafer were coated with 10 nm-20 nm platinum by a Leica ACE 600 coater which could control the depth of coat to increase the electrical conductivity. Transmission electron microscopy (TEM) was performed on a JEOL JEM-F200 with an operation voltage of 200 kV or 80 kV, so as to get more structure and morphology details. The samples for TEM study were prepared by dispersing in ethanol followed by 30-minute ultrasonication, and then dropped on a carbon doped copper grid.

Fourier transform Infrared (FTIR) spectra of the fabricated g-C_3N_4 samples (bulk, nanotubes and nanosheets) were obtained on a Perkin Elmer Spectrum Two spectrometer at room temperature in the range of 4000-450 cm^{-1} with a resolution of 4 cm^{-1}. The spectra of these g-C_3N_4 materials were collected on ATR mode and the spectrum of MWCNTs was collected on transmittance mode. For transmittance mode, MWCNTs was mixed with KBr and transferred to the spectrometer as soon as possible to minimize moisture.

X-ray photoelectron spectroscopy (XPS) of the fabricated g-C_3N_4 samples was conducted on a Thermo ESCALAB250i high-resolution X-ray Photoelectron Spectrometer (base pressure below 2.10^{-6} Pa) using a monochromatic Al Kα X-ray source (1486.68 eV) with a power of 120 W. Survey scans were collected at 100 eV pass energy and region scans were collected at

20 eV pass energy. Core level binding energies were calibrated using C1s peak at 284.8 eV as the charge reference.

Nickel content in Ni-g-C_3N_4 nanotubesbefore and after washing was measured by Inductively Coupled Plasma Optical Emission Spectroscopy (ICP-OES). Samples were digested with mixed acid ($HCl+HNO_3$) followed by microwave digestion. The clear solution was analysed by ICP-OES (Optima7300DV, PerkinElmer, USA).

N_2 adsorption and desorption isotherms of the fabricated g-C_3N_4 samples were obtained on a Micromeritics TriStar 3000 Analyzer at 77 K, the surface area and internal pore characteristics were calculated by Brunauer-Emmett-Teller (BET) manner and Barrett-Joyner-Halenda (BJH) adsorption method, respectively. Prior to the test, the samples were degassed at 150 $^{\circ}$C for 3 hours under vacuum in order to remove the moisture and dissolved gases.

3.3 Hydrogen Storage characterisation

The hydrogen adsorption/desorption and relative kinetic studies were conducted on a high-pressure Sievert instrument system, which is shown in Figure 3.1, in the range 0-3.7 MPa and room temperature to 65 $^{\circ}$C. Figure 3.2 shows the simple illustration of this system. There are four valves: V3 controls the vacuum system while V4 controls the sample system and V2 controls the hydrogen supply system. V1 controls the inert gas supply system which was not used in this study. The measuring system consists of P (pressure gauge) and B (hydraulic accumulator). T1 and T2 are the thermometers measuring the temperature of measuring system and sample system. The sample system consists of three parts: F (filter), C (thermostat bath) and D (sample container). The main parts of the system are measuring system and sample system loading the samples. Prior to the test, the system was precisely calibrated by introducing 0.1-0.5 MPa 99.999 % high purity hydrogen gas at different temperatures based on the Japanese Industrial Standard H 7201 (JISH 7201) [79]. The samples were degassed at 280 $^{\circ}$C under

vacuum (10^{-3} Torr) for 4 hours to remove moisture and dissolved gases. After degassing, the activated samples were then cooled down to a specific temperature under vacuum and ready for hydrogen storage test. For adsorption study, high purity hydrogen gas was introduced to the measuring system and the pressure was increased step by step. The samples were allowed to contact with hydrogen at each step by opening the valve (V4). The pressure was decreased and reached the equilibrium at each pressure since hydrogen adsorption after contacting. The hydrogen storage capacities, as expressed in weight percentage, was plotted in the form of pressure-composition-isotherm (PCI). After equilibrium, the valve (V4) was closed and more hydrogen was introduced to the measuring system to increase the pressure for next step's test. The desorption study was conducted right after the adsorption study which was the reverse of adsorption process where the hydrogen pressure was allowed to decrease stepwise during the test. The sample were allowed to contact hydrogen at each step as well. The pressure was increased and reached the equilibrium at each pressure since hydrogen desorption after contacting.

The calculation of the change of the storage capacity (wt.%) from each step's pressure change is based on the ideal gas formula:

$$PV = nRT$$

where P indicates the system pressure (Pa),

V is the gas volume under P (m^3),

n is the mole of ideal gas (mol),

T is the system temperature (K),

R is the ideal gas constant (8.314472 J/mol/K).

Basically, the overall hydrogen should be the same before/after the samples contact hydrogen:

$$n_1 + n_s = n_2 + n_s'$$

where n_1 is the amount of hydrogen in the system before contacting,

n_s is the amount of hydrogen in the sample before contacting,

n_2 is amount of hydrogen in the system after contacting,

n_s' is the amount of hydrogen in the sample after contacting.

The changed amount of hydrogen in the samples (since adsorption or desorption) can be calculated through equation (1):

$$\Delta n = n_1 - n_2 = n_s - n_s' \quad (1)$$

The system consists of two parts, measuring system and sample system for loading the samples. Therefore, the hydrogen in the whole system can be the hydrogen in the measuring system plus the hydrogen in the sample system, equation (1) can be written as:

$$\Delta n = n_1 - n_2 = n_{m1} + n_{s1} - n_{m2} - n_{s2} \quad (2)$$

Where n_{m1} is the amount of hydrogen in the measuring system before contacting,

n_{m2} is the amount of hydrogen in the measuring system after contacting,

n_{s1} is the amount of hydrogen in the sample system before contacting,

n_{s2} is the amount of hydrogen in the sample system after contacting.

By apply the ideal gas formula, n_1 can be written as:

$$n_1 = n_{m1} + n_{s1} = \frac{(\frac{P_1 V_m}{T_m} + \frac{P_1' V_s}{T_s})}{R} \quad (3)$$

Where R is the ideal gas constant,

P_1 is the pressure in the measuring system before contacting,

V_m is the volume of the measuring system,

T_m is the temperature in the measuring system,

P_1' is the pressure in the sample system before contacting,

V_s is the volume of the sample system,

T_s is the temperature of the sample system.

For the measurement at a certain step, the pressure P_1 in the measuring system before contacting can be read directly from the pressure gauge. The pressure P_1' in the sample system before contacting should be equal to the previous step's pressure in the measuring system after contacting as the pressure reaches equilibrium at the previous step and the pressure in both systems are the same.

By applying the ideal gas formula, n_2 can also be written as:

$$n_2 = n_{m2} + n_{s2} = \frac{(\frac{P_2V_m}{T_m} + \frac{P_2V_s}{T_s})}{R} \quad (4)$$

Where P_2 is the pressure in the measuring system after contacting.

For the measurement at a certain step, the pressure P_2 in the measuring system after contacting can be obtained directly from the pressure gauge. The pressure in the sample system after contacting should be P_2 as well. Since the pressure reaches equilibrium after contacting so the pressure in both systems should be the same.

Therefore, Δn can be written by applying equation (3) and (4) to (2), which is:

$$\Delta n = \frac{(\frac{P_1V_m}{T_m} + \frac{P_1'V_s}{T_s})}{R} - \frac{(\frac{P_2V_m}{T_m} + \frac{P_2V_s}{T_s})}{R} \quad (5)$$

Equation (5) should be only used for ideal gases. In order to apply it to calculate the hydrogen content in the samples in this study. Correction is needed. Japanese Industrial Standard H 7201(JISH 7201) is referred to make the correction [79]. The correction factors of compression ratio are introduced to equation(5):

$$\Delta n = \frac{(\frac{P_1V_m}{Z_1T_m} + \frac{P_1'V_s}{Z_2T_s})}{R} - \frac{(\frac{P_2V_m}{Z_3T_m} + \frac{P_2V_s}{Z_4T_s})}{R} \quad (6)$$

Z_1-Z_4 are the correction factors. The correction factors can be calculated through the following equation as state in Japanese Industrial Standard H 7201(JISH 7201) [79]:

$$Z = 1 + P * \left(A + \frac{B}{T} + \frac{C}{T^2} + \frac{D}{T^3} + \frac{E}{T^4}\right) \quad (7)$$

Where P is the pressure,

T is the temperature in the measuring system or sample system.

A, B, C, D are constant, which are:

A: 4.93482*10^{-5},

B: 2.04036,

C: 8.15334*10,

D: -6.5561*10^{4}.

Therefore, the changed hydrogen content in the samples in weight percent at each step's pressure change can be obtained by:

$$\Delta m = \frac{M}{m}\left(\frac{\left(\frac{P_1 V_m}{Z_1 T_m}+\frac{P_1' V_S}{Z_2 T_S}\right)}{R} - \frac{\left(\frac{P_2 V_m}{Z_3 T_m}+\frac{P_2 V_S}{Z_4 T_S}\right)}{R}\right) \quad (8)$$

Where M is the mole mass of hydrogen molecule,

m is the weight of tested samples.

Figure 3.1. High-pressure Sievert instrument.

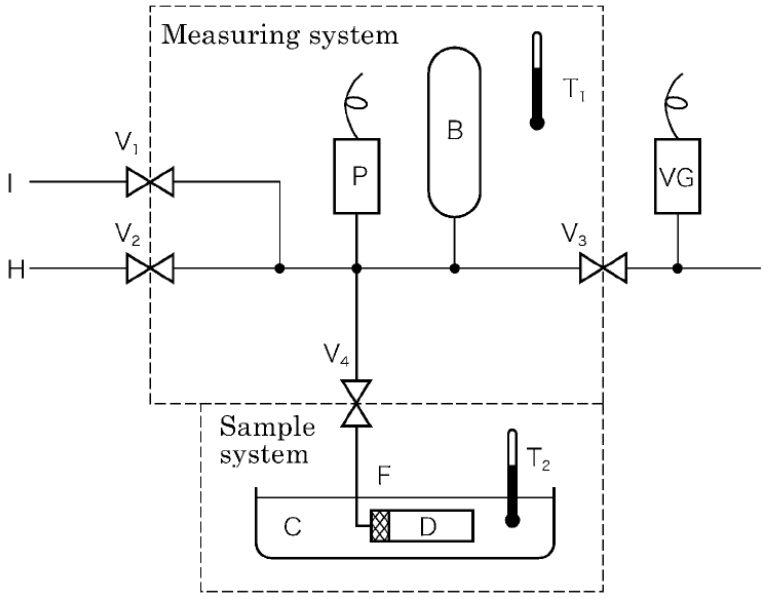

Figure 3.2. Simply illustration of hydrogen adsorption/desorption measuring system [1].

Temperature programmed desorption (TPD) was conducted on AutoChem II 2920 (Figure 3.3) to further study the sorption behaviour. Prior to the test, the samples were degassed at 150 °C in vacuum for three hours to remove adsorbed gases and moisture. Then the samples were heated from room temperature (25 °C) to 300 °C with a heating rate of 10 °C/min in the flow of argon gas (20 ml/min). The purpose of the heat treatment is to remove any chemical species remaining in the samples which would decompose above 150 °C but below 300 °C thus influence the following TPD test. The heat treatment was conducted several times until no signal could be detected, suggesting all impure chemicals has been removed. Therefore, any signal detected should be from hydrogen desorption not from other chemical decomposition in later TPD experiment. For TPD experiment, the samples were charged with 99.99 % hydrogen at 25 °C or 65 °C at 0.1 MPa for three hours. After charging, the samples were purged by argon for 30 minutes to remove physisorbed hydrogen. Then the samples were heated from 25 °C to 300 °C with a heating rate of 10 °C/min using argon as carrier gas, the flow rate was 20 ml/min.

Figure 3.3. AutoChem II 2920.

Chapter 4 Results and Discussion

4.1 Introduction

g-C_3N_4 nanotubes are one of the promising hydrogen storage materials for two reasons. The first reason is the nitrogen-induced nanopores on the nanotube. The doubly bond nitrogen at the edge of pore can be an active site for hydrogen adsorption; plus, if the nanotubes have multiwall structure, hydrogen can pass the pores and be stored between the walls firmly [17,75]. The second reason is the nitrogen atom. The nitrogen atoms can strengthen the interaction between hydrogen and adsorbent by inducing dipole interaction or reducing the energy barrier of dissociation adsorption [9-13]. The traditional syntheses of g-C_3N_4 nanotubes are suffering from time-consuming, low yield and usage of toxic chemicals [25]. In this study, a convenient and environment-friendly polycondensation method was used to synthesize the materials. Multiwall carbon nanotubes (MWCNTs) and two different g-C_3N_4 materials, bulk g-C_3N_4 and g-C_3N_4 nanosheet were studied for comparison. For convenience, g-C_3N_4 nanosheets and g-C_3N_4 nanotubes are labelled as C-620 and C-550 in following discussion.

During the fabrication process of g-C_3N_4 nanotubes, toxic NH_3 gas was released which detrimentally affected the environment and safety [33]. As reported by Fang et al, nickel could decompose NH_3 to form H_2 and N_2. The produced hydrogen generated water atmosphere with oxygen, which prevented the great aggregation of g-C_3N_4 layers and thus resulted in the formation of nanosheets. The generated water atmosphere further triggered C/N-steam reforming reaction and created defects on the g-C_3N_4 nanosheets [33]. For this reason, nickel was used in the fabrication of g-C_3N_4 nanotubes to create defects and thus increase the surface area of the g-C_3N_4 nanotubes. Four samples were synthesised and studied. The difference in the four samples was the amount of nickel used in the fabrication. The fabrication process was

described in detail in Chapter 3, in which the mixture of nickel, melamine and cyanuric acid was heated at 550 °C for 4 h. After the heat treatment, the obtained materials were washed by DI water to remove impurity nickel nitride. The washed samples were labelled as 0.01C-550, 0.03C-550, 0.08C-550 and 0.12C-550 (0.01, 0.03, 0.08 and 0.12 denote the mass (g) of nickel used in the fabrication).

In this chapter, physical, chemical properties, and microstructural characterisations of g-C_3N_4 nanotubes and Ni-g-C_3N_4 nanotubes are presented. The hydrogen storage performance as characterized by PCI method are then related to the various properties characterised.

4.2 SEM and TEM Observations on g-C_3N_4 nanotubes produced

The morphology of C-550 was studied by SEM and TEM. As shown in Figure 4.1, C-550 presented the porous and tubular structure. In Figures 4.1 (a) and (b), lots of nanotubes aggregated together, forming a kind of packed network superstructure. Almost all C-550 nanotubes were embedded in the tangled structure with a length of 0.8-1 μm and a diameter of 50-400 nm. In Figures 4.1 (c) and (d), very long nanotubes also could be spotted in C-550. The length of this long tube was about 4 μm and the diameter was about 300 nm. Interestingly, several pores can be clearly seen on the long tube body as indicated in Figure 4.1 (d) by red circles, the diameter of these pores was about 40 nm. Theses pores could be good for hydrogen storage since hydrogen molecules or atoms could diffuse into the inner parts through the pores and then be trapped. In addition, there were lots of non-tube-like but bulk-like structure in C-550. As can be seen later, these non-tube forms were not effective to trap hydrogen and hence should be eliminated. The improvement in the fabrication process or purifying method is outside the scope of this work but is recommended in the future study.

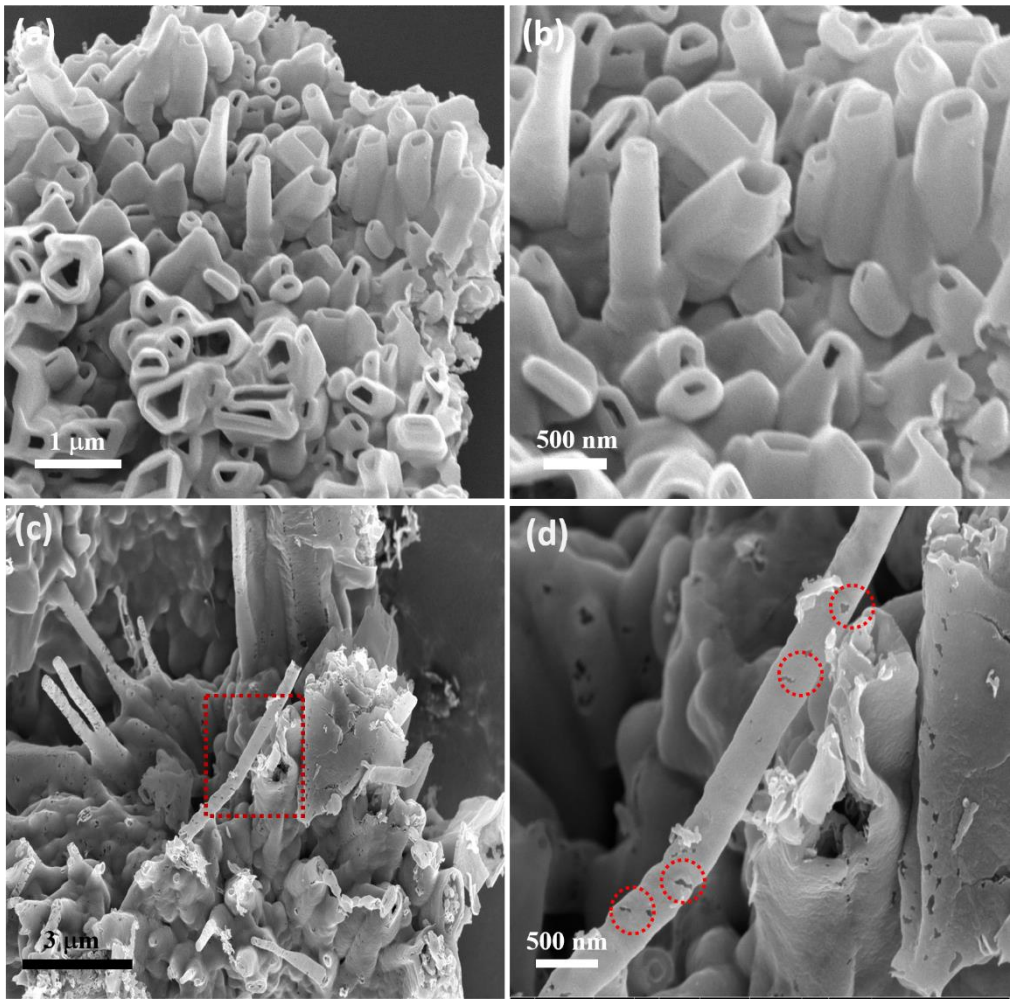

Figure 4.1. (a) (b): SEM images of C-550, nanotubes with the length of 0.8-1 μm and the diameter of 50-400 nm were observed; (c): Long nanotubes with the length of 4 μm and the diameter of 300 nm were found, bulk-like-structure (impurity) could be found as well; (d): Enlarged image of the long nanotube which possessed several pores (40 nm) on the body.

Figures 4.2 shows the SEM micrographs of the products obtained by heating melamine and cyanuric acid at different temperature which illustrates the formation process of g-C_3N_4 nanotubes (C-550) during the heat treatment. The samples were still in bulk structure at 300 ˚C. After 400 ˚C, nanorods structure started to grow on the surface of the bulk particles. With the temperature further increased to 550 ˚C, nanorods opened and changed to nanotubes. It seems that the bulk precursor acted as the substrate which supported the growth of nanotubes on it.

That explains why a packed network superstructure of g-C_3N_4 nanotubes was obtained in Figures 4.1 (a) and (b). Figures 4.3 (a) and (b) show the TEM images of C-550. The nanotube had a diameter of about 400 nm and a length of about 1.2 μm. The wall thickness was about 70 nm, suggesting multiwalled structure. Several pores on the nanotube body with an average size of 40 nm have been found, confirming the observations from SEM study. Figure 4.3 (c) presented a magnified picture of the tube wall confirming lots of g-C_3N_4 layers stacking together. This characteristic clearly indicates a multiwalled structure was obtained. The interlayer distance of these layers was also calculated according to diffraction pattern shown in Figure 4.3 (d), which is 3.24 Å corresponding to a (002) plane stacking [26].

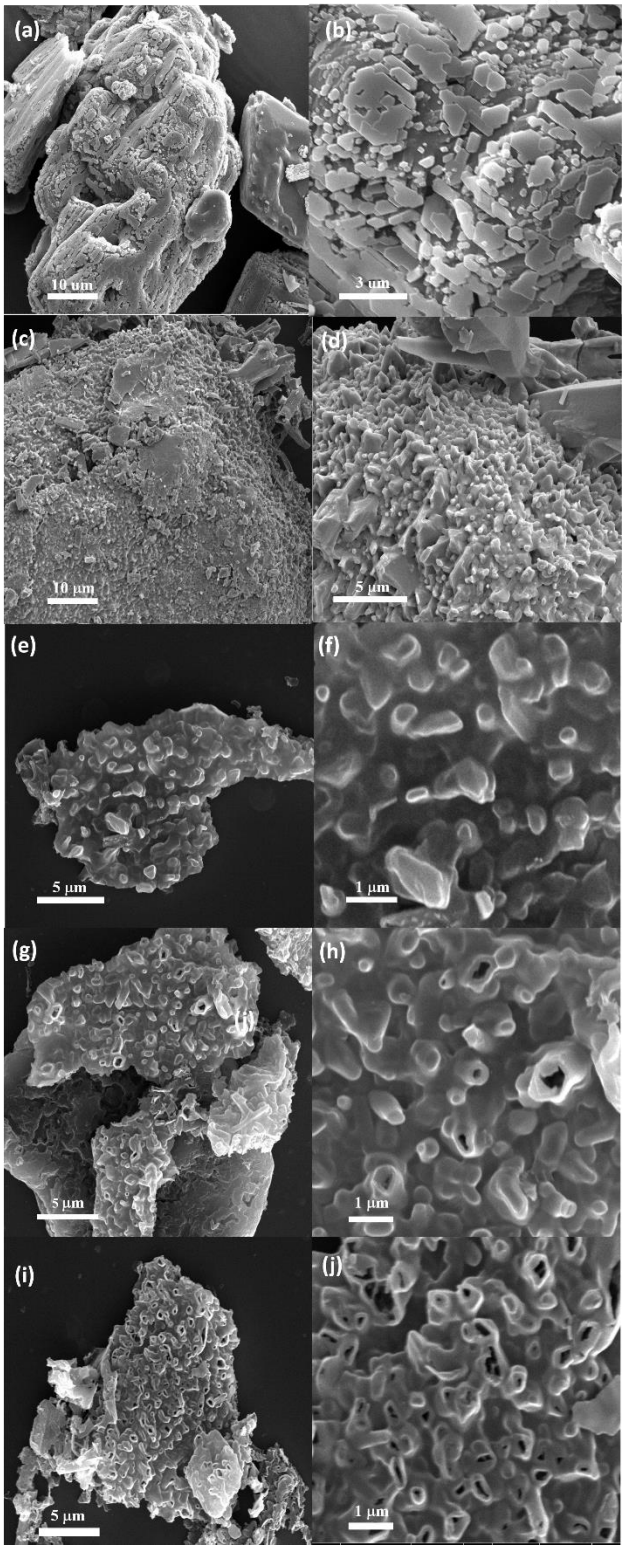

Figure 4.2. SEM micrographs of the products obtained by heating precursors (melamine and cyanuric acid) at different temperature. (a)(b): 300 ˚C; (c)(d): 400 ˚C; (e)(f): 500 ˚C; (g)(h): 550 ˚C; (i)(j): 550 ˚C-1 h.

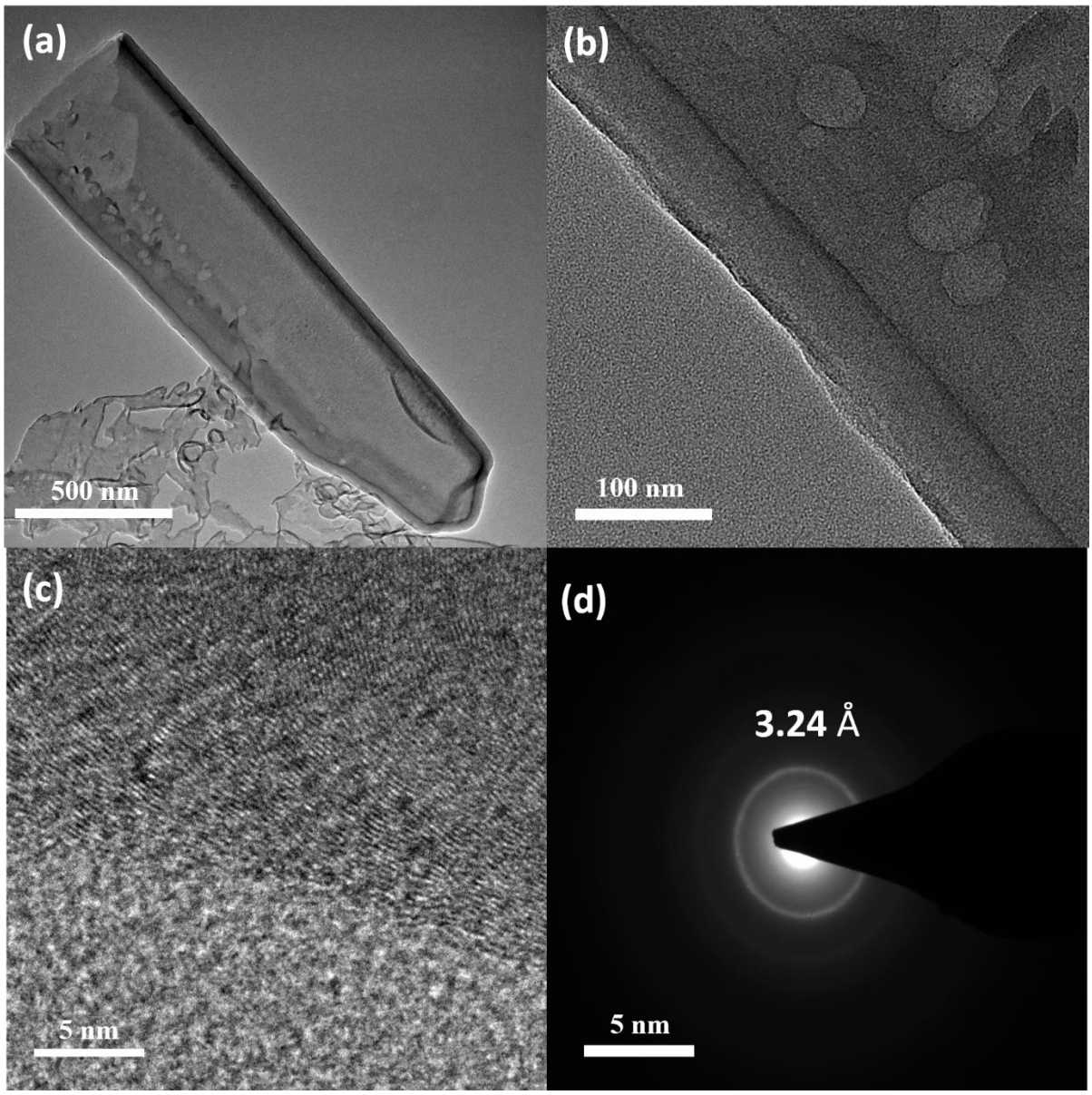

Figure 4.3. (a)(b): TEM images of C-550, the nanotube had the length of 1.2 μm and the diameter of 400 nm, the wall thickness was 70 nm. Pores (40 nm) were found on the tube body; (c): Magnified picture of the tube wall showed lots of g-C_3N_4 layers stacking; (d): diffraction pattern showed the interlayer distance was 3.24 Å of g-C_3N_4 layers.

Figures 4.4 (a)-(d) show the microstructure of C-620 and bulk g-C_3N_4, respectively. C-620 possessed porous and nanosheet structure. Compared with C-550 which only possessed several pores on the tubes, the pores with a much larger size of 20-100 nm have been found almost everywhere on the nanosheet. Bulk g-C_3N_4 showed a thick, bulky and sheet-like

structure, which should be formed by the great aggregation of g-C_3N_4 layers as reported by another researcher. [33] During the synthesis of C-550, melamine and cyanuric acid were heated from room temperature (around 25 ˚C) to 550 ˚C and stayed at 550 ˚C for 4 h. According to Wang et al.'s study and Figure 4.2, these chemicals formed nanorods-like structures by hydrogen bond first, with the temperature further increased to 550 ˚C the nanorods would transform to nanotube structure [26]. In this study, the samples were also continued to be heated to 620 ˚C. It was found that the nanotubes could not withstand high temperature and they opened to become nanosheets. In the synthesis of bulk g-C_3N_4, only melamine was used in the fabrication so there was no nanorod structure formation [26]. Judging by the great aggregation of bulk g-C_3N_4, it is concluded that this nanorod structure reduced the stacking of g-C_3N_4 layers in the formation of nanotubes and nanosheets. The structure of MWCNTs is shown in Figures (e) and (f). Compared with C-550, MWCNT had slender nanotubes and these nanotubes entangled with each other. The diameter was about 10 nm and the length was about 2-3 μm. The thickness of nanotubes' wall was about 5 nm as shown in Figure 4.4 (f). Contrast to the g-C_3N_4 structure, no pores were detected on the MWCNTs.

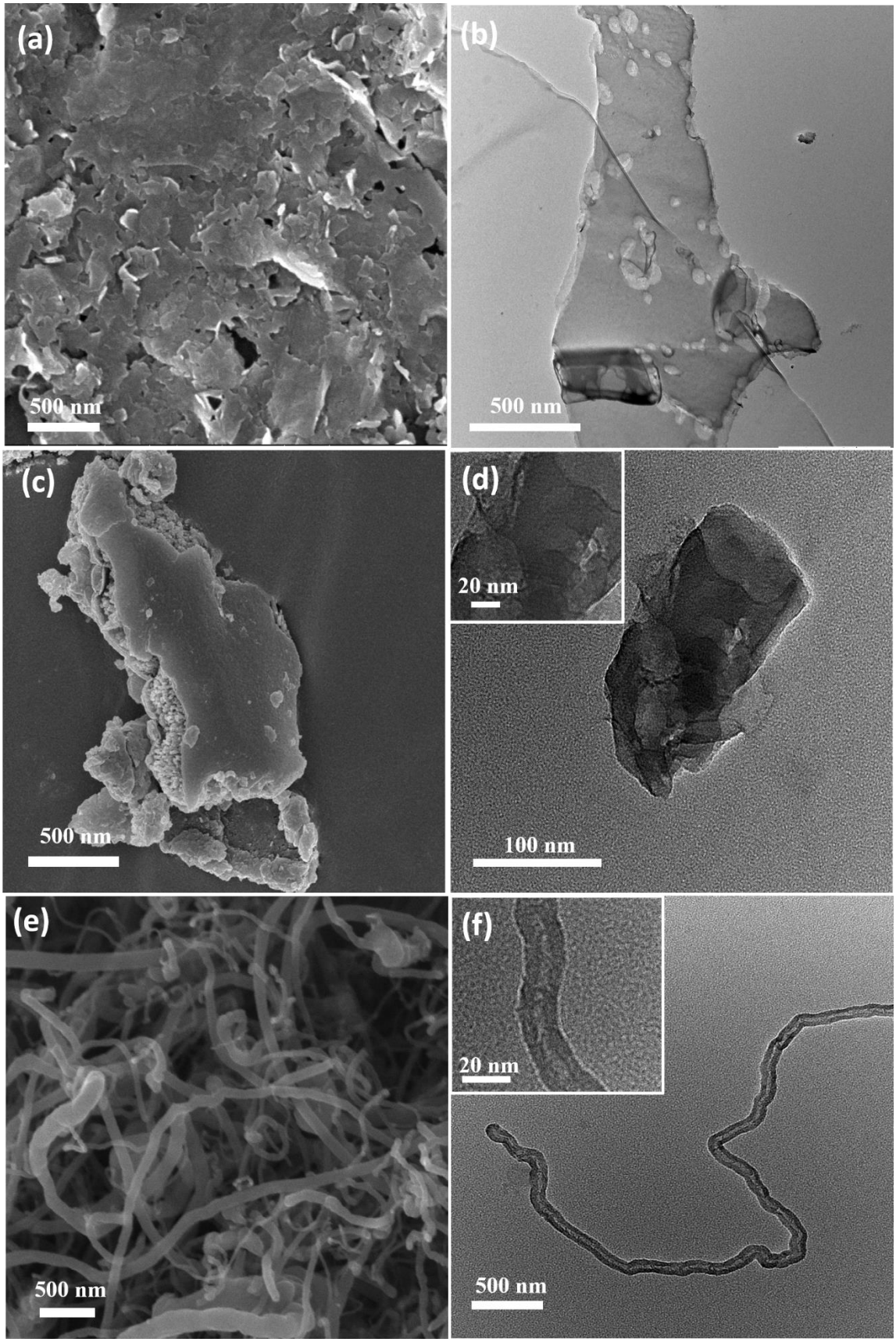

Figure 4.4. (a)(b):SEM and TEM images of C-620; (c)(d):SEM and TEM images of bulk g-C_3N_4 ; (e)(f): SEM and TEM images of MWCNTs.

Figure 4.5 shows the mixture of nickel, melamine, and cyanuric acid (MCN complex) before the heat treatment. The studied sample was named 0.12C-550, suggesting 0.12 g nickel was used in the fabrication. The white particles shown in Figure 4.5 were nickel while other dark particles were cyanuric acid and melamine. After grinding, nickel powders dispersed homogeneously in the mixture and the average size was about 15 μm for small nickel particles. As can be seen in Figure 4.5 (d), bigger nickel particles with the size of 50 μm were also found, which were the result of the aggregation of several small ones. The morphology of Ni- g-C_3N_4 nanotubes obtained by the heat treatment of MCN complex was studied by SEM. The fabrication process was almost the same for the four samples, except different amounts of nickel were added. As shown in Figure 4.6, the products possessed a nanotubular structure with open ends, indicating successful synthesis of nanotubes structure. The diameter of nanotubes varied from 50 to 400 nm suggesting Ni-g-C_3N_4 nanotubes had similar size to the nanotubes of C-550.

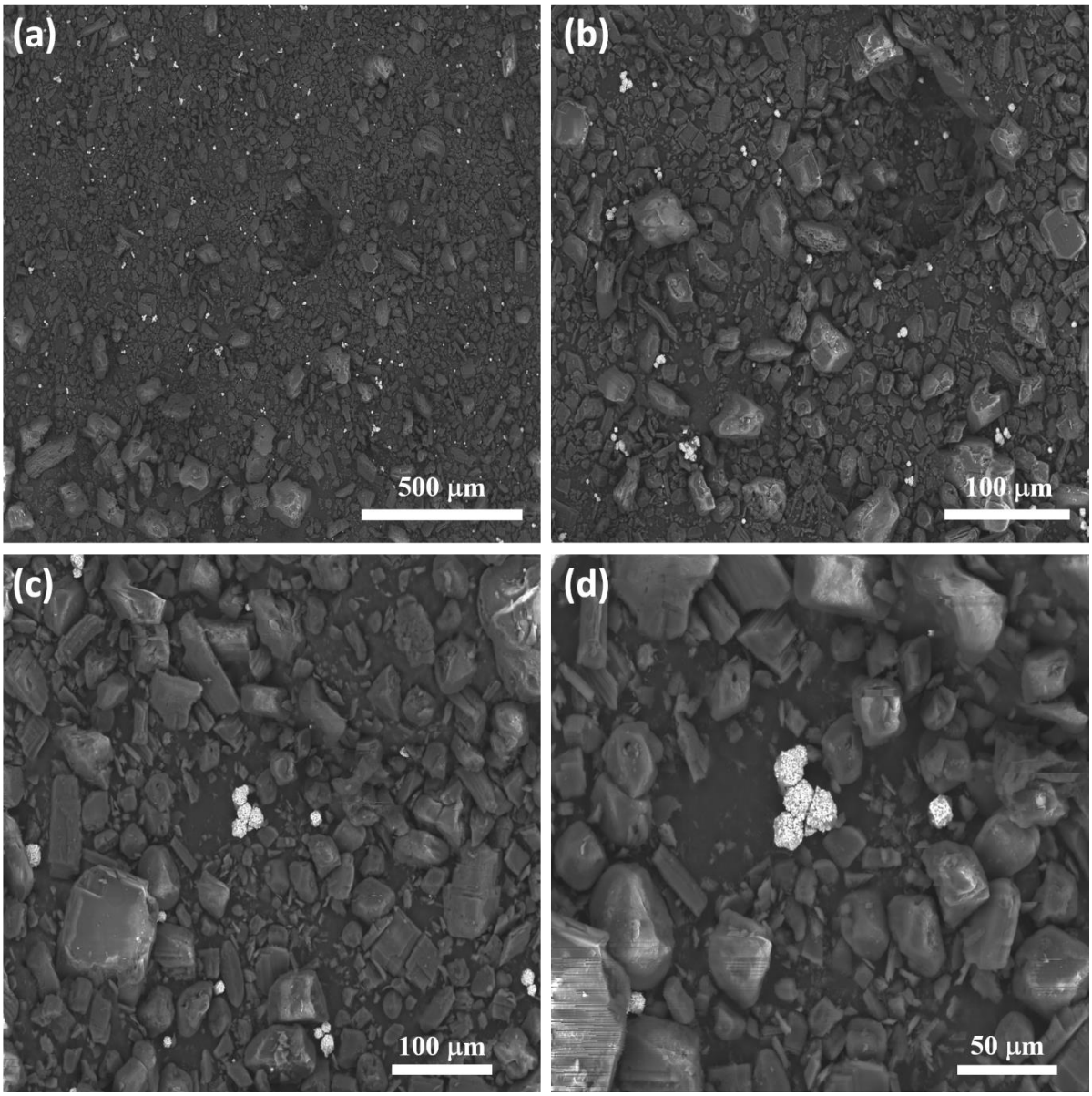

Figure 4.5. SEM images of CMN complex (the sample is 0.12C-550). Nickle particles (white) with the size of 15 μm or 50 μm were observed.

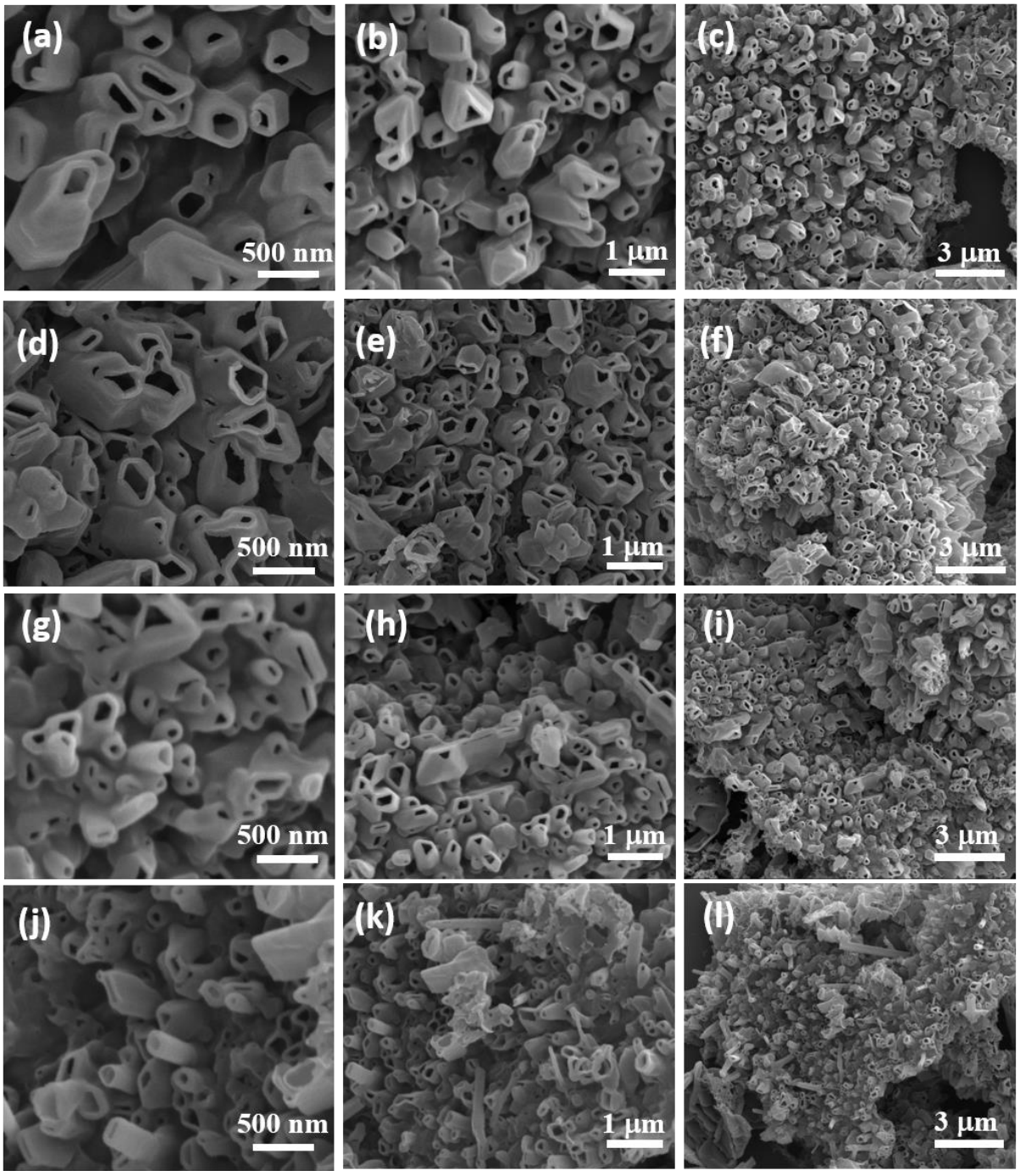

Figure 4.6. SEM images of Ni- g-C_3N_4 nanotubes (a-c: 0.01C-550, d-f: 0.03C-550, g-i: 0.08C-550, j-l: 0.12C-550).

TEM was also applied to study the nanotubes produced via nickel-assisted synthesis; the studied sample was 0.12C-550 which is shown in Figures 4.7 (a)-(d). 0.12C-550 also had pores on the tube body. Compared with C-550 which only had few pores, pores could be found almost

everywhere on 0.12C-550. Interestingly, some pores were brighter while some pores were darker, suggesting the depth of these pores was different. The thickness of walls was about 50 nm and 40 nm which was much smaller than the wall thickness of C-550 (70 nm), indicating the reduced aggregation of g-C_3N_4 layers in the wall. Figure 4.8 shows a small particle spotted in 0.12C-550. The size of this particle is about 20 nm. EDX results confirmed that only nickel and nitrogen signal existed, suggesting the small particle was nickel nitride (Ni_3N).

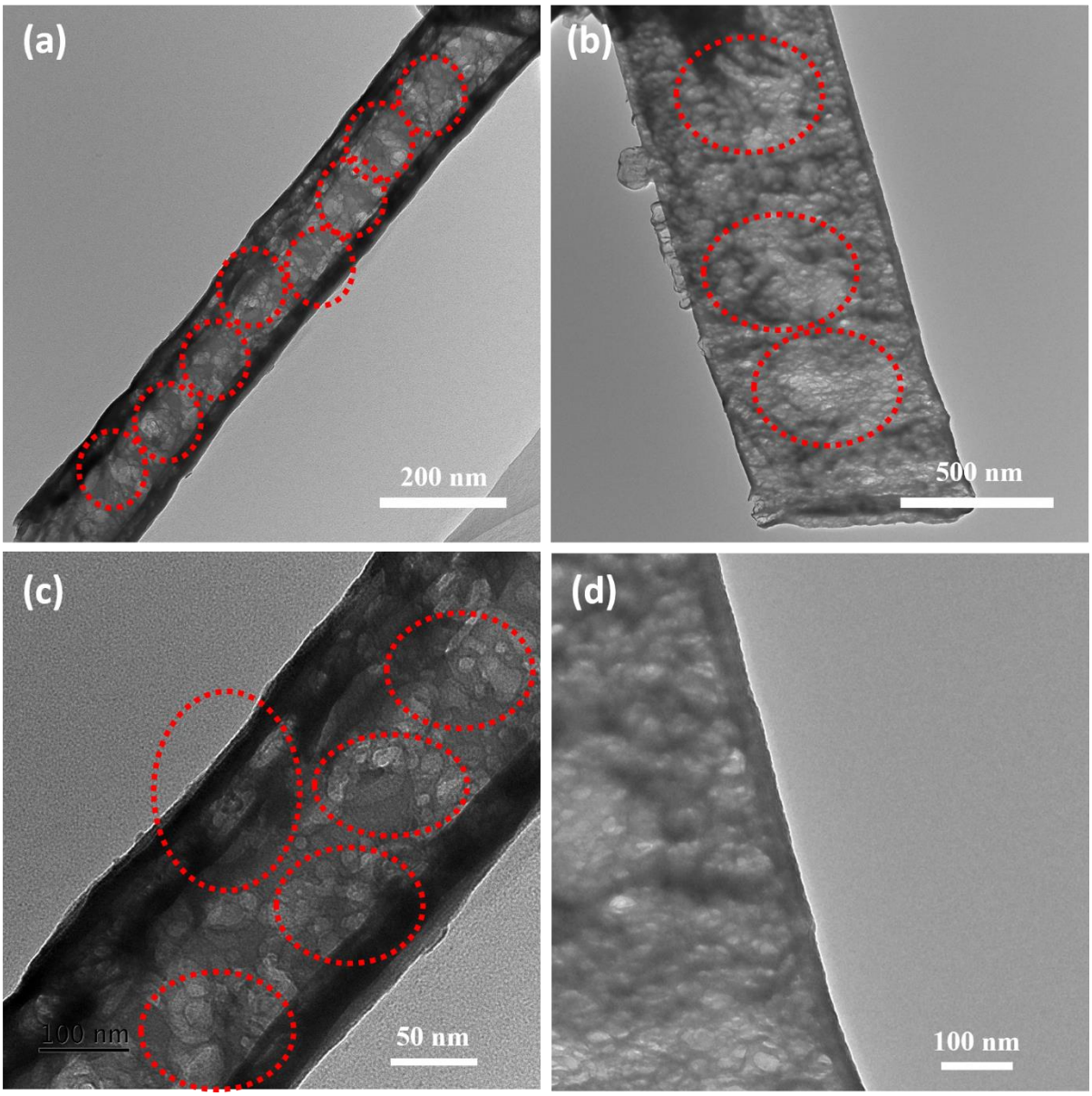

Figure 4.7. TEM images of 0.12C-550, pores (40-50 nm) could be found on the tube body.

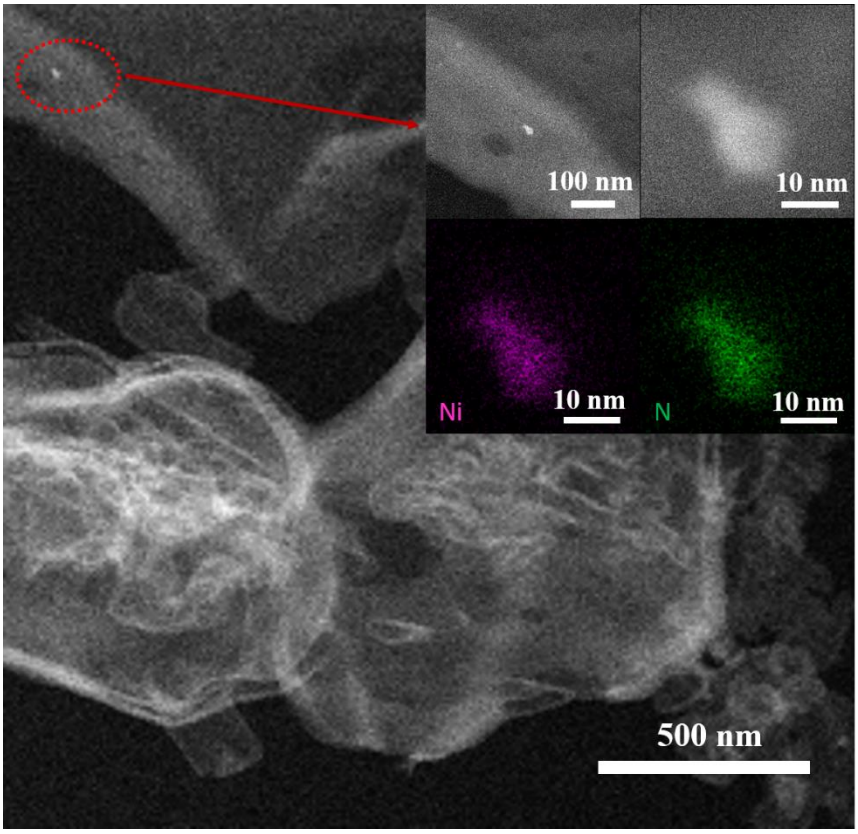

Figure 4.8. Small particle (20 nm) spotted in 0.12C-550, and the EDX result of the small particle.

4.3 XRD Characterization

XRD spectra of C-620, C-550 and bulk g-C_3N_4 are presented in Figure 4.9. Two peaks could be identified in the XRD patterns of all g-C_3N_4 samples, this result was consistent with other people's study [20,26,73,74]. The low-angle peak at 13.1° could be assigned to (100) plane which was associated with in-plane nitrogen linkage of tri-s-triazine, and the high-angle peak between 27° and 28° could be linked to (002) plane which arise from the periodic stacking of conjugated sheets[26]. The peak at 27.7° slightly shifted to a higher angle 28.1° in the spectra of C-620, indicating the structure compaction as the result of polycondensation at higher temperature [80]. Interestingly, the peak at 13.1° was not obvious for C-620 and C-550. One reason is the larger background noise found in C-620 and C-550 (Figure 4.9). The high value of noise might influence the intensity of the low-angle peak at 13.1°. The other reason should be the smaller planar size of nanotube and nanosheet structure [81,82]. The higher angle peak of C-620 and C-550 was also less pronounce compared with the peak of bulk g-C_3N_4, which could be associated with the evident size-dependent properties of tube structure, and smaller size and looser stacking of g-C_3N_4 nanotubes and nanosheets [83]. The XRD pattern of MWCNTs could be found in Figure 4.9 as well. Two strong peaks appeared at 26° and 43.1° corresponding to (002) and (110) reflections [84].

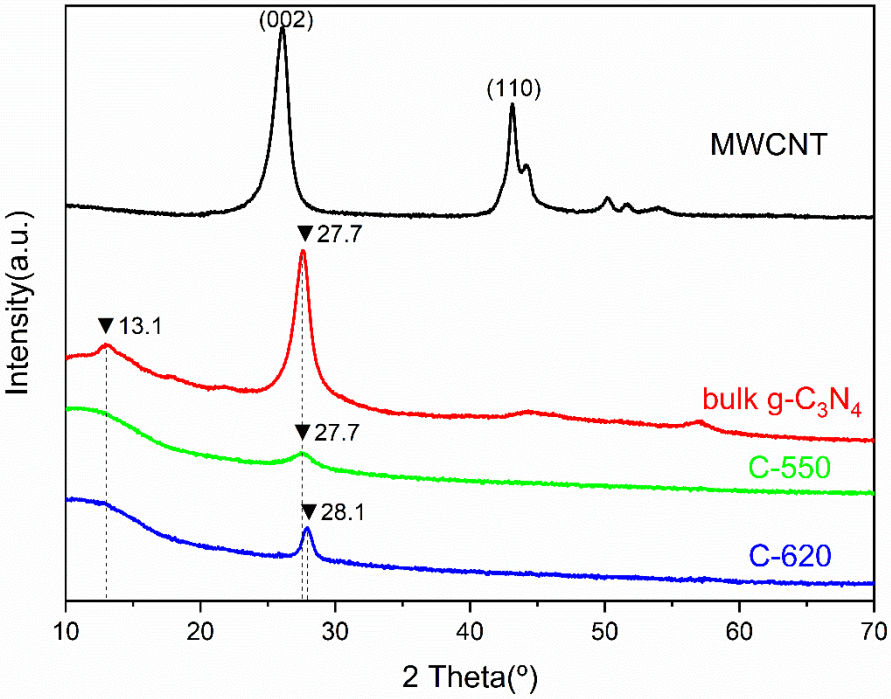

Figure 4.9 XRD of C-550, C-620, bulk g-C_3N_4 and MWCNTs.

Figure 4.10(a) shows the XRD results of the Ni-g-C_3N_4 nanotubes after the heat treatment but before DI water washing. No peaks of nickel but only peaks of nickel nitride (Ni_3N) were spotted. The intensity of the peaks increased with the amount of nickel used (0.01-0.12 g), suggesting more nickel nitride formed during fabrication. To remove the impurities nickel nitride, the synthesised samples were washed by DI water. More details of the washing procedures could be found in Chapter 3. Figure 4.10 (b) shows the XRD spectra of 0.12C-550 and 0.12C-550 before washing. The intensity of nickel nitride reflections decreased largely suggesting the washing was successful and most of nickel nitride has been removed. In order to study the formation process of nickel nitride during synthesis process, XRD patterns of precursor materials (MCN complex) heated at different temperature were also collected, which could be found in Figures 4.11 and 4.12. The studied sample is 0.12C-550. The XRD patterns

of melamine and cyanuric acid are also attached for reference. According to Figure 4.2 which illustrates the formation process of g-C_3N_4 nanotubes (C-550), nanorods structure started to form at 400 ˚C. As the temperature further increased to 550 ˚C, nanotubes appeared as the result of the transformation of nanorods to nanotubes. In Figure 4.11, XRD pattern starts to change after 400 ˚C, corresponding to the formation of nanorods structure. As temperature gradually increased and reached 550 ˚C, nickel nitride was found. After holding at 550 ˚C for 2 hours, nickel could not be found and only nickel nitride remained, suggesting all nickel has reacted to form nickel nitride. Increasing the holding time to 6 h at 550 ˚C (Figure 4.12) resulted in the decomposition of nickel nitride through the loss of nitrogen, hence the nickel peaks reappeared. The heat treatment was conducted in air, so nickel could be oxidized, which explains the presence of nickel oxide. With the holding time increased to 8 h, nickel nitride was fully decomposed and only the peaks of nickel and nickel oxide remained. g-C_3N_4 nanotubes also could not survive after being heated for 8 h at 550 ˚C. According to Wang et al.'s study, NH_3 was released when nanorods transformed to nanotubes [26], which explains why nickel nitride could only be found after 550 ˚C in this study. Since the transformation started at 550 ˚C (Figure 4.2), NH_3 should also start to be released at this temperature. Nickel could only have the chance to react with NH_3 and produced nickel nitride after 550 ˚C. Figure 4.13 presents the XRD patterns of C-550 and other Ni-g-C_3N_4 nanotubes. The peak at 27.7° (002) became broad and weak for these Ni-g-C_3N_4 nanotubes , which should be ascribed to the reduced correlation length of interlayer periodicity of the tris-triazine building blocks [25,85], and the disorder structure caused by pores and defects [86], as confirmed by TEM observation.

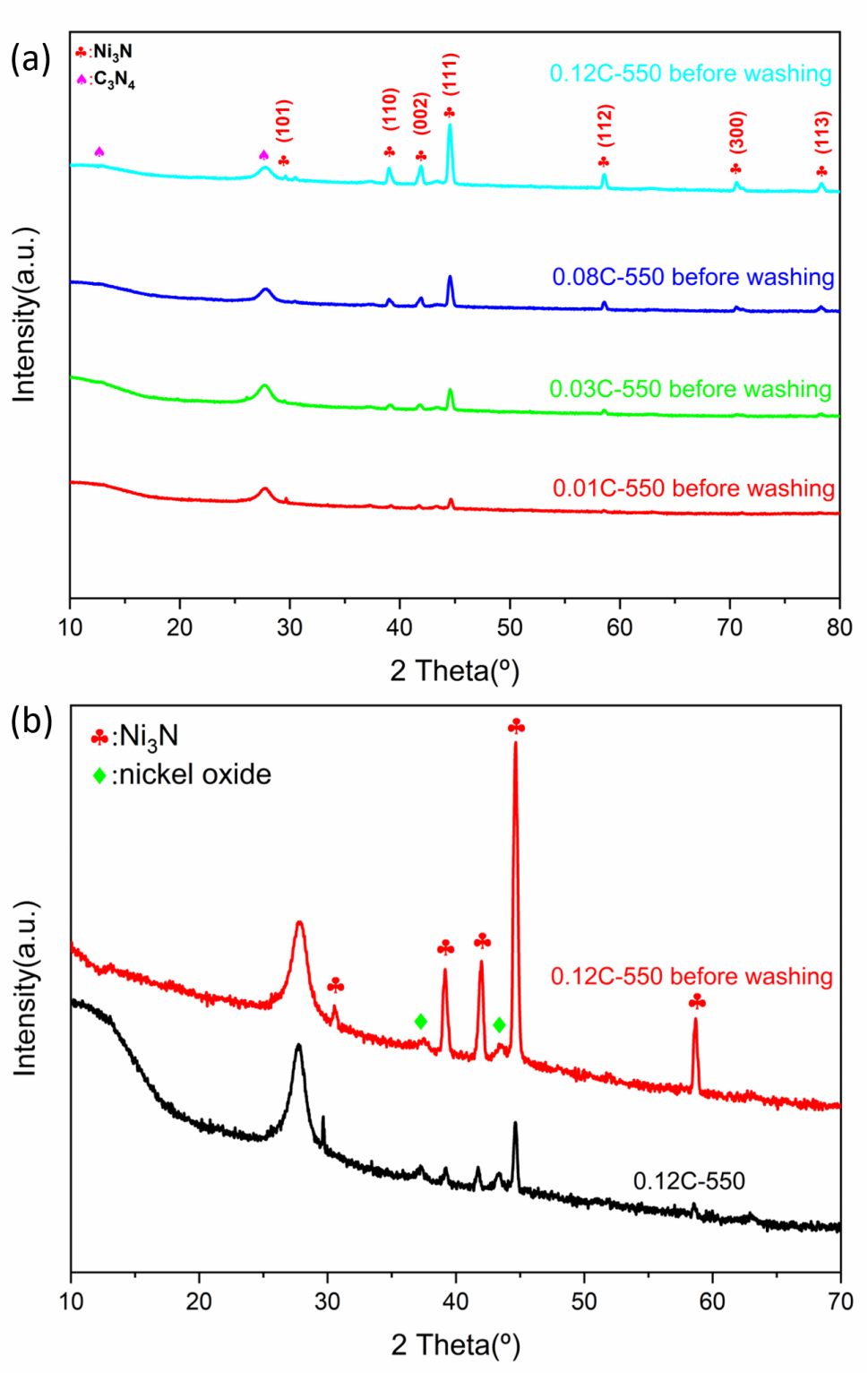

Figure 4.10 XRD of (a) 0.01C-550, 0.03C-550, 0.08C-550 and 0.12C-550 without DI water washing. (b) comparison of XRD pattern of 0.12C-550 and 0.12C-550 before washing.

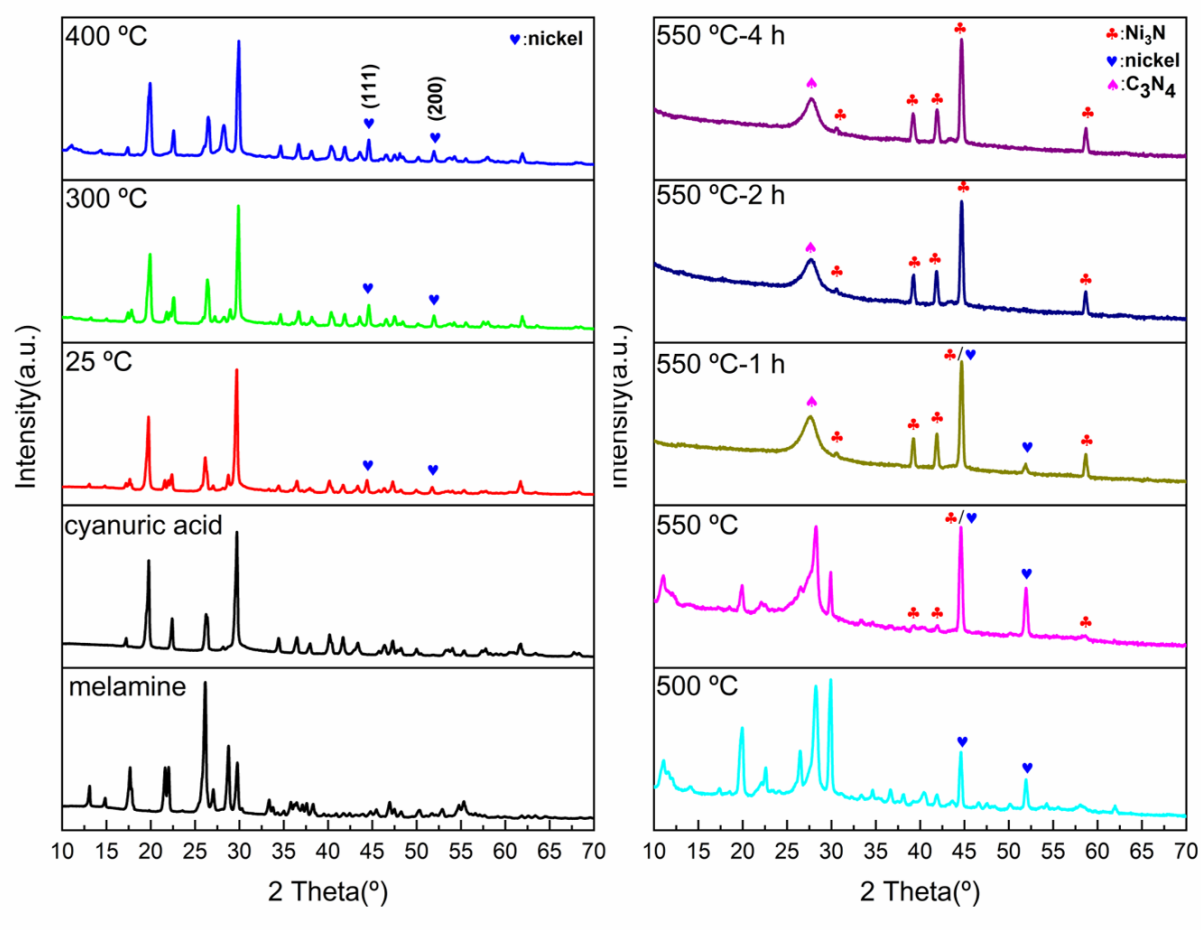

Figure 4.11 XRD of precursor (MCN complex) treated at different temperature, the patterns of melamine and cyanuric acid are also attached.

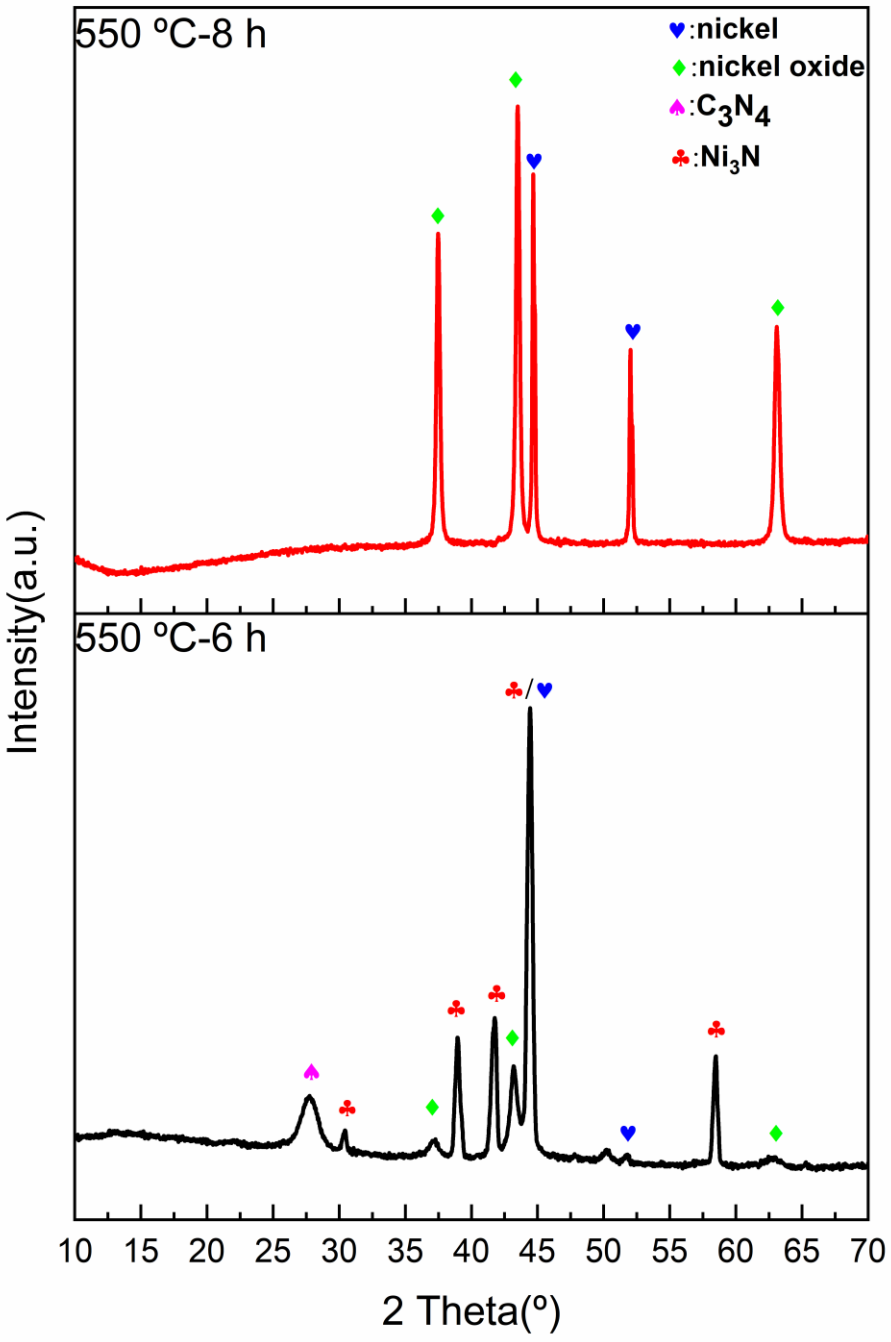

Figure 4.12 XRD of precursor (MCN complex) treated at 550 ˚C for 6 h and 8 h.

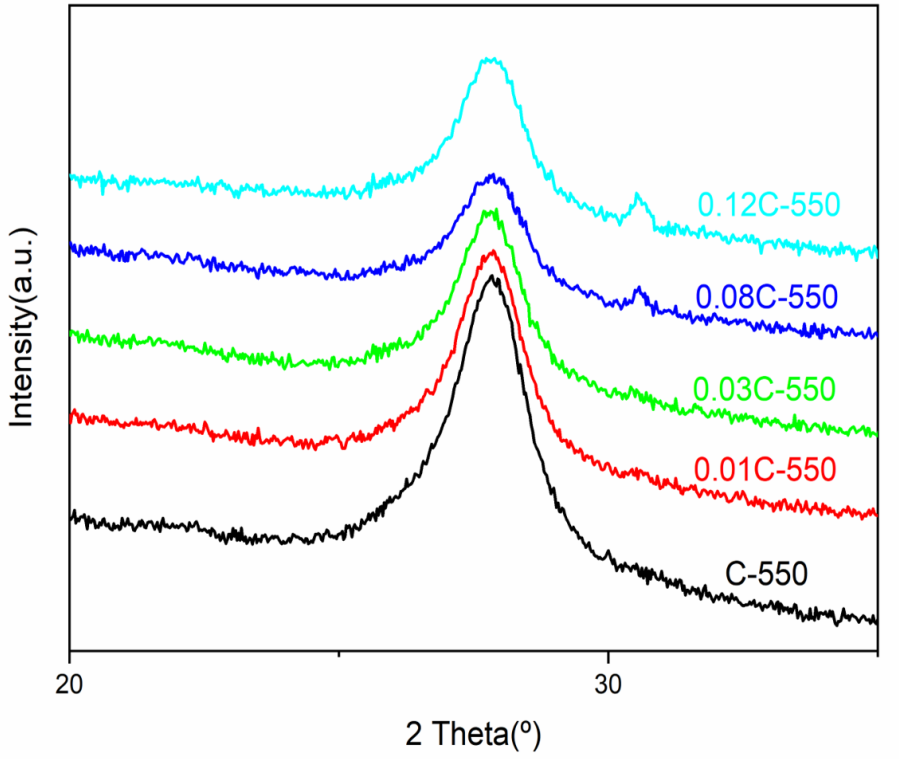

Figure 4.13 XRD pattern obtained in 20-40° of C-550 and nickel-assisted synthesis samples.

4.4 Surface Analysis

The surface area can influence the hydrogen storage performance of materials. For physisorption, the bigger surface area the material has, the more active sites it can provide for hydrogen adsorption [87]. For this reason, the surface area and pore distribution of the carbonaceous materials included in this work were investigated by N_2 adsorption/desorption isotherms. Figure 4.14 (a) shows the N_2 physisorption isotherms of MWCNTs, bulk g-C_3N_4, C-550 and C-620. The isotherms were typical IV isotherms for all samples, the high relative pressure (P/P°) of hysteretic loop suggests the existence of mesopores [10]. The data generated

from the isotherms are given in Table 4.1. It could be found that C-550 and MWCNTs had similar BET surface area and pore volume. Bulk g-C_3N_4 has the smallest values of BET surface area (10.98 m^2/g) and pore volume (0.06 cm^3/g) in all g-C_3N_4 materials, which should be explained by the great aggregation of g-C_3N_4 layers as confirmed by TEM observation (Figure 4.4). Considering the interlayer distance of g-C_3N_4 was about 0.324 nm and the size of nitrogen molecule was about 0.364 nm, it is hard for nitrogen to diffuse into the layers of g-C_3N_4 and be adsorbed [33,88]. C-620 had the largest surface area and pore volume in all g-C_3N_4 materials which could be attributed to the thin and highly porous structure as confirmed by SEM and TEM. The pore distribution (Figure 4.14 (b)) also showed C-620 had a great volume for the pores with the size of 20-100 nm compared with other samples. This finding was consistent with the TEM observation in Section 4.2 and confirms the porous structure of C-620. The highly porous structure of C-620 could be explained by the thermal oxidization of the tri-s-triazine units in the g-C_3N_4. Li et al. once fabricated porous g-C_3N_4 nanosheets by calcining bulk g-C_3N_4 at 550 $^{\circ}$C in air and found that the increase of the calcination time resulted in the thermal oxidization of the tri-s-triazine units consisted of C-N bonds, thus encouraging the formation of porous structure of g-C_3N_4 nanosheets [89]. Besides, the thermal oxidization of tri-s-triazine units broke the weak molecular force between the g-C_3N_4 layers, thus reducing the aggregation of g-C_3N_4 layers [90]. In the present study, g-C_3N_4 nanosheets were synthesized at 620 $^{\circ}$C (C-620) instead of 550 $^{\circ}$C which was the heat treatment temperature designated for bulk g-C_3N_4 and g-C_3N_4 nanotubes (C-550). The higher calcination temperature of C-620 may also result in a severe thermal oxidation and create lots of defects and reduce the aggregation, similar to the extended calcination time as reported by Li et al., and thus a thin and highly porous structure of g-C_3N_4 nanosheets was obtained.

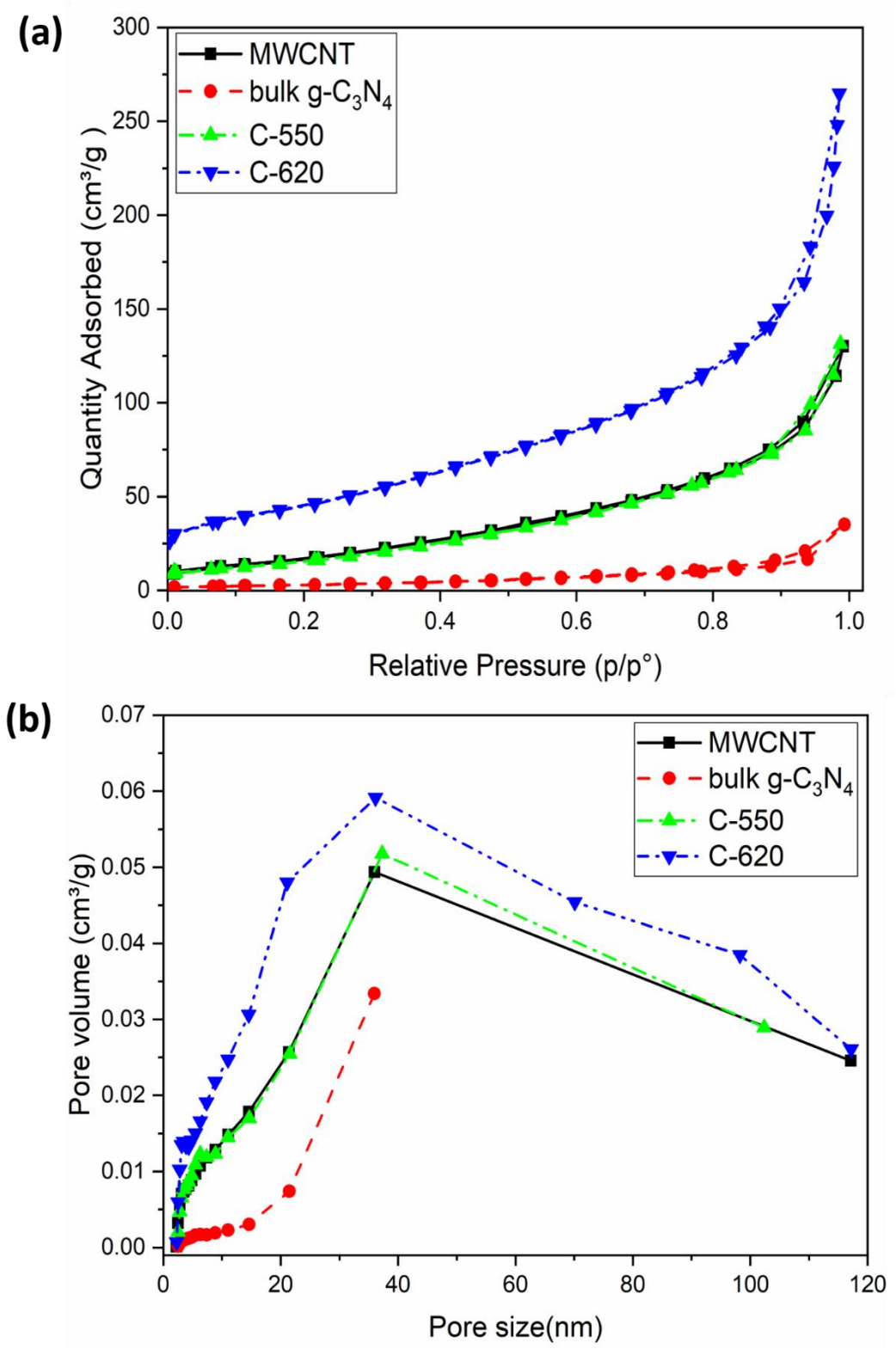

Figure 4.14. (a) N_2 adsorption/desorption isotherm. (b) Pore size distribution curves of MWCNTs, bulk g-C_3N_4, C-550 and C-660.

Sample	BET surface area(m^2/g)	Pore volume(cm^3/g)	Average pore size(nm)
MWCNTs	61.31	0.23	8.91
Bulk g-C_3N_4	10.98	0.06	13.67
C-550	59.38	0.23	9.24
C-620	161.02	0.43	9.73

Table 4.1. BET surface area, pore volume and average pore size of bulk g-C_3N_4, C-550 and C-620.

Figure 4.15 shows the N_2 physisorption isotherms of nickel-assisted synthesis g-C_3N_4 nanotubes. Compared with C-550 which adsorbed 146 cm^3/g nitrogen, the maximum adsorbed nitrogen of nickel-assisted synthesis samples increased with the nickel amount. In the case of 0.12C-550, the adsorbed N_2 reaches 230 cm^3/g. Table 4.2 presents the data generated from the isotherms. With the increase of nickel used in the fabrication, the BET surface area, pore volume and average pore size increased. These increased values could be attributed to the reduced aggregation of g-C_3N_4 layers and highly porous structure as resulted from steam reforming etching [33], as confirmed by XRD and TEM. It is postulated that increasing the amount of nickel used in the fabrication triggered more decomposition of NH_3 gas to produce hydrogen. The water molecules formed from the resulting hydrogen may enhance etching and reduce aggregation. Thus, the surface area and pore volume increased with nickel. It was found that the increased pore volume belonged to the pores with the sizes between 20 nm and 100 nm. This finding was consistent with the TEM observation in Figure 4.7).

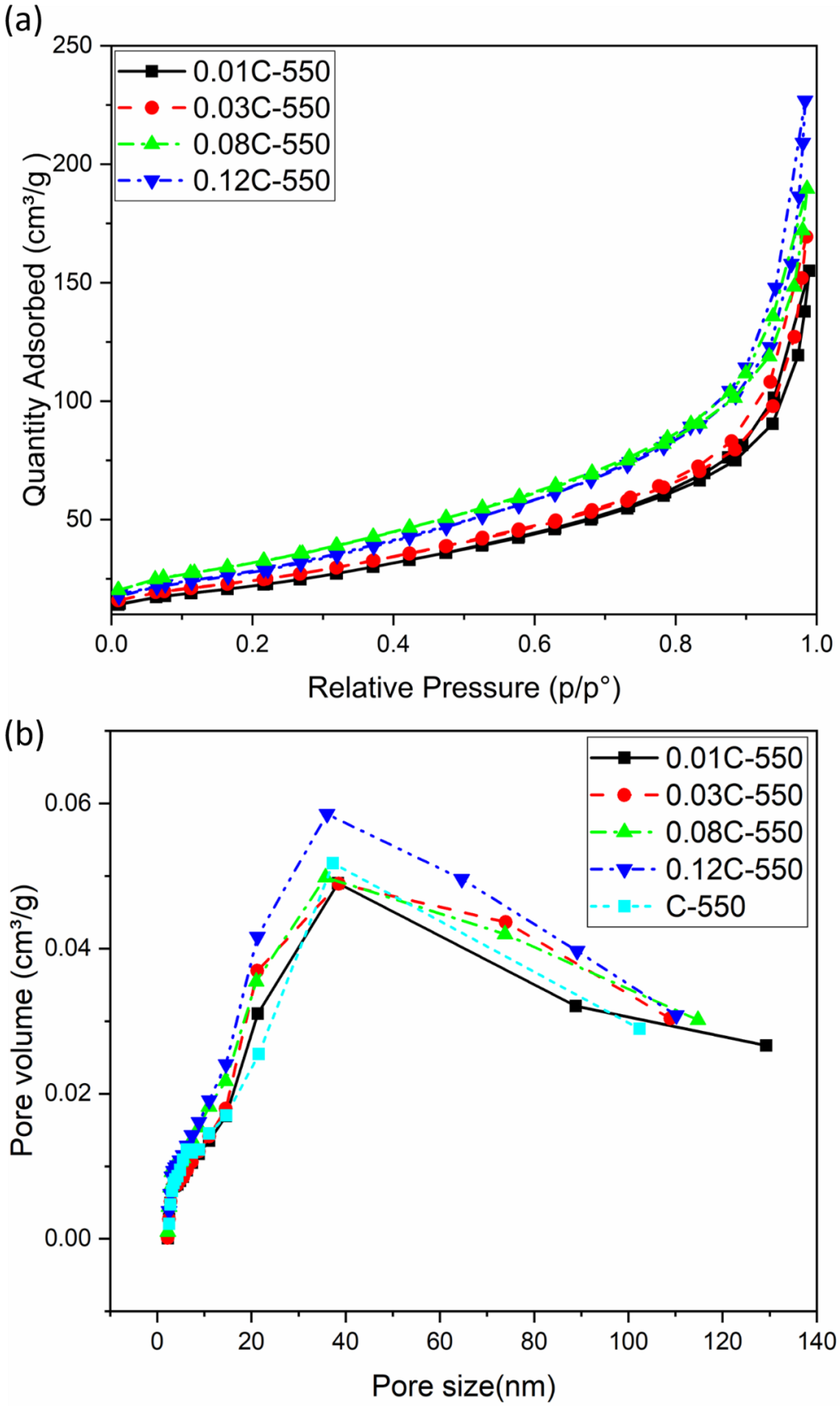

Figure 4.15. (a) N_2 adsorption/desorption isotherm. (b) Pore size distribution curves of nickel-assisted synthesis samples.

Sample	BET surface area(m^2/g)	Pore volume(cm^3/g)	Average pore size(nm)
C-550	59.38	0.23	9.24
0.01C-550	81.18	0.25	10.64
0.03C-550	88.43	0.28	11.16
0.08C-550	103.07	0.38	11.38
0.12C-550	116.77	0.40	11.28

Table 4.2. BET surface area, pore volume and average pore size of nickel-assisted synthesis samples. The information of C-550 is also attached for reference.

4.5 XPS Analysis and ICP Analysis

X-ray photoelectron spectroscopy (XPS) was used to probe the chemical composition of g-C_3N_4 materials (bulk, nanotubes and nanosheets). Figure 4.16 (a) shows the XPS survey spectra of the samples studied. The peaks at 288 eV, 399 eV and 532 eV corresponded to C1s, N1s and O1s, respectively. The weak signal from O1s could be attributed to the adventitious adsorbed water [91]. Figures 4.16 (b) and (c) show the C1s and N1s spectra of all g-C_3N_4 samples. There was not big difference in the spectra, suggesting that the samples had similar chemical composition. High resolution C1s spectra could be fitted to three peaks. The broad peak across 284 and 286 eV was assigned to C-C/C=C and C-H bond which were usually found in XPS characterization of g-C_3N_4 [92,93]. The peak at 286.4 eV and 288.3 eV corresponded to C-NH_x $_{(1,2)}$ on the edge of heptazine units and N=C-N coordination in the framework of g-C_3N_4, respectively [84]. The N1s pattern also could be further deconvoluted into three peaks. The

strong peak on the left was ascribed to bicoordinated N atoms (N_2C). And the peaks at 400.09 eV and 401.2 eV were assigned to tricoordinated N (N_3C) atoms and NH_x groups in the heptazine framework, respectively [94]. It should be noted that the bicoordinated N in N1s spectra of C-620 showed a left shift of 0.1-0.2 eV, which could be explained by re-distribution of electrons caused by the nitrogen defects and higher crystallinity of C-620 [95]. The C/N ratios of C-620, C-550 and bulk g-C_3N_4 are provided in Table 4.3, which were 0.76, 0.72 and 0.7, respectively. These values approached the theorical C/N ratio of graphitic carbon nitride (0.75) [26]. The high C/N ratio of C-620 suggested the great loss of nitrogen during fabrication which should be caused by the thermal oxidization, as reported by other groups [90,96].

Sample	C (%)	N (%)	O (%)	C/N ratio
C-620	42.46	55.83	1.69	0.76
C-550	41.21	57.13	1.66	0.72
Bulk g-C_3N_4	39.67	56.64	0.55	0.70

Table 4.3. C/N ratios of C-620, C-550 and bulk g-C_3N_4 obtained by elemental analysis.

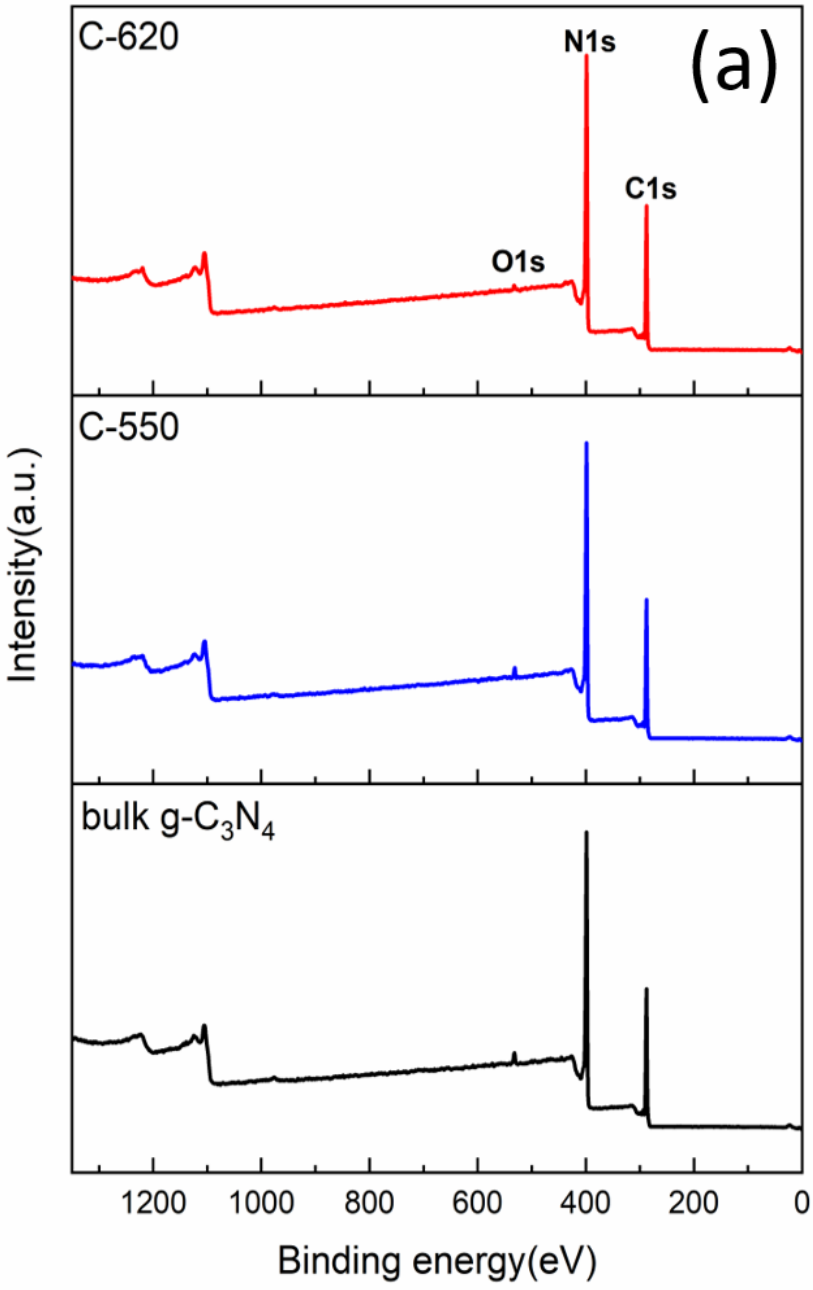
C-620
N1s
(a)
C1s
O1s
C-550
bulk g-C3N4
Intensity(a.u.)
1200
1000
800
600
400
200
0
Binding energy(eV)

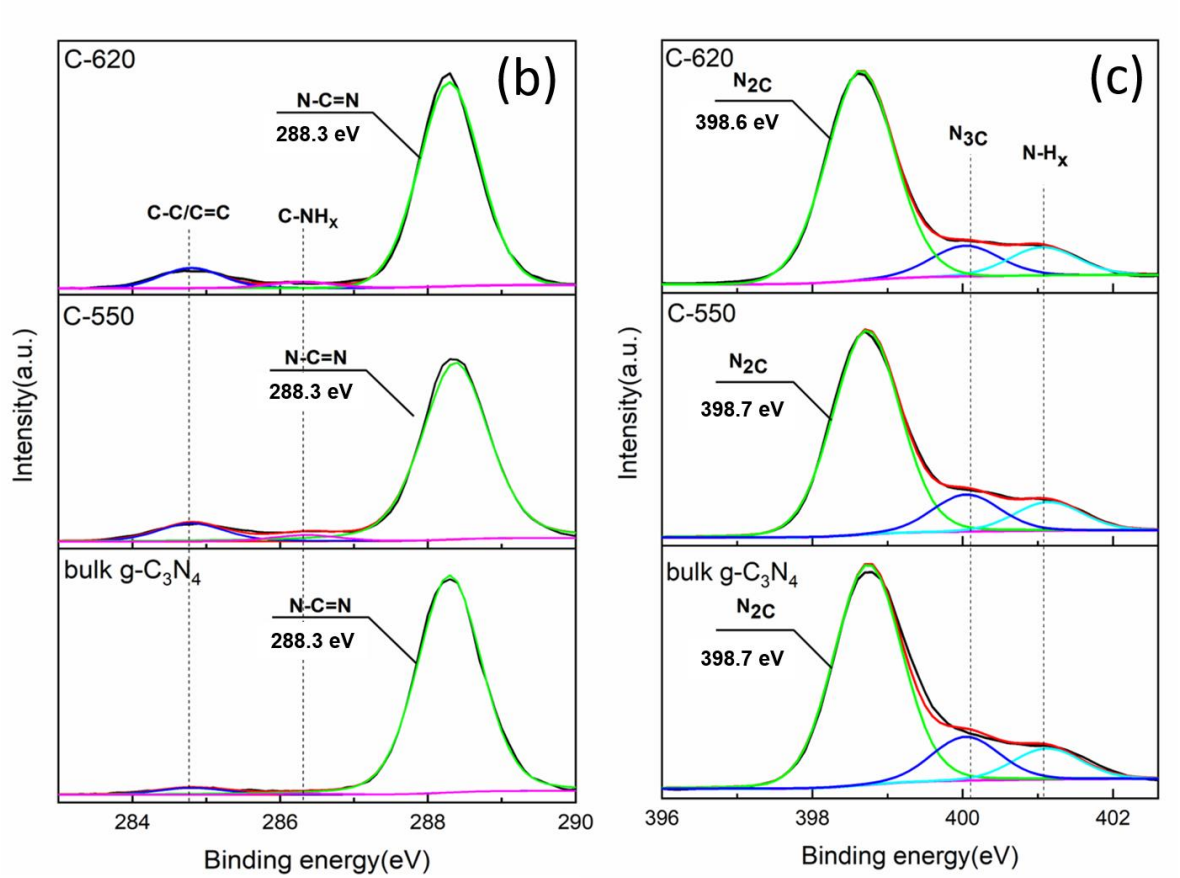

Figure 4.16. (a) XPS survey spectra of C-620, C-550 and bulk g-C_3N_4. High resolution (b) C1s spectra of C-620, C-550 and bulk g-C_3N_4. (c) N1s spectra of C-620, C-550 and bulk g-C_3N_4.

XPS was also used to study nickel-assisted synthesis g-C_3N_4 nanotubes. Figure 4.17 presents the N1s and C1s spectra of nickel-assisted synthesis g-C_3N_4 nanotubes. No obvious shift in binding energy indicated there was no change in chemical state of C and N. The C1s spectra of those nickel-assisted synthesis g-C_3N_4 nanotubes could be fitted to three peaks: C-C/C=C at 248.8 eV, C-NH_x at 286.4 eV, N-C=N at 288.3 eV [94]. The N1s spectra could also be divided into three peaks which are corresponding to bicoordinated N, tricoordinated N and NH_x, respectively [94].

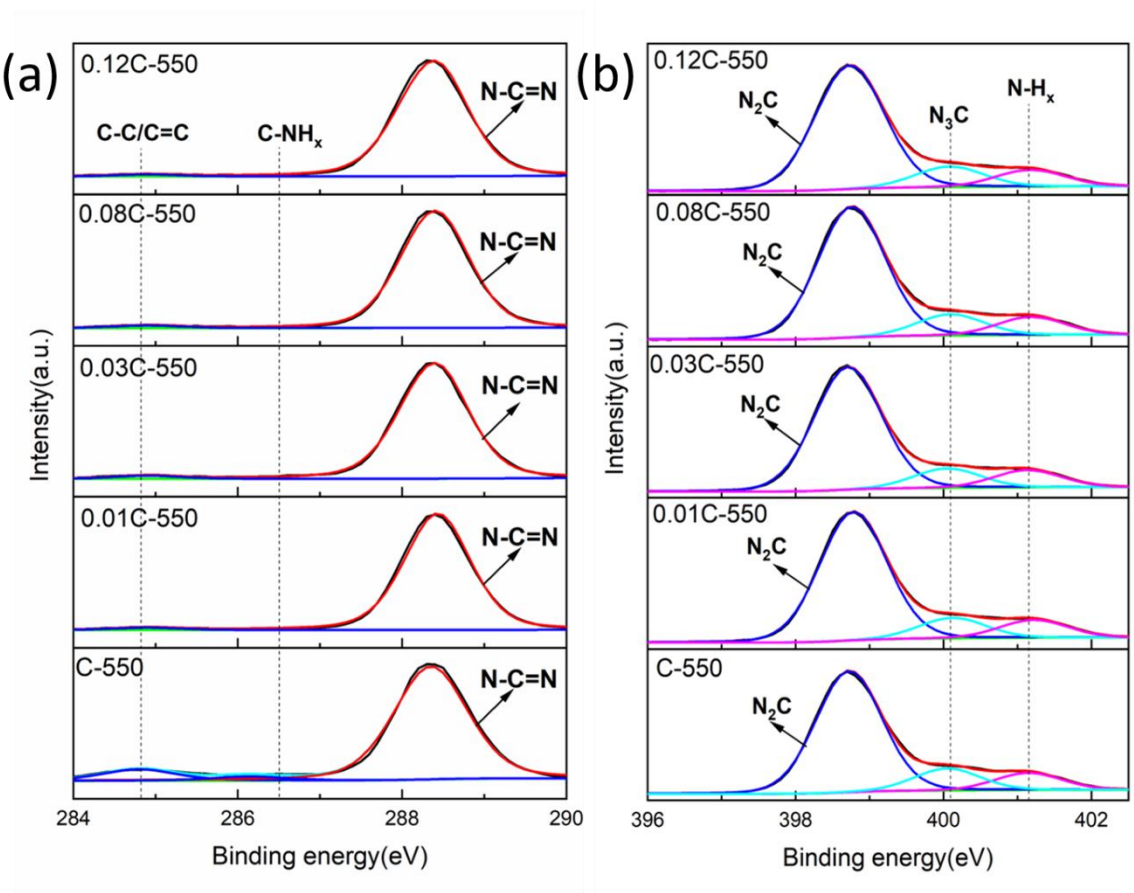

Figure 4.17. High resolution (a) C1s spectra of Ni-g-C_3N_4 nanotubes and (b) N1s spectra of nickel-assisted synthesis g-C_3N_4 nanotubes (the spectra of C-550 are also attached for reference).

The elemental analysis results of Ni-g-C_3N_4 nanotubes could be found in Table 4.4. Compared with C-550, the atomic ratio of C decreased, and the C/N ratio also decreased, indicating carbon vacancies [32,33]. Clearly, the nanotubes surface was poor in carbon, suggesting the steam reforming process preferred to proceed with the loss of carbon then nitrogen. According to the study of thermal oxidization etching found in C-620 (Table 4.3) or in other research, the thermal etching preferred to proceed with the oxidization of nitrogen than carbon [90,96]. The loss of carbon atoms found in Ni-g-C_3N_4 nanotubes indicated the steam reforming mechanism is different from the mechanisms of thermal oxidization etching. In addition, only very small amount of nickel (atomic ratio 0-0.02 %) was found in these samples. Table 4.5

presents the nickel content before and after washing determined by ICP. The content of nickel decreased significantly after washing. The reduced nickel content found in XPS and ICP suggest most of impurity nickel nitride has been removed in washing process which is consistent with XRD result (Figure 4.10). With the increase of nickel loading (from 0.01 to 0.12), the atomic ratio of C-C/C=C and C-NH_x in C1s spectra (Figure 4.18 and Table 4.6) gradually decreased, implying the loss of carbon occurring at graphitic carbon species and C-NH_x lattice sites [32]. The ratios of N_3C and NH_x also decreased in N1s spectra for Ni-g-C_3N_4 nanotubes (table 4.7), suggesting the loss of nitrogen occurring at N_3C and NH_x lattice sites [33,32].

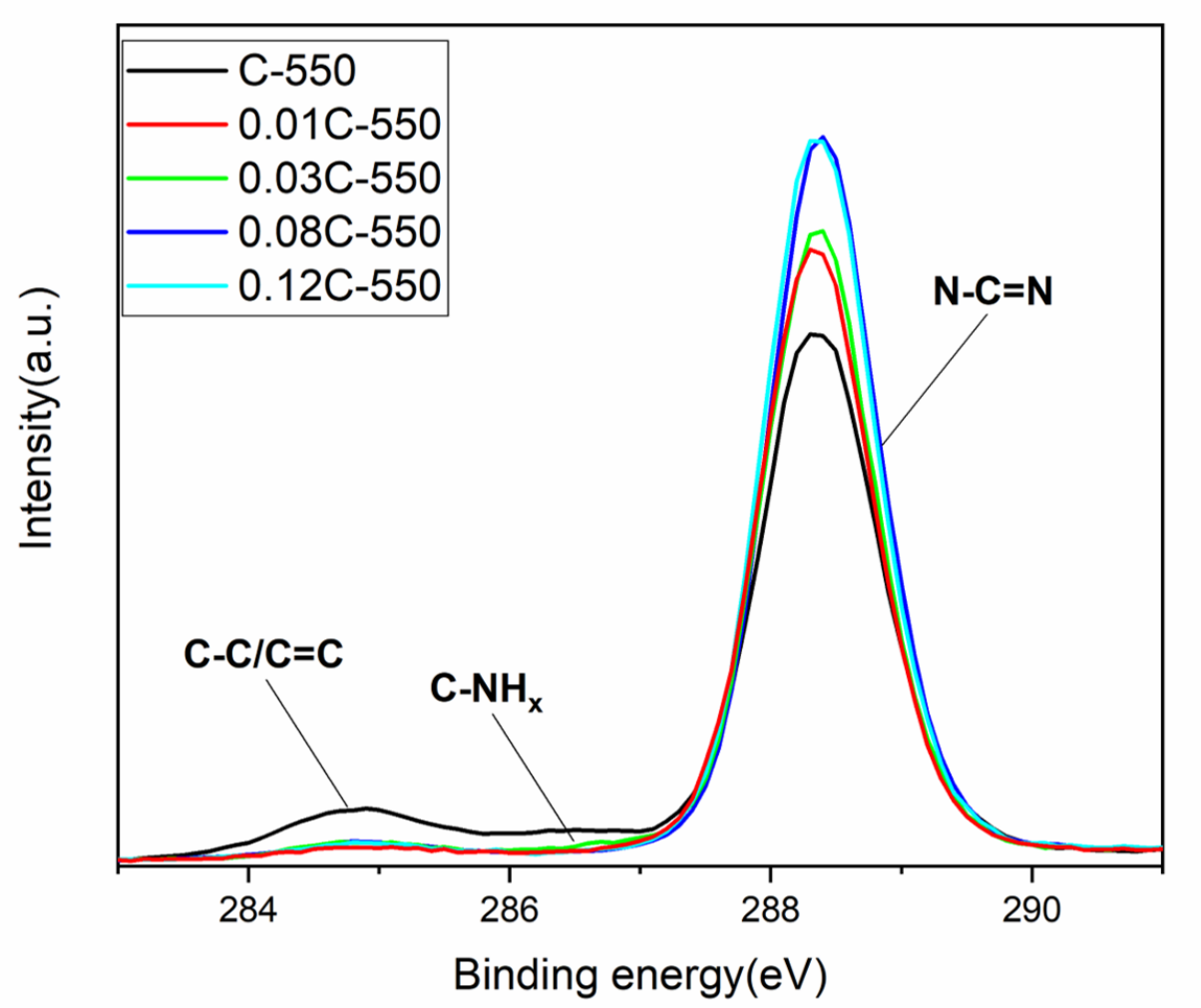

Figure 4.18. High resolution C1s spectra of nickel-assisted synthesis g-C_3N_4 nanotubes and C-550.

Figure 4.19 presents the O1s spectra of Ni-g-C_3N_4 nanotubes . Basically, the spectra of O1s could be fitted into three peaks: adsorbed water molecule at 533 eV, C=O at 531.9 eV and Ni=O at 530.1 eV [97,98]. Ni=O found in the spectrum of 0.12C-550 should be attributed to nickel oxide formed during the heat treatment. C=O could only be found in Ni-g-C_3N_4 nanotubes . The appearance of C=O in Ni-g-C_3N_4 nanotubes could be resulted from the steam reforming etching which made the samples vulnerable to oxidization [33]. The reason should be the removal of carbon and nitrogen atoms breaking the bonds with other carbon atoms on tri-s-triazine units or graphitic species thus making the structure unstable. These non-fully bonded carbon atoms on the units formed double bond with oxygen atoms in air and restabilized the structure.

Sample	C (%)	N (%)	O (%)	Ni(%)	C/N ratio
C-550	41.21	57.13	1.66	0.00	0.72
0.01C-550	40.84	58.29	0.86	0.01	0.70
0.03C-550	40.63	58.41	0.94	0.02	0.70
0.08C-550	40.61	58.56	0.81	0.02	0.68
0.12C-550	40.01	58.44	1.53	0.02	0.68

Table 4.4. C/N ratios of Ni-g-C_3N_4 nanotubes (the data of C-550 are also attached for reference).

	0.01C-550	0.03C-550	0.08C-550	0.12C-550
Before washing (wt.%)	3.3	7.7	18.1	30.1
After washing (wt.%)	2.5	3.3	4.5	5.8

Table 4.5. Nickel content in Ni-g-C_3N_4 nanotubes before and after washing.

Sample	N-C=N (%)	C-C/C=C (%)	C-NHx (%)
C-550	85.39	9.39	5.22
0.01C-550	95.59	2.43	1.66
0.03C-550	95.76	2.84	1.39
0.08C-550	95.96	2.69	1.36
0.12C-550	97.28	1.53	1.19

Table 4.6 Relative ratios of N-C=N, C-C/C=C and C-NH_x in Ni-g-C_3N_4 nanotubes determined by C1s spectra (the data of C-550 are also attached for reference).

Sample	N_2C (%)	N_3C (%)	N-Hx (%)
C-550	75.90	13.36	10.74
0.01C-550	78.20	11.61	10.60
0.03C-550	78.50	11.20	10.30
0.08C-550	78.37	11.40	10.24
0.12C-550	78.33	11.69	9.97

Table 4.7 Relative ratios of N_2C, N_3C, NH_x in Ni-g-C_3N_4 nanotubes determined by N1s spectra (the data of C-550 are also attached for reference).

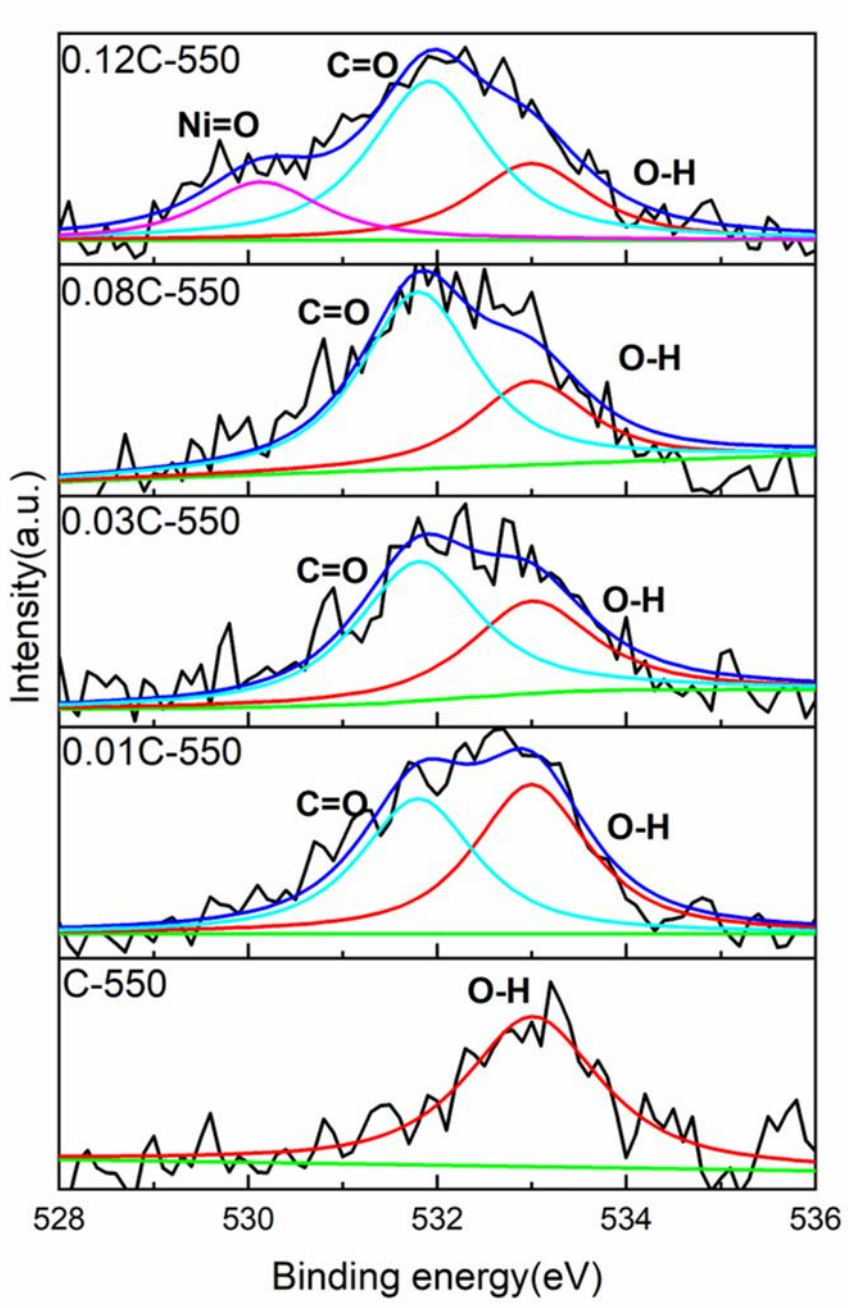

Figure 4.19. High resolution O1s spectra of Ni-g-C_3N_4 nanotubes.

4.6 FTIR Analysis

The chemical information of carbon nitride-based materials was further investigated by FTIR. Figure 4.20 (a) presents the FTIR results of g-C_3N_4, C-550 and C-620, the patterns were similar suggesting that they had similar chemical structure, corresponding to the former discussion. The strong stretching vibration at 820 cm^{-1} corresponded to breathing mode of the triazine units[26]. The peaks at 1231 cm^{-1}, 1317 cm^{-1} and 1404 cm^{-1} were associated with the aromatic C–N stretching while the peaks at around 1533 cm^{-1} and 1628 cm^{-1} could be assigned to the existence of C=N [67]. The peak at 1684 cm^{-1} was C=O stretching [73]. The broad absorption band in the region of 3000-3500 cm^{-1} could be related to the N–H stretching of uncondensed amino groups and O–H bonds of the surface water [26,73]. Other unidentified peaks could originate from the impurities such as unreacted melamine or cyanuric acid. Figure 4.18(b) shows the spectra of C-550 and 0.12C-550. The spectra of 0.12C-550 was similar to that of C-550, suggesting that the chemical structure of 0.12C-550 remained unchanged after fabrication, corresponding to the XPS observation. Interestingly, a new peak at 2981 cm^{-1} appeared in 0.12C-550. The new peak was assigned to C-H bond [76,99-101]. As discussed in the previous sections, during the heat treatment, nickel reacted with released NH_3 and produces hydrogen: $6Ni+2NH_3 = 2Ni_3N+3H_2$ [28-31]. The appearance of C-H bond should be attributed to the chemical adsorption of hydrogen as results of the interaction of H_2 and 0.12C-500 at high temperature. Figure 4.20(c) shows the FTIR spectra of MWCNTs. The stretching vibration at 2844 and 2915 cm^{-1} could be assigned to symmetric and asymmetric stretching of C-H bond, the peak at 1637 cm^{-1} was the C=C skeleton stretching of MWCNTs and O-H from adsorbed water, the board peaks between 1540 cm^{-1} and 1570 cm^{-1} were C=O and C=C in aromatic rings, 1468 cm^{-1} and 1382 cm^{-1} were the stretching of sp^3 C-H [100,101,102,103,].

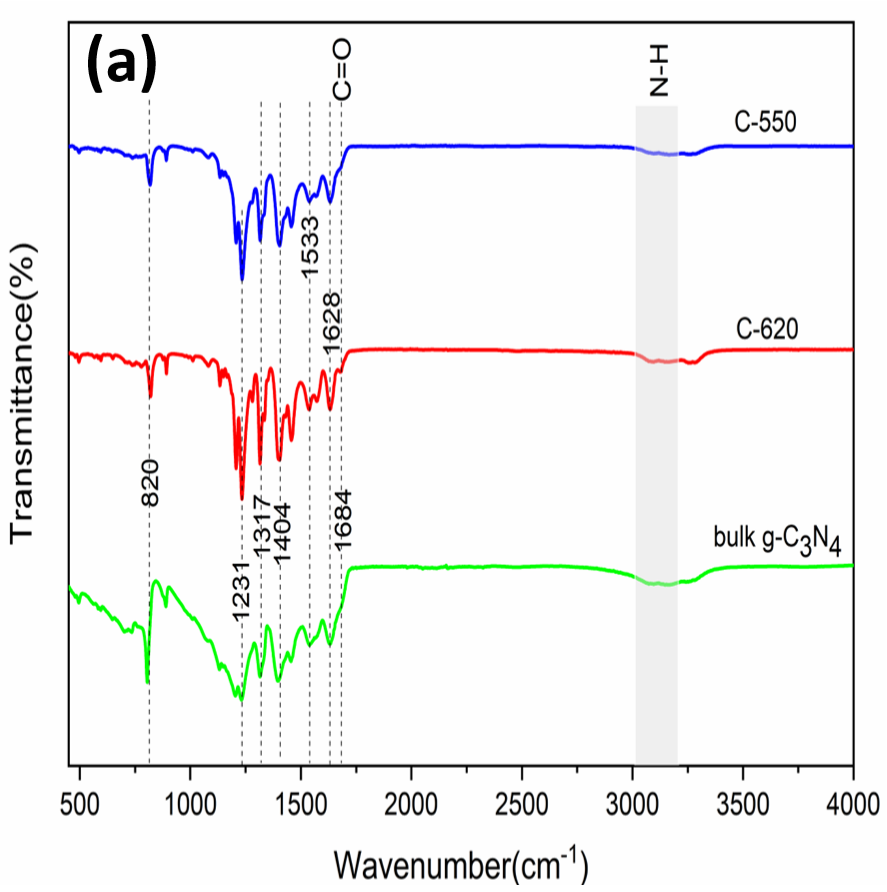
(a)
C=O
N-H
C-550
C-620
bulk g-C3N4
1533
1628
820
1317
1404
1684
1231
Transmittance(%)
500
1000
1500
2000
2500
3000
3500
4000
Wavenumber(cm-1)

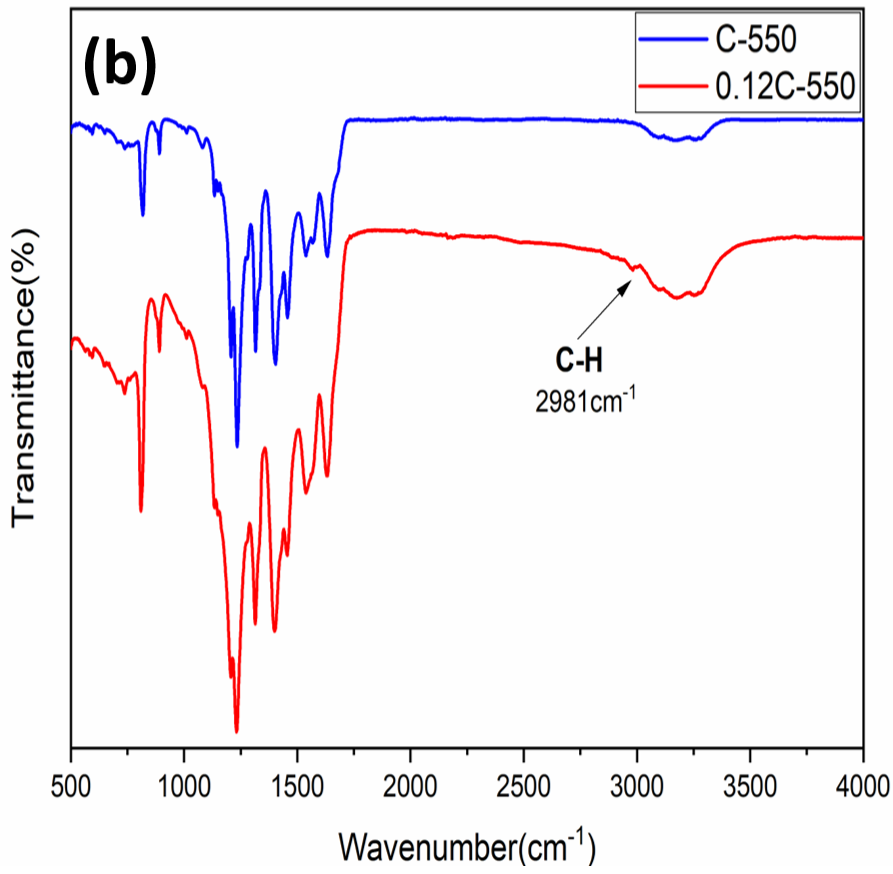
(b)
C-550
0.12C-550
C-H
2981cm-1
Transmittance(%)
500
1000
1500
2000
2500
3000
3500
4000
Wavenumber(cm-1)

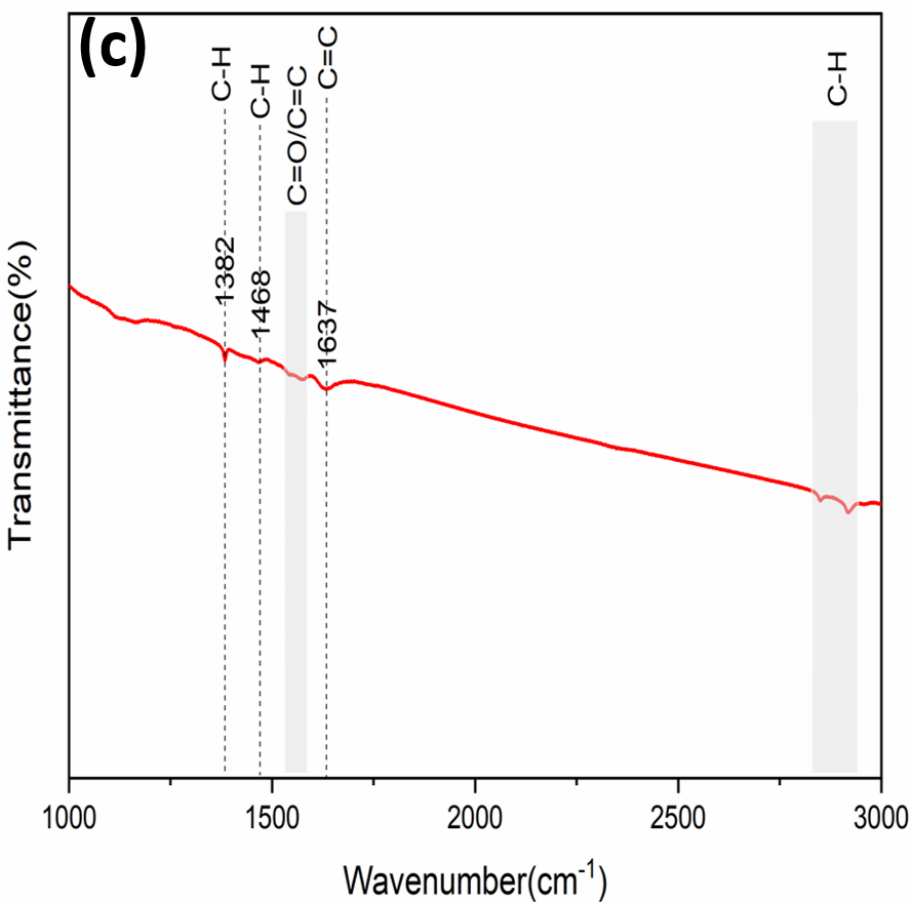

Figure 4.20. (a) FTIR spectra of bulk g-C_3N_4, C-550 and C-620. (b) FTIR spectra of 0.12Ni-550, the spectrum of C-550 is also attached for reference. (c) FTIR of MWCNTs.

4.7 Hydrogen Storage Characterization

The hydrogen adsorption and desorption isotherms are presented in Figures 4.21 (a), (b) and (c). The isotherms were obtained in the pressure range from 0 to 3.7 MPa, at room temperature (25 °C), 45 °C and 65 °C, respectively. The storage capacity increased with the increase in hydrogen pressure for all samples and reached the maximum value at 3.7 MPa. With the temperature increased from room temperature to 65 °C, the maximum hydrogen capacity decreased, which could be attributed to the increase of kinetic energy of gas molecules to encounter the barrier potentials [77]. C-550 and MWCNTs had similar surface area, but the storage capacity was much higher for C-550. It was also evident that MWCNTs had the small

storage capacity at 3.7 MPa in any temperature as compared with bulk g-C_3N_4, even if the surface area of bulk g-C_3N_4 was very small. C-620 possessed a high storage capacity as compared with bulk g-C_3N_4. That could be explained by the big specific surface area brought by the thin and highly porous structure, which provided more entry and reaction sites for hydrogen adsorption [104]. Interestingly, the capacity of C-620 was slight lower than the capacity of C-550, despite the fact that C-620 had a large specific surface area. Koh et al. studied the hydrogen storage performance of g-C_3N_4 nanotubes and g-C_3N_4 monolayer, they found the interaction between hydrogen and nanotubes was more stable than the interaction between hydrogen and monolayer [17]. Jhi et al. studied the hydrogen storage in BN nanotubes and BN nanosheets, they found the BN nanotubes possessed substantial buckling bonds which strongly interacted with hydrogen [105]. It was also reported that the curvature of carbon nanotubes could increase the binding energy [87]. Perhaps this could be the reason why C-620 did not hold hydrogen as much as C-550. Therefore, it is shown here that nanotube structure is more suitable for hydrogen storage than sheet structure. The theoretical storage capacity of g-C_3N_4 was 5.45 wt.% in Koh's research, which was far from the result obtained in this study [17]. One reason was the diameter of nanotubes. The nanotubes model that Koh et al. used in his calculation has a diameter of 0.8-2.3 nm, which was much smaller than that of C-550 (50-300 nm). The second reason was that the samples obtained here was impure. Lots of non-tubular structure (impurity) still remained in the sample after fabrication, as demonstrated in Figures 4.1(c-d). Therefore, future works such as the diameter reduction and purification of the g-C_3N_4 are needed to further improve the hydrogen storage performance.

The isosteric heat of adsorption (Q_{st}) can be a direct indicator of the interaction between hydrogen and adsorbent. In order to obtain Q_{st}, Clausius-Clapeyron equation: $Q_{st} = -R\,[\partial\,[\ln(P)]/\partial(1/T)]$ was applied [77], where R is the gas constant, P is the equilibrium pressure, T is the adsorption temperature. Here, the adsorption isotherms obtained at 25 °C and 45 °C were used for the calculation of Q_{st}. The range of 25 °C – 50 °C was chosen since it was the ideal temperature range for application, and the obtained adsorption heat during this range would be more meaningful. Figure 4.22 presents the adsorption heat of all g-C_3N_4 materials and MWCNTs. With the hydrogen uptake increased the adsorption heat decreased gradually, which could be explained by the gradual reduction of the number of available adsorption sites, which weakened the interaction between the sites and hydrogen [106]. All g-C_3N_4 materials possessed higher adsorption heat than MWCNTs did, suggesting the obtained high storage capacity of these g-C_3N_4 materials was due to the stronger interaction between these materials and hydrogen. The hydrogen adsorption heat in C-550 was found to be higher than those in C-620. This result is consistent with Kho's studies [1], which indicated graphitic carbon nitride nanotubes had a higher binding energy with hydrogen than sheets did. The relative low adsorption heat of bulk g-C_3N_4 might be also caused by the sheet-like aggregated surface as confirmed by TEM observation. Compared with MWCNTs which had very few hydrogen (0.05 wt.%) left, it should be noted that there was still lots of hydrogen (about 0.1-0.2 wt.%) left in g-C_3N_4 materials after desorption at the designated temperatures (Figure 4.21). The trapped hydrogen is likely chemisorbed on g-C_3N_4, as physisorbed hydrogen tends to have higher reversibility due to the weak Van der Waal force, while chemisorbed hydrogen is stable and would require extra energy to release [2].

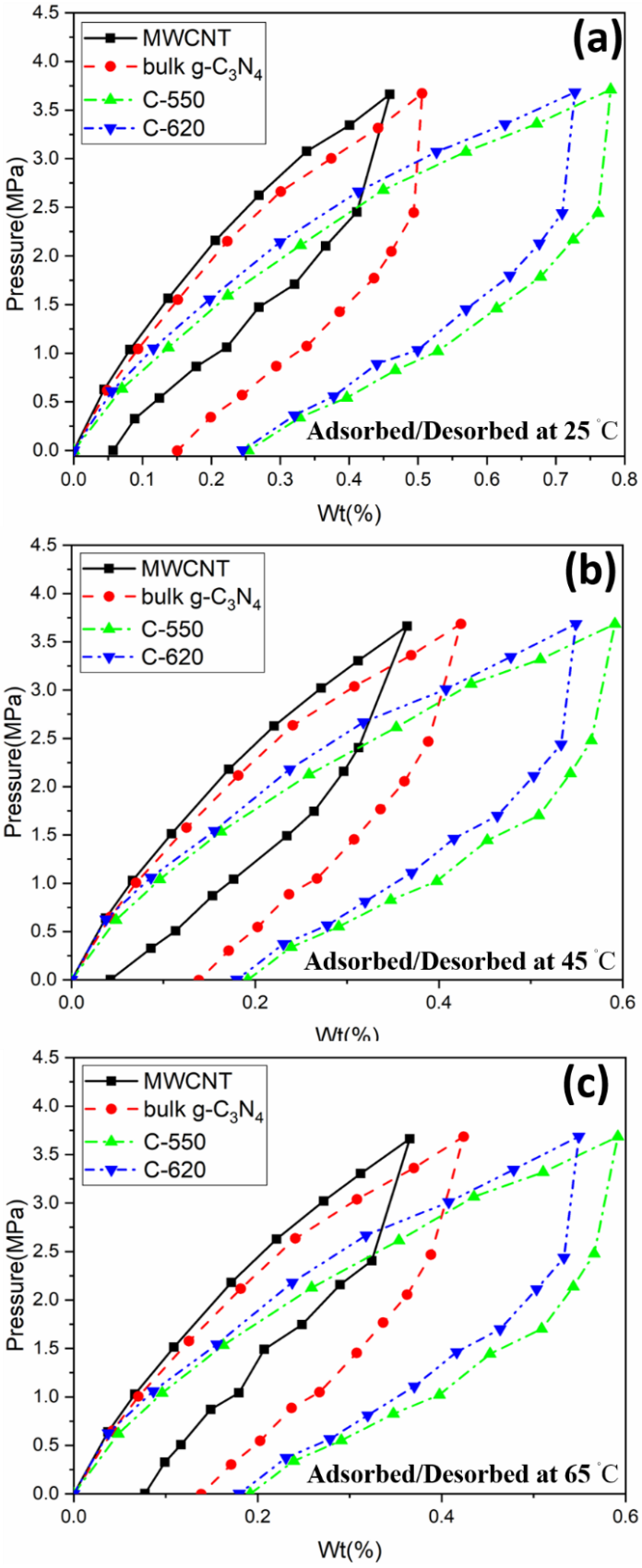

Figure 4.21. (a) (b) (c) Room temperature (25 ˚C), 45 ˚C and 65 ˚C hydrogen adsorption/desorption isotherms of MWCNTs, bulk g-C_3N_4, C-550 and C-620.

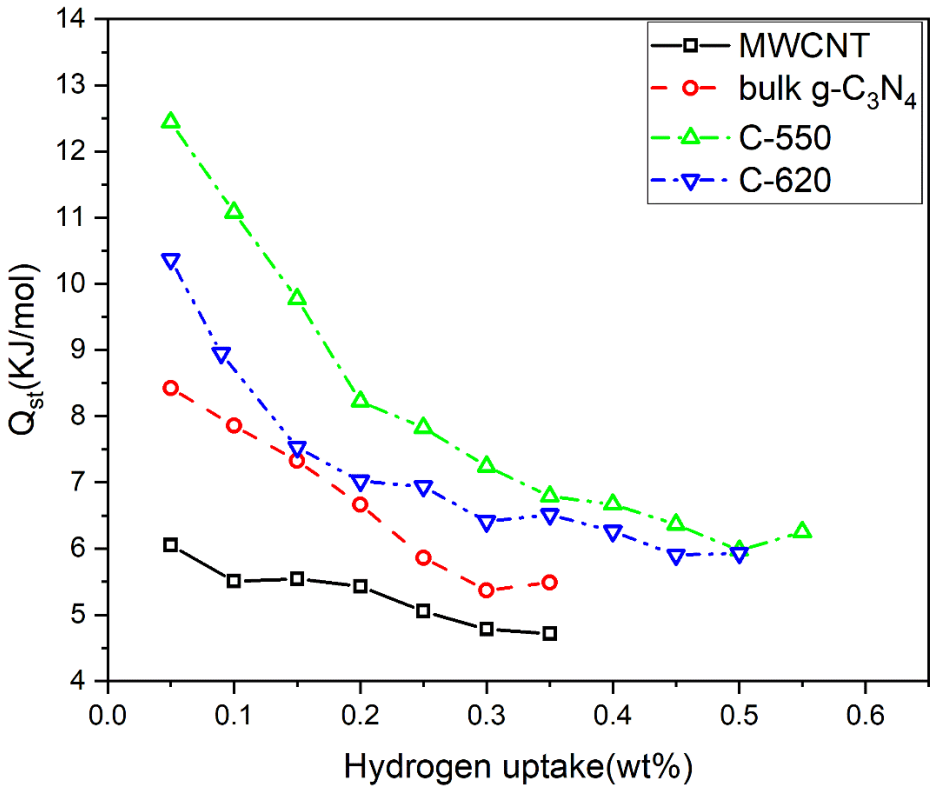

Figure 4.22. Isosteric heat of adsorption(Q_{st}) of g-C_3N_4 materials and MWCNTs.

Hydrogen storage test was also conducted on Ni- g-C_3N_4 nanotubes following the same procedures. The hydrogen adsorption/desorption isotherms of Ni- g-C_3N_4 nanotubes and C-550 are presented in Figure 4.23. The storage capacity increased with the pressure and reached the maximum value when the pressure was 3.7 MPa. The maximum capacity decreased with the increase of temperature. All nickel-assisted synthesis g-C_3N_4 nanotubes possessed larger storage capacities as compared with C-550 at all temperatures. With the amount of nickel used in the fabrication increased (from 0.01 to 0.12 g), the storage capactiy also increased. 0.12C-550 possesed the highest storage capacity at room temperature (25 $^{\circ}$C), which was 1.17 wt.%. Figure 4.24 shows the isosteric heat of adsorption (Q_{st}) of Ni-g-C_3N_4 nanotubes , the adsorption heat of C-550 is also attached for reference. The adsorption heats were much higher for these

nickel-assisted synthesis materials, suggesting that the high capacities obtained in Figrue 4.23 were attributed to the strong interaction between hydrogen and materials. According to the literature, defects and pores can provide strong sites for physisorption and enable chemisorption of hydrogen [107-110]. Tang et al. and Wu et al. studied the influence of defect on hydrogen storage performance of BN nanotubes, they found the dangling bonds at the defects could be strong sites for hydrogen chemisorption [111,112]. In this study, nickel reacted with released NH_3 and produced H_2, which generated water atmosphere with oxygen and triggered steam reforming etching on the samples. The etching created pores and defects (as confirmed by TEM observation and BET analysis) which provided lots of adsorption sites for hydrogen. Thus the adsorption heats were higher for Ni-g-C_3N_4 nanotubes . With more nickel used in the fabrication, more defects could be produced so the adsorption heats increased accordingly.

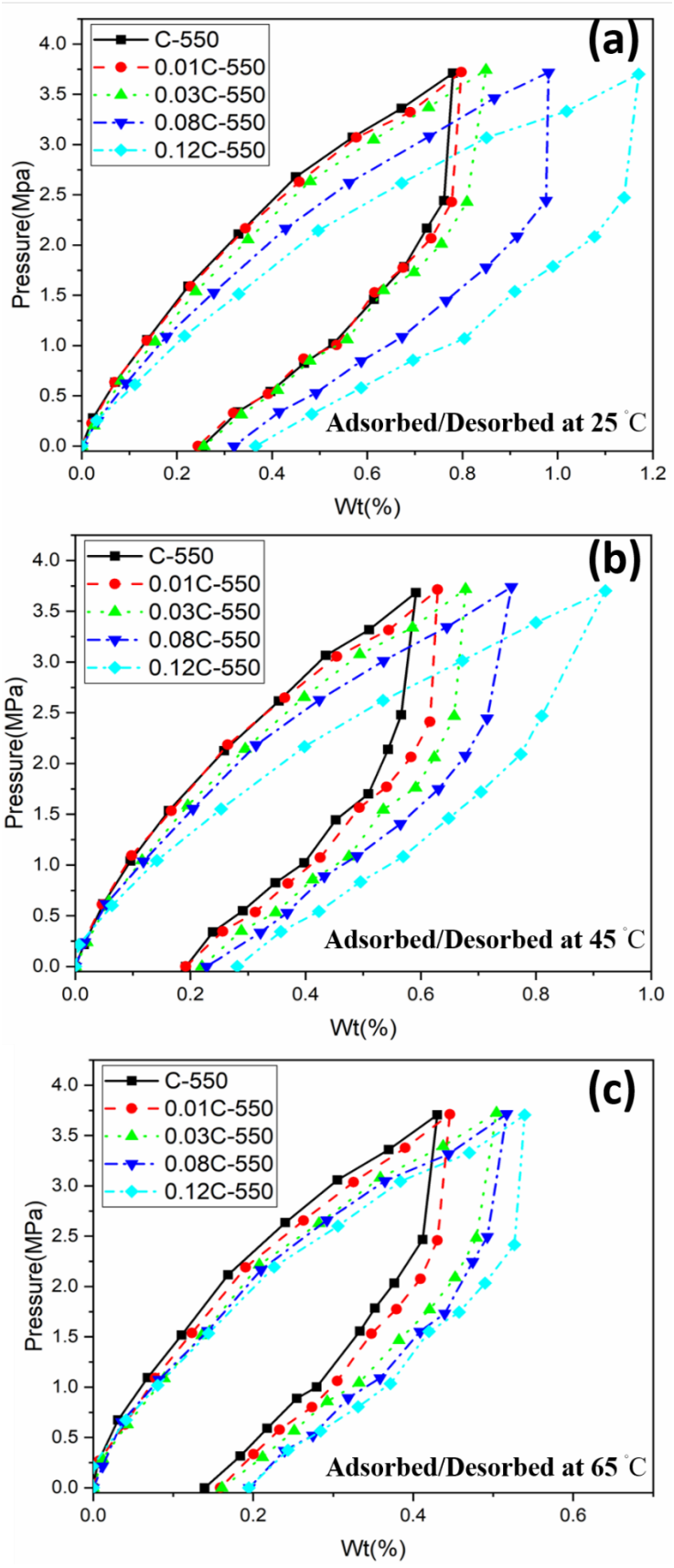

Figure 4.23. (a) (b) (c) Room temperature (25 ˚C), 45 ˚C and 65 ˚C hydrogen adsorption/desorption isotherms of Ni-g-C_3N_4 nanotubes .

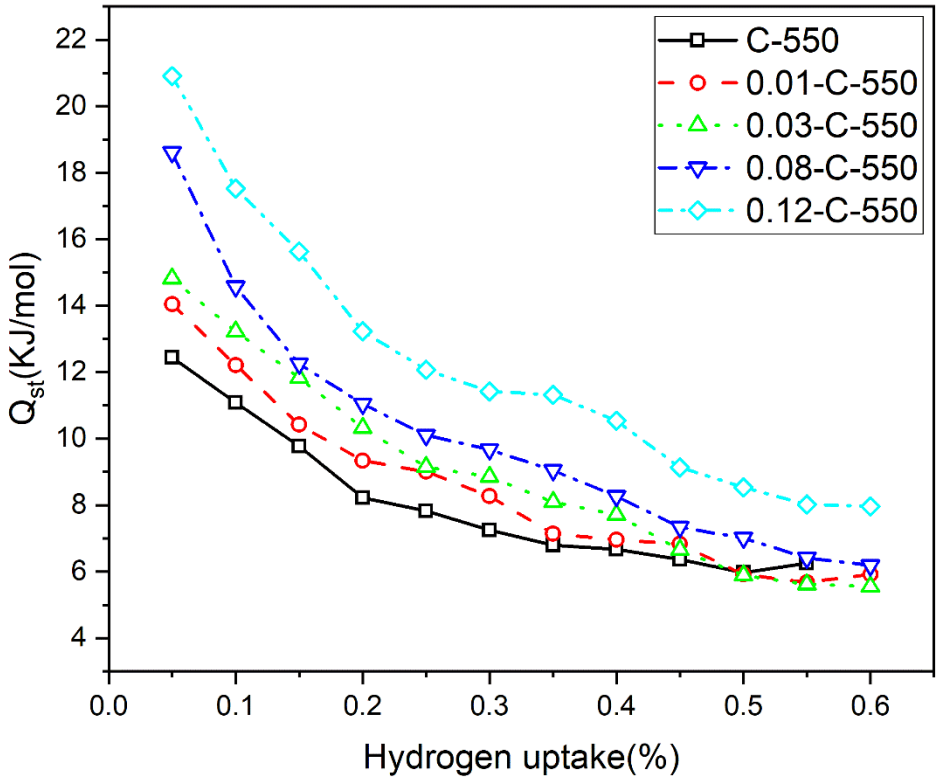

Figure 4.24. Isosteric heat of adsorption(Q_{st}) of Ni-g-C_3N_4 nanotubes , C-550's data are also attached for reference.

To further study hydrogen chemisorption behaviour of the carbonaceous materials in this work, Temperature Programmed Desorption (TPD) was applied. The whole procedures of the test could be found in Chapter 3. Normally, the samples were pre-charged with hydrogen at a certain temperature and pressure. Then the samples were purged with argon gas to remove physisorbed hydrogen. After purging, the samples were heated to release hydrogen. Since physisorbed hydrogen was removed in the purging process, any signal detected in the heat process should be attributed to the chemisorbed hydrogen.

In the TPD test, materials will desorb hydrogen and readsorb hydrogen at the same time, the desorption speed is increasing with the temperature since desorption is an activated process; However, with the removal of hydrogen from the materials, the rate reaches the maximum and then decreases with temperature [113]. That is why usually the desorption peak is recorded in the TPD curve. Materials may have several desorption peaks, corresponding to different adsorption sites (and hence adsorption energy) for hydrogen. The higher temperature the peak maximum locates, the higher is the binding energy between hydrogen and materials [113]. However, extra attention should be paid to the experiment parameters, especially the pumping speed or carrier gas flowing speed. Slow pumping speed or carrier gas flowing rate will cause a lag in the signals recorded and the desorption peak will shift to a higher temperature [114]. The reason is the large readsorption of hydrogen due to low pumping speed/carrier gas flowing rate [114]. Therefore, carrier gas flowing rate was carefully selected in this test to minimise readsorption as much as possible.

Figure 4.25 shows the TPD curves of MWCNTs, bulk g-C_3N_4, C-550 and C-620. For MWCNTs, the TPD signal was weak and no obvious desorption peak was detected suggesting little or no chemisorption occurred in MWCNTs. Thus, in MWCNTs hydrogen was adsorbed through weak physisorption, which could be removed easily during the purging process. However, strong signals were detected for g-C_3N_4 materials (bulk, C-620 and C-550), implying a significant amount of hydrogen chemisorption. Therefore, the great amount of unreleased hydrogen found in hydrogen storage test (Figure 4.21) should be attributed to the chemisorption of hydrogen. The board desorption curves of materials shows a complex, multi-step and energetically heterogenous desorption mode, clearly suggesting that these materials possessed heterogeneous surfaces and possessed more than one type of adsorption sites for hydrogen [113,115]. In addition, the peaks shifted to a higher temperature and became less pronounce if the materials were hydrogen-charged at higher temperature (65 $^{\circ}$C). The reason should be the

thermal motion of hydrogen at high temperature. If the charging was conducted at high temperature, the thermal motion of hydrogen with a high kinetic energy would break the bond between hydrogen and weak sites [116]. As a result, only strong adsorption sites at high temperature could adsorb hydrogen. That explains the right-shift of the peaks and the decrease in hydrogen intensity in Figure 4.25. The area under the TPD profile was proportional to the quantity of adsorbed hydrogen. The bigger the area, the more was the hydrogen chemisorbed by the materials. As the area under the TPD profile was the largest for C-550, followed by C-620 and bulk g-C_3N_4, it confirmed that C-550 chemisorbed the most hydrogen. In addition, the adsorbed hydrogen in C-620 and bulk g-C_3N_4 was mostly located at relatively weak adsorption sites (<150 $^{\circ}$C) while the adsorption mostly concentrates on strong adsorption sites (>150 $^{\circ}$C) in C-550, again suggesting the stronger adsorption in C-550. The area under the TPD spectra of C-620 was larger than the area of bulk g-C_3N_4 suggesting more chemisorbed hydrogen in C-620, which could be explained by the porous and high surface area structure of C-620 providing more adsorption sites for hydrogen [104].

TPD experiment was also conducted on 0.12C-550 Ni-g-C_3N_4 nanotubes . The TPD profile of C-550 is attached for comparison (Figure 4.26). As compared with C-550, the overall area under the TPD curve increased for 0.12C-550, suggesting more chemisorption occurred. The increased hydrogen was at relative weak adsorption sites (<170 $^{\circ}$C). However, a small decrease in adsorbed hydrogen at relative strong adsorption sites (>170 $^{\circ}$C) was noticed. Confirmed by TEM observation and BET surface analysis, 0.12C-550 possessed a highly porous structure created by steam reforming etching. The increasing chemisorbed hydrogen at weak adsorption sites (Figure 4.26) should be the hydrogen adsorbed at defects and pores. The etching might also destroy the structure of g-C_3N_4 nanotubes, and result in a reduction in the strong adsorptions sites. Hence, the adsorbed hydrogen at the strong sites reduced accordingly. The defects enabled the hydrogen chemisorption shift to relative weak adsorption sites, thus

the activation energy of desorption decreases, which then make hydrogen be desorbed easily in Ni-g-C_3N_4 nanotubes .

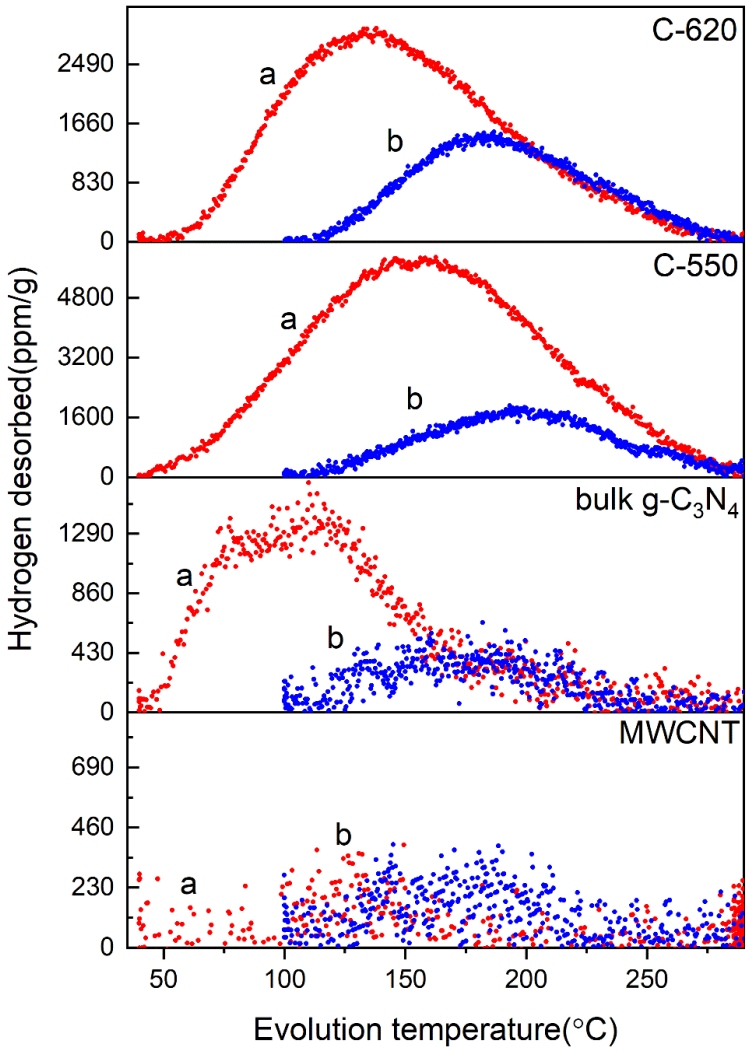

Figure 4.25. TPD curves of MWCNTs, bulk g-C_3N_4, C-550 and C-620 obtained after adsorbing hydrogen at (a) room temperature (25 ˚C) and (b) 65 ˚C.

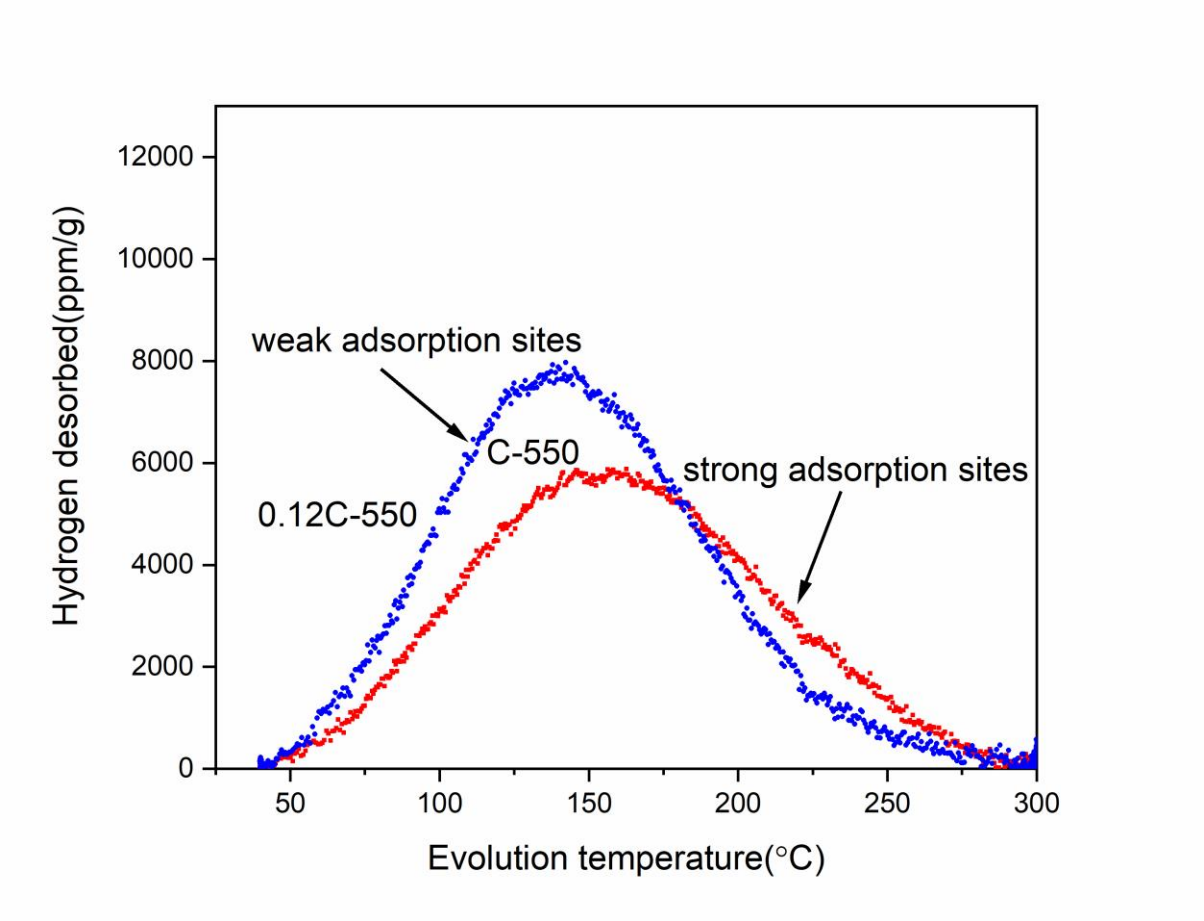

Figure 4.26. TPD curves of 0.12C-550 and C-550 obtained after adsorbing hydrogen at room temperature (25 ˚C).

The obtained high adsorption heats (Q_{st}) of g-C_3N_4 materials in Figure 4.22 were not only explained by chemisorption. Figure 4.27 presents the comparison of hydrogen storage ability of MWNCT and g-C_3N_4 materials. The red bars represent the desorbed hydrogen in hydrogen storage test which should be attributed to physisorption due to the weak bonding, while the blue bars represent the trapped and unreleased hydrogen which should be attributed to chemisorption because of stronger bonding [2]. Even if MWCNTs and C-550 have similar BET surface area and pore volume, C-550 still released more hydrogen than MWCNTs did at any temperature, clearly indicating more physisorption in C-550. The same result could also be found in the case of C-620. Possible due to the small surface area, bulk g-C_3N_4 did not possess

more physisorbed hydrogen at 25 °C and 45 °C. However, at high temperature of 65 °C, the amount of physisorbed hydrogen was more in bulk g-C_3N_4 than in MWCNTs. This could be a result of the stronger bonding between bulk g-C_3N_4 and hydrogen molecule and the strong bonding was not easy to break due to the thermal motion. Therefore, the high calculated adsorption heat (Figure 4.21) is partially ascribed to strong physisorption and partially ascribed to chemisorption. Both of them should be attributed to either nitrogen strengthens physisorption on carbon atoms and reduce energy barrier which enable chemisorption on carbon atoms [9-13,107,117], or the doubly bonded nitrogen itself provided strong sites for hydrogen physical and chemical adsorption [17]. Figure 4.28 shows the comparison of hydrogen storage ability of C-550 and nickel-assisted synthesis g-C_3N_4 nanotubes. Increase in trapped hydrogen (chemisorption) and desorbed hydrogen (physisorption) have been noticed. With the increase in nickel used in fabrication (0.01-0.12 g), the amount of physisorbed and chemisorbed hydrogen increased. Defects and pores do not just provide sites to enable chemisorption [109,111,112], but they also are strong sites for the physisorption [107-109,111]. Thus, both physisorption and chemisorption increase in Ni-g-C_3N_4 nanotubes as confirmed by hydrogen storage test (Figure 4.23) and TPD experiment (Figure 4.26). With more nickel was used in the fabrication, the etching effect becomes stronger and more pores and defects were created. Thenceforth, the adsorbed hydrogen increased accordingly.

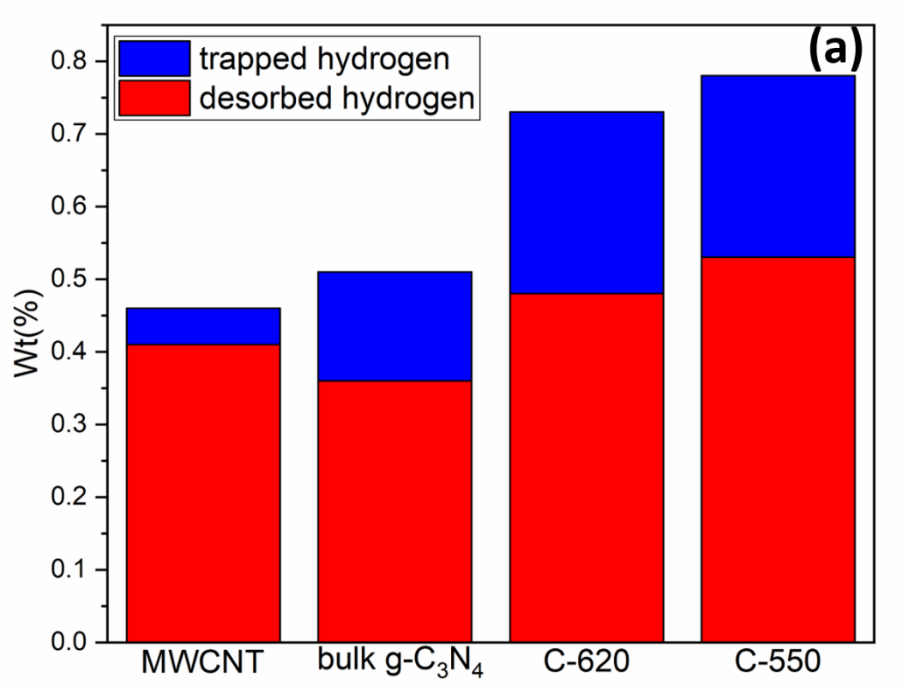
(a)
trapped hydrogen
desorbed hydrogen
Wt(%)
0.0
0.1
0.2
0.3
0.4
0.5
0.6
0.7
0.8
MWCNT
bulk g-C3N4
C-620
C-550

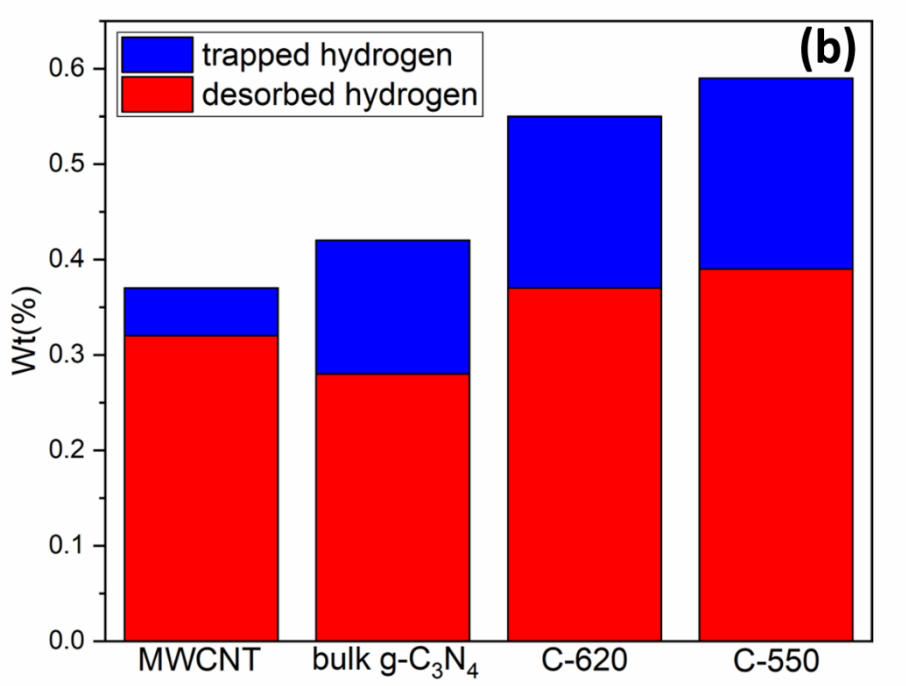
(b)
trapped hydrogen
desorbed hydrogen
Wt(%)
0.0
0.1
0.2
0.3
0.4
0.5
0.6
MWCNT
bulk g-C3N4
C-620
C-550

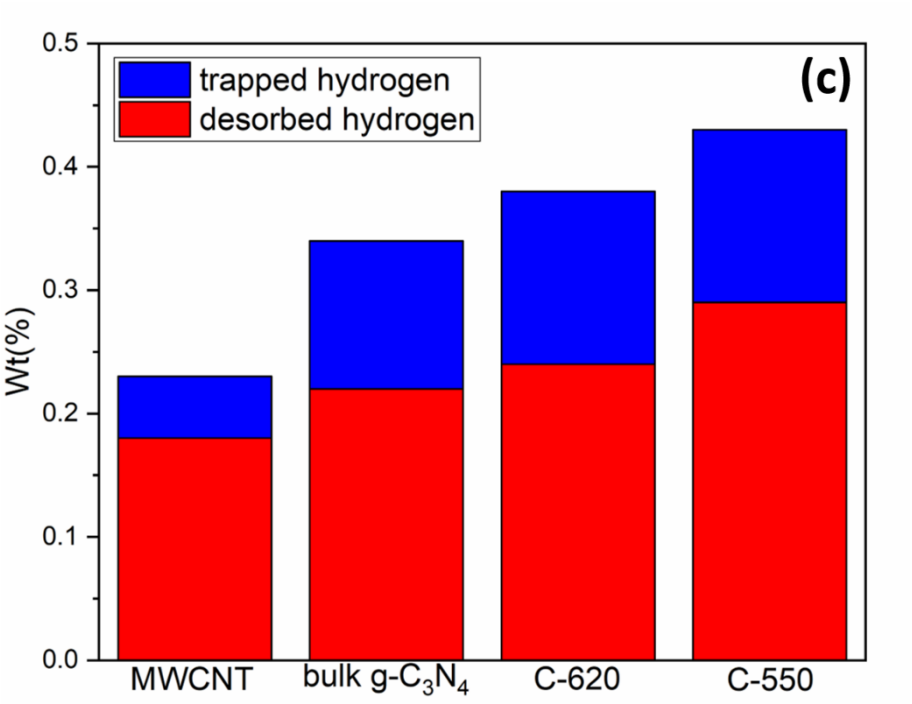

Figure 4.27. The comparison of hydrogen storage ability of MWCNTs and g-C_3N_4 materials obtained at (a) room temperature (25 ˚C), (b) 45 ˚C, (c) 65 ˚C. (The used data from figure 4.21)

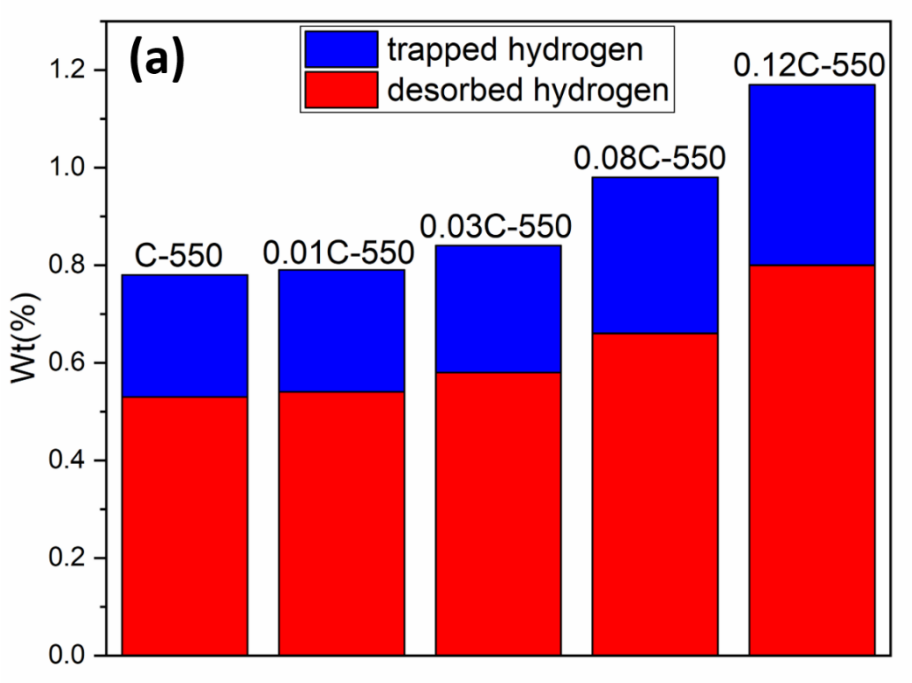

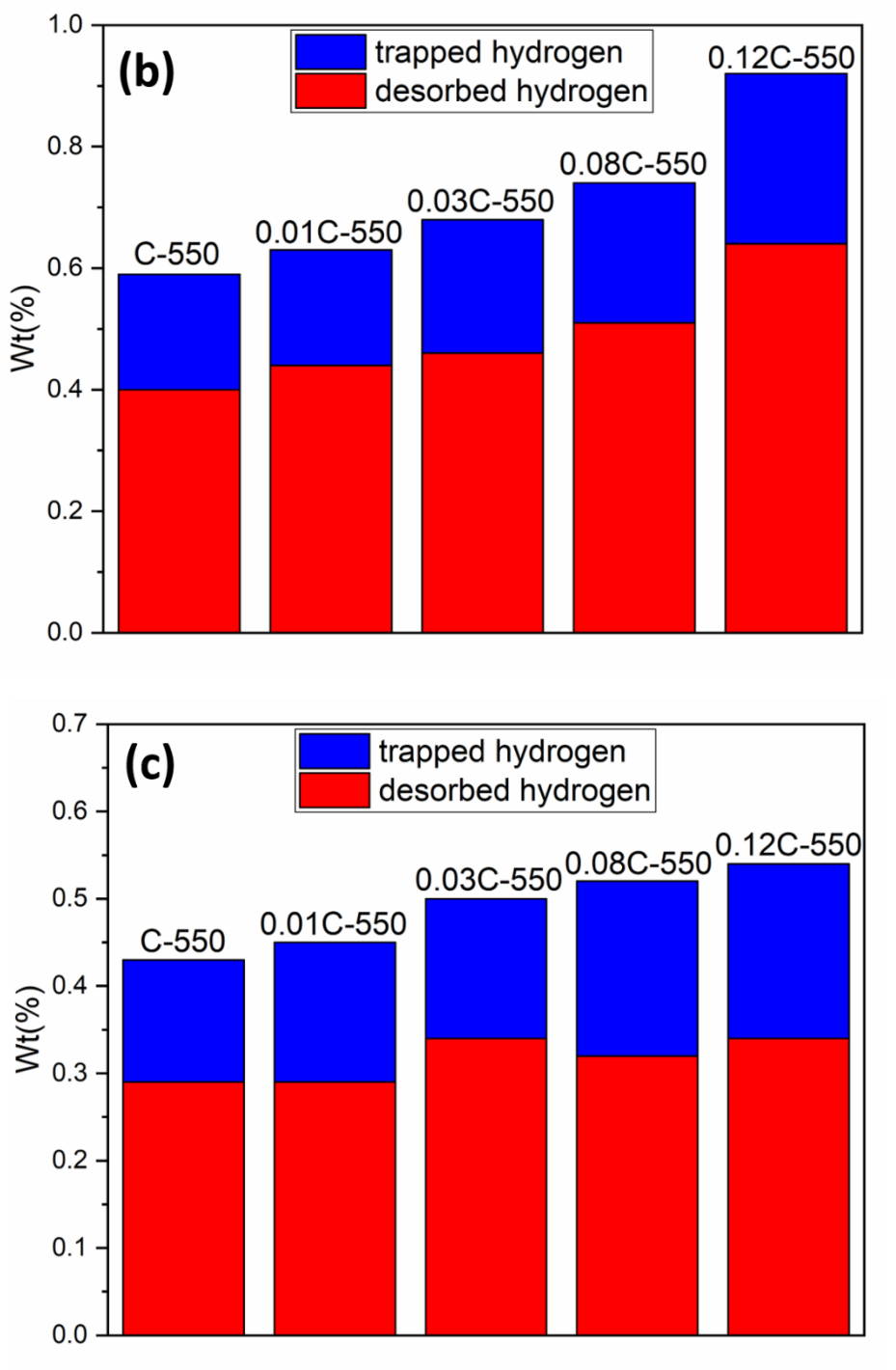

Figure 4.28. The comparison of hydrogen storage ability of C-550 and Ni-g-C_3N_4 nanotubes obtained at (a) room temperature (25 ˚C), (b) 45 ˚C, (c) 65 ˚C. (The used data from figure 4.23)

Chapter 5 Conclusion and Future Work

5.1 Conclusion

In this work, hydrogen storage materials g-C_3N_4 nanotubes were synthesised and studied. Multiwall carbon nanotubes (MWCNTs), g-C_3N_4 nanosheets and bulk g-C_3N_4 were also studied for comparison. The three g-C_3N_4 materials (nanotubes, nanosheets and bulk) had a similar chemical composition as confirm by FTIR and XPS, but the morphologies were different. The synthesised g-C_3N_4 nanotubes possessed a multiwall structure with the outer diameter of 50-400 nm, which was larger than the average diameter of MWCNTs (10 nm) studied here. However, the two materials had similar specific surface area (61.31 m^2/g for MWCNTs and 58.38 cm^3/g for g-C_3N_4 nanotubes) and pore volume (0.23 cm^3/g for both materials). Compared with MWCNTs which should have 100 % of the nanotube structure, the purity of g-C_3N_4 nanotubes was not high since lots of non-tube-like but bulk-like structure still could be observed. The obtained g-C_3N_4 nanosheets possessed a thin and highly porous structure, as the result g-C_3N_4 nanosheets had the highest specific surface area (161.02 m^2/g) and pore volume (0.43 cm^3/g). On the contrary, bulk g-C_3N_4 nanotubes had a bulk structure with considerable aggregation of g-C_3N_4 layers, so its specific surface area (10.98 m^2/g) and pore volume (0.06 cm^3/g) were the lowest.

For hydrogen storage, all g-C_3N_4 materials possessed a better performance in hydrogen storage test than MWCNTs. The room temperature (25 $^{\circ}C$) storage capacity obtained at under a hydrogen pressure of 3.7 MPa was 0.51 wt.% for bulk g-C_3N_4, which was higher than the capacity of MWNCTs (0.46 wt.%), even though the specific surface area and pore volume of the former were lower. Although the purity of g-C_3N_4 nanotubes was not as high as the purity of MWCNTs, but its storage capacity (0.78 wt.%) was still improved by up to 70 % as

compared with MWCNTs. The storage capacity of g-C_3N_4 nanosheets (0.73 wt.%) was also higher than the capacity of MWNCTs.

The isosteric heat of adsorption (Q_{st}) was calculated to study the strength of the interaction between hydrogen and materials. It was found that Q_{st} was higher for g-C_3N_4 materials than that of MWCNTs, suggesting the higher hydrogen capacity obtained was attributed to the strong interaction between materials and hydrogen. The strong interaction was believed to be due to nitrogen atoms which either strengthened the interaction between hydrogen and carbon atoms, or the doubly bonded nitrogen itself provided strong adsorption sites for hydrogen. In addition, Q_{st} of g-C_3N_4 nanotubes was higher than Q_{st} of g-C_3N_4 nanosheets and bulk g-C_3N_4, suggesting a much stabler bond with hydrogen in g-C_3N_4 nanotubes, which could be explained by the curvature of nanotube's surface which increased the adsorption energy. This finding explains the highest capacity of g-C_3N_4 nanotubes among the three g-C_3N_4 materials. TPD study further found a huge amount of chemisorbed hydrogen in g-C_3N_4 materials as compared with MWCNTs, implying that chemisorption should also play an important role in the great hydrogen storage performance of g-C_3N_4 materials in additional to the hydrogen physisorption.

In the second part of this research, nickel-assisted synthesis of g-C_3N_4 nanotubes was carried out and the hydrogen storage performance was examined. In the fabrication process, nickel decomposed and released NH_3, and the obtained H_2 after NH_3 decomposition generated water atmosphere, which triggered steam reforming etching on g-C_3N_4 nanotubes. Thus, highly porous structure of g-C_3N_4 nanotubes with high specific surface area and pore volume was obtained. XPS found the etching effect preferred to proceed with the loss of carbon then nitrogen. The loss of carbon occurred at graphitic carbon species and C-NH_x lattice sites while the loss of nitrogen occurred at N_3C and NH_x lattice sites. The as-synthesised materials had high hydrogen storage capacities as measure at three temperatures (room temperature (25 °C), 45 °C, 65 °C) and under a hydrogen pressure of 3.7 MPa. The storage capacity obtained at

room temperature for the nickel-assisted synthesised samples has promoted by up to 50 % (from 0.78 wt.% to 1.17 wt.%), as compared with g-C_3N_4 nanotubes synthesized without using nickel. As confirmed by hydrogen desorption study and TPD experiment, the increased capacity should be attributed to increased hydrogen physisorption and chemisorption, as extra adsorption sites provided by the created defects and pores were effective hydrogen storage sites.

5.2 Future work

Even if g-C_3N_4 nanotubes have excellence performances in hydrogen storage, the obtained materials' storage capacity was still far from the theorical value of 5.45 wt.% as obtained by first principal calculation. Two possible reasons can be proposed here: Firstly, the nanotubes fabricated were not very pure, lots of non-tube-like structure could still be observed. The second reason was that the specific surface area of g-C_3N_4 nanotubes was not very high, which should be attributed to the nanotubes' large diameter and the multiwall structure. It is recommended that the future work should focus on improving the structure of g-C_3N_4 nanotubes, such as increasing the purity, reducing the diameter, and reducing the aggregation of g-C_3N_4 layers on the wall to increase the specific surface area. Ni-g-C_3N_4 nanotubes was shown to possess a highly porous structure, which had the high storage capacity. So, nickel-based modification method is a promising way to create pores and defects on g-C_3N_4 nanotubes which then benefited hydrogen storage. However, its effect on the kinetics of the hydrogenation and dehydrogenation needs to be elucidated. It has been reported that materials with smaller pores had the higher hydrogen uptake and adsorption energy than the materials with the larger pores did [118]. Therefore, future work should also focus on improving this fabrication method by adjusting the fabrication parameters, like changing the amount and the size of nickel used, so as to create large number of fine pores and defects. In addition, metal doping was known as

an effective way to increase the hydrogen storage performance of carbon nanotubes owing to the hydrogen spillover effect of the metal particles [99,110]. It is interesting to see how metal particles other than nickel could influence the hydrogen storage performance of g-C_3N_4 nanotubes. Thus, metal doping on the hydrogen storage of g-C_3N_4 nanotubes is an area worth pursuing.

Reference

1.Schlapbach, L., & Züttel, A. (2011). Hydrogen-storage materials for mobile applications. In *Materials for sustainable energy: a collection of peer-reviewed research and review articles from nature publishing group* (pp. 265-270).

2.Ren, J., Musyoka, N. M., Langmi, H. W., Mathe, M., & Liao, S. (2017). Current research trends and perspectives on materials-based hydrogen storage solutions: a critical review. *international journal of hydrogen energy*, *42*(1), 289-311.

3.Sakintuna, B., Lamari-Darkrim, F., & Hirscher, M. (2007). Metal hydride materials for solid hydrogen storage: a review. *International journal of hydrogen energy*, *32*(9), 1121-1140.

4.Au, Y. S., Obbink, M. K., Srinivasan, S., Magusin, P. C., De Jong, K. P., & De Jongh, P. E. (2014). The Size Dependence of Hydrogen Mobility and Sorption Kinetics for Carbon-Supported MgH2 Particles. *Advanced Functional Materials*, *24*(23), 3604-3611.

5.Jia, Y., Cheng, L., Pan, N., Zou, J., Lu, G., & Yao, X. (2011). Catalytic De/Hydrogenation in Mg by Co-Doped Ni and VOx on Active Carbon: Extremely Fast Kinetics at Low Temperatures and High Hydrogen Capacity. *Advanced Energy Materials*, *1*(3), 387-393.

6.Adeniran, B., & Mokaya, R. (2015). Low temperature synthesized carbon nanotube superstructures with superior CO 2 and hydrogen storage capacity. *Journal of Materials Chemistry A*, *3*(9), 5148-5161.

7.Henwood, D., & Carey, J. D. (2007). Ab initio investigation of molecular hydrogen physisorption on graphene and carbon nanotubes. *Physical Review B*, *75*(24), 245413.

8.Mahdizadeh, S. J., & Goharshadi, E. K. (2019). Hydrogen storage on graphitic carbon nitride and its palladium nanocomposites: A multiscale computational approach. *International Journal of Hydrogen Energy*, *44*(16), 8325-8340.

9.Zhang, Z., & Cho, K. (2007). Ab initio study of hydrogen interaction with pure and nitrogen-doped carbon nanotubes. *Physical Review B*, *75*(7), 075420.

10.Sankaran, M., & Viswanathan, B. (2006). The role of heteroatoms in carbon nanotubes for hydrogen storage. *Carbon*, *44*(13), 2816-2821.

11.Reisi-Vanani, A., & Alihoseini, L. (2014). Computational investigation of the adsorption of molecular hydrogen on the nitrogen-doped corannulene as a carbon nano-structure. *Surface science*, *621*, 146-151.

12.Miwa, R. H., Martins, T. B., & Fazzio, A. (2008). Hydrogen adsorption on boron doped graphene: an ab initio study. *Nanotechnology*, *19*(15), 155708. 19.15 (2008): 155708.

13.Petrushenko, I. K. (2015). Structural and Mechanical Properties of Fluorinated SWCNTs: a DFT Study.

14.Gao, J., Zhou, Y., Li, Z., Yan, S., Wang, N., & Zou, Z. (2012). High-yield synthesis of millimetre-long, semiconducting carbon nitride nanotubes with intense photoluminescence emission and reproducible photoconductivity. *Nanoscale*, *4*(12), 3687-3692.

15.Wu, C., Zhu, X., Wang, C., Sheng, H., Yang, J., & Xie, Y. (2007). Bamboolike carbon nitride nanotubes (C 9 N 5 H 3): Atomic-scale construction, synthesis and lithium battery applications. *Applied physics letters*, *90*(11), 113116.

16.Irannejad, N., Rezaei, B., Ensafi, A. A., & Momeni, M. M. (2017). Enhanced efficiency of dye-sensitized solar cell by using a novel modified photoanode with platinum C3N4 nanotubes incorporated Ag/TiO2 nanoparticles. *Electrochimica Acta*, *247*, 764-770.

17.Koh, G., Zhang, Y. W., & Pan, H. (2012). First-principles study on hydrogen storage by graphitic carbon nitride nanotubes. *International journal of hydrogen energy*, *37*(5), 4170-4178.

18.Tong, Z., Yang, D., Sun, Y., Nan, Y., & Jiang, Z. (2016). Tubular g-C3N4 Isotype Heterojunction: Enhanced Visible-Light Photocatalytic Activity through Cooperative Manipulation of Oriented Electron and Hole Transfer. *Small*, *12*(30), 4093-4101.

19.Mo, Z., Xu, H., Chen, Z., She, X., Song, Y., Wu, J., Yan, P., Xu, L., Lei, Y., Yuan, S., & Li, H. (2018). Self-assembled synthesis of defect-engineered graphitic carbon nitride nanotubes for efficient conversion of solar energy. *Applied Catalysis B: Environmental*, *225*, 154-161.

20.Jin, Z., Zhang, Q., Yuan, S., & Ohno, T. (2015). Synthesis high specific surface area nanotube g-C 3 N 4 with two-step condensation treatment of melamine to enhance photocatalysis properties. *RSC Advances*, *5*(6), 4026-4029.

21.Li, K., Zeng, Z., Yan, L., Luo, S., Luo, X., Huo, M., & Guo, Y. (2015). Fabrication of platinum-deposited carbon nitride nanotubes by a one-step solvothermal treatment strategy and their efficient visible-light photocatalytic activity. *Applied Catalysis B: Environmental*, *165*, 428-437.

22.Cao, C., Huang, F., Cao, C., Li, J., & Zhu, H. (2004). Synthesis of carbon nitride nanotubes via a catalytic-assembly solvothermal route. *Chemistry of materials*, *16*(25), 5213-5215.

23.Bian, S. W., Ma, Z., & Song, W. G. (2009). Preparation and characterization of carbon nitride nanotubes and their applications as catalyst supporter. *The Journal of Physical Chemistry C*, *113*(20), 8668-8672.

24.Lee, J. W., Viswan, R., Choi, Y. J., Lee, Y., Kim, S. Y., Cho, J., Jo, Y., & Kang, J. K. (2009). Facile Fabrication and Superparamagnetism of Silica-Shielded Magnetite Nanoparticles on Carbon Nitride Nanotubes. *Advanced Functional Materials*, *19*(14), 2213-2218.

25.Zeng, Z., Li, K., Yan, L., Dai, Y., Guo, H., Huo, M., & Guo, Y. (2014). Fabrication of carbon nitride nanotubes by a simple water-induced morphological transformation process and their efficient visible-light photocatalytic activity. *RSC Advances*, *4*(103), 59513-59518.

26.Wang, X., Zhou, C., Shi, R., Liu, Q., Waterhouse, G. I., Wu, L., Tung, C., Zhang, T. (2019). Supramolecular precursor strategy for the synthesis of holey graphitic carbon nitride nanotubes with enhanced photocatalytic hydrogen evolution performance. *Nano Research*, *12*(9), 2385-2389.

27.Zhang, Y., Mori, T., & Ye, J. (2012). Polymeric carbon nitrides: semiconducting properties and emerging applications in photocatalysis and photoelectrochemical energy conversion. *Science of Advanced Materials*, *4*(2), 282-291.

28.Song, F., Li, W., Yang, J., Han, G., Liao, P., & Sun, Y. (2018). Interfacing nickel nitride and nickel boosts both electrocatalytic hydrogen evolution and oxidation reactions. *Nature communications*, *9*(1), 1-10.

29.Hu, S., Feng, C., Wang, S., Liu, J., Wu, H., Zhang, L., & Zhang, J. (2019). Ni3N/NF as bifunctional catalysts for both hydrogen generation and urea decomposition. *ACS applied materials & interfaces*, *11*(14), 13168-13175.

30.Gillot, F., Oró-Solé, J., & Palacín, M. R. (2011). Nickel nitride as negative electrode material for lithium ion batteries. *Journal of Materials Chemistry*, *21*(27), 9997-10002.

31.Zhang, B., Xiao, C., Xie, S., Liang, J., Chen, X., & Tang, Y. (2016). Iron–nickel nitride nanostructures in situ grown on surface-redox-etching nickel foam: efficient and ultrasustainable electrocatalysts for overall water splitting. *Chemistry of Materials*, *28*(19), 6934-6941.

32.Yang, P., Ou, H., Fang, Y., & Wang, X. (2017). A facile steam reforming strategy to delaminate layered carbon nitride semiconductors for photoredox catalysis. *Angewandte Chemie*, *129*(14), 4050-4054.

33.Fang, Z., Hong, Y., Li, D., Luo, B., Mao, B., & Shi, W. (2018). One-step nickel foam assisted synthesis of holey g-carbon nitride nanosheets for efficient visible-light photocatalytic H2 evolution. *ACS applied materials & interfaces*, *10*(24), 20521-20529.

34.Vegge, T., Sørensen, R. Z., Klerke, A., Hummelshøj, J. S., Johannessen, T., Nørskov, J. K., & Christensen, C. H. (2008). Indirect hydrogen storage in metal ammines. In *Solid-State Hydrogen Storage* (pp. 533-564). Woodhead Publishing.

35.http://peakoilbarrel.com/world-energy-2014-2050-part-3.[Accessed11 October 15].

36.Shafiee, S., & Topal, E. (2009). When will fossil fuel reserves be diminished? *Energy policy*, *37*(1), 181-189.

37.Ouyang, L. Z., Huang, J. M., Fang, C. J., Zhang, Q. A., Sun, D. L., & Zhu, M. (2012). The controllable hydrolysis rate for LaMg12 hydride. *international journal of hydrogen energy*, *37*(17), 12358-12364.

38.Rusman, N. A. A., & Dahari, M. (2016). A review on the current progress of metal hydrides material for solid-state hydrogen storage applications. *International Journal of Hydrogen Energy*, *41*(28), 12108-12126.

39.Demirbas, A. (2007). Storage and transportation opportunities of hydrogen. *Energy Sources, Part B*, *2*(3), 287-295.

40.http://www.motortrend.com/cars/toyota/mirai/2016/2016-toyota-mirai-first-drive [accessed 2017.10.26]

41.https://simanaitissays.com/2015/06/27/toyota-mirai-tidbits/ [accessed 2017.10.26].

42. Kalamaras, C. M., & Efstathiou, A. M. (2013). Hydrogen production technologies: current state and future developments. In *Conference papers in science* (Vol. 2013). Hindawi.

43.Ouyang, L. Z., Huang, J. M., Wang, H., Wen, Y. J., Zhang, Q. A., Sun, D. L., & Zhu, M. (2013). Excellent hydrolysis performances of Mg3RE hydrides. *International journal of hydrogen energy*, *38*(7), 2973-2978.

44.Thomas, G. (2000). Overview of storage development DOE hydrogen program. *Sandia National Laboratories*, *9*.

45.Abdalla, A. M., Hossain, S., Nisfindy, O. B., Azad, A. T., Dawood, M., & Azad, A. K. (2018). Hydrogen production, storage, transportation and key challenges with applications: A review. *Energy conversion and management*, *165*, 602-627.

46.LAVERSENNE, B. B. L. (2005). HYDROGEN STORAGE USING BOROHYDRIDES. *Entropy*, *184*, 183-3.

47.Boateng, E., & Chen, A. (2020). Recent advances in nanomaterial-based solid-state hydrogen storage. *Materials Today Advances*, *6*, 100022.

48.Chalk, S. G., & Miller, J. F. (2006). Key challenges and recent progress in batteries, fuel cells, and hydrogen storage for clean energy systems. *Journal of Power Sources*, *159*(1), 73-80.

49.Drive, U. S. (2015). Target explanation document: onboard hydrogen storage for light-duty fuel cell vehicles.

50.Principi, G., Agresti, F., Maddalena, A., & Russo, S. L. (2009). The problem of solid state hydrogen storage. *Energy*, *34*(12), 2087-2091.

51.Zlotea, C., & Latroche, M. (2013). Role of nanoconfinement on hydrogen sorption properties of metal nanoparticles hybrids. *Colloids and Surfaces A: Physicochemical and Engineering Aspects*, *439*, 117-130.

52.Stetson, N. (2012). An overview of US DOE's activities for hydrogen fuel cell technologies. *DOE office of energy efficiency and renewable energy (EERE). (ed^(eds)*.

53.Ouyang, L. Z., Dong, H. W., Peng, C. H., Sun, L. X., & Zhu, M. (2007). A new type of Mg-based metal hydride with promising hydrogen storage properties. *International journal of hydrogen energy*, *32*(16), 3929-3935.

54.Stroman, R. O., Schuette, M. W., Swider-Lyons, K., Rodgers, J. A., & Edwards, D. J. (2014). Liquid hydrogen

fuel system design and demonstration in a small, long endurance air vehicle. *International journal of hydrogen energy*, *39*(21), 11279-11290.

55.van den Berg, A. W., & Areán, C. O. (2008). Materials for hydrogen storage: current research trends and perspectives. *Chemical Communications*, (6), 668-681.

56.McWhorter, S., Read, C., Ordaz, G., & Stetson, N. (2011). Materials-based hydrogen storage: attributes for near-term, early market PEM fuel cells. *Current Opinion in Solid State and Materials Science*, *15*(2), 29-38.

57.Su, D. S., & Centi, G. (2013). A perspective on carbon materials for future energy application. *Journal of energy chemistry*, *22*(2), 151-173.

58.Yang, S. J., Jung, H., Kim, T., & Park, C. R. (2012). Recent advances in hydrogen storage technologies based on nanoporous carbon materials. *Progress in Natural Science: Materials International*, *22*(6), 631-638.

59.Murray, L. J., Dincă, M., & Long, J. R. (2009). Hydrogen storage in metal–organic frameworks. *Chemical Society Reviews*, *38*(5), 1294-1314.

60.Broom, D. P., Webb, C. J., Hurst, K. E., Parilla, P. A., Gennett, T., Brown, C. M., Zacharia, R., Tylianakis, E., Klontzas, E., Froudakis, G.E., Steriotis, Th.A., Trikalitis, P.N., Anton, D.L., Hardy, B., Tamburello, D., Corgnale, C., Van Hassei, B.A., Cossement, D., Chahine, R., & Hirscher, M. (2016). Outlook and challenges for hydrogen storage in nano porous materials. *Applied Physics A*, *122*(3), 151.

61.Zhou, L. (2005). Progress and problems in hydrogen storage methods. *Renewable and Sustainable Energy Reviews*, *9*(4), 395-408.

62.Gross, K. J., Thomas, G. J., & Jensen, C. M. (2002). Catalyzed alanates for hydrogen storage. *Journal of Alloys and Compounds*, *330*, 683-690.

63.Eigen, N., Kunowsky, M., Klassen, T., & Bormann, R. (2007). Synthesis of NaAlH4-based hydrogen storage material using milling under low pressure hydrogen atmosphere. *Journal of alloys and compounds*, *430*(1-2), 350-355.

64.Orimo, S. I., Nakamori, Y., Eliseo, J. R., Züttel, A., & Jensen, C. M. (2007). Complex hydrides for hydrogen storage. *Chemical Reviews*, *107*(10), 4111-4132.

65.Wang, L., & Yang, R. T. (2010). Hydrogen storage on carbon-based adsorbents and storage at ambient temperature by hydrogen spillover. *Catalysis Reviews*, *52*(4), 411-461.

66.Boudart, M., Vannice, M. A., & Benson, J. E. (1969). Adlineation, portholes and spillover. *Zeitschrift für Physikalische Chemie*, *64*(1_4), 171-177.

67.She, X., Xu, H., Xu, Y., Yan, J., Xia, J., Xu, L., Song, Y., Jiang, Y., Zhang, Q., & Li, H. (2014). Exfoliated graphene-like carbon nitride in organic solvents: enhanced photocatalytic activity and highly selective and sensitive sensor for the detection of trace amounts of Cu 2+. *Journal of Materials Chemistry A*, *2*(8), 2563-2570.

68.She, X., Xu, H., Wang, H., Xia, J., Song, Y., Yan, J., Xu, Y., Zhang, Q., Du, D., & Li, H. (2015). Controllable synthesis of CeO_2/gC_3N_4 composites and their applications in the environment. *Dalton Transactions*, *44*(15), 7021-7031.

69.Zhang, J., Zhang, M., Yang, C., & Wang, X. (2014). Nanospherical carbon nitride frameworks with sharp edges accelerating charge collection and separation at a soft photocatalytic interface. *Advanced Materials*, *26*(24), 4121-4126.

70.Zhu, Y., Feng, Y., Chen, S., Ding, M., & Yao, J. (2020). Carbon nitride nanotube-based materials for energy and environmental applications: a review of recent progresses. *Journal of Materials Chemistry A*.

71.Sung, S. L., Tsai, S. H., Tseng, C. H., Chiang, F. K., Liu, X. W., & Shih, H. C. (1999). Well-aligned carbon

nitride nanotubes synthesized in anodic alumina by electron cyclotron resonance chemical vapor deposition. *Applied physics letters*, *74*(2), 197-199.

72.Guo, Q., Xie, Y., Wang, X., Zhang, S., Hou, T., & Lv, S. (2004). Synthesis of carbon nitride nanotubes with the C 3 N 4 stoichiometry via a benzene-thermal process at low temperatures. *Chemical communications*, (1), 26-27.

73.Zhou, C., Shi, R., Shang, L., Wu, L. Z., Tung, C. H., & Zhang, T. (2018). Template-free large-scale synthesis of g-C 3 N 4 microtubes for enhanced visible light-driven photocatalytic H2 production. *Nano Research*, *11*(6), 3462-3468.

74.Jordan, T., Fechler, N., Xu, J., Brenner, T. J., Antonietti, M., & Shalom, M. (2015). "Caffeine doping" of carbon/nitrogen-based organic catalysts: Caffeine as a supramolecular edge modifier for the synthesis of photoactive carbon nitride tubes. *ChemCatChem*, *7*(18), 2826-2830.

75.Kim, S. Y., Kim, H. S., Augustine, S., & Kang, J. K. (2006). Nanopores in carbon nitride nanotubes: Reversible hydrogen storage sites. *Applied physics letters*, *89*(25), 253119.

76.Bai, X. D., Zhong, D., Zhang, G. Y., Ma, X. C., Liu, S., Wang, E. G., Chen, Y., Shaw, D. T. (2001). Hydrogen storage in carbon nitride nanobells. *Applied Physics Letters*, *79*(10), 1552-1554.

77.Nair, A. A., & Sundara, R. (2016). Palladium cobalt alloy catalyst nanoparticles facilitated enhanced hydrogen storage performance of graphitic carbon nitride. *The Journal of Physical Chemistry C*, *120*(18), 9612-9618.

78.Rostami, S., Nakhaei Pour, A., & Izadyar, M. (2019). Hydrogen adsorption by g-C3N4 and graphene oxide nanosheets. *Journal of Nanostructures*, *9*(3), 498-509.

79.Japanese Industrial Standards Committee. (2007). Method of measurement of pressure-composition-temperature (PCT) relations of hydrogen absorbing alloys. *JIS H 7201*.

80.Cui, Y., Zhang, J., Zhang, G., Huang, J., Liu, P., Antonietti, M., & Wang, X. (2011). Synthesis of bulk and nanoporous carbon nitride polymers from ammonium thiocyanate for photocatalytic hydrogen evolution. *Journal of materials chemistry*, *21*(34), 13032-13039.

81.Xu, H., Yan, J., She, X., Xu, L., Xia, J., Xu, Y., Huang, L., & Li, H. (2014). Graphene-analogue carbon nitride: novel exfoliation synthesis and its application in photocatalysis and photoelectrochemical selective detection of trace amount of Cu 2+. *Nanoscale*, *6*(3), 1406-1415.

82.Ma, T. Y., Dai, S., Jaroniec, M., & Qiao, S. Z. (2014). Graphitic carbon nitride nanosheet–carbon nanotube three-dimensional porous composites as high-performance oxygen evolution electrocatalysts. *Angewandte Chemie International Edition*, *53*(28), 7281-7285.

83.Cheng, F., Wang, H., & Dong, X. (2015). The amphoteric properties of g-C3N4 nanosheets and fabrication of their relevant heterostructure photocatalysts by an electrostatic re-assembly route. *Chemical communications*, *51*(33), 7176-7179.

84.Kamil, A. M., Hussein, F. H., Halbus, A. F., & Bahnemann, D. W. (2014). Preparation, characterization, and photocatalytic applications of MWCNTs/TiO2 composite. *International Journal of Photoenergy*, *2014*.

85.Liang, Q., Li, Z., Yu, X., Huang, Z. H., Kang, F., & Yang, Q. H. (2015). Macroscopic 3D porous graphitic carbon nitride monolith for enhanced photocatalytic hydrogen evolution. *Advanced Materials*, *27*(31), 4634-4639.

86.Zhao, W., Zhang, H., Liu, J., Xu, L., Wu, H., Zou, M., Wang, Q., He, X., Li, Y., & Cao, A. (2018). Controlled Air-Etching Synthesis of Porous-Carbon Nanotube Aerogels with Ultrafast Charging at 1000 A g− 1. *Small*, *14*(40), 1802394.

87.Züttel, A. (2003). Materials for hydrogen storage. *Materials today*, *6*(9), 24-33.

88.Cavenati, S., Grande, C. A., & Rodrigues, A. E. (2005). Separation of methane and nitrogen by adsorption on carbon molecular sieve. *Separation Science and Technology*, *40*(13), 2721-2743.

89.Li, Y., Jin, R., Xing, Y., Li, J., Song, S., Liu, X., Li, M., & Jin, R. (2016). Macroscopic foam-like holey ultrathin g-C3N4 nanosheets for drastic improvement of visible-light photocatalytic activity. *Advanced Energy Materials*, *6*(24), 1601273.

90.Niu, P., Zhang, L., Liu, G., & Cheng, H. M. (2012). Graphene-like carbon nitride nanosheets for improved photocatalytic activities. *Advanced Functional Materials*, *22*(22), 4763-4770.

91.Liu, J., Zhang, T., Wang, Z., Dawson, G., & Chen, W. (2011). Simple pyrolysis of urea into graphitic carbon nitride with recyclable adsorption and photocatalytic activity. *Journal of Materials Chemistry*, *21*(38), 14398-14401.

92.Wachowski, L., Sobczak, J. W., & Hofman, M. (2007). Speciation of functional groups formed on the surface of ammoxidised carbonaceous materials by XPS method. *Applied surface science*, *253*(9), 4456-4461.

93.Crunteanu, A., Charbonnier, M., Romand, M., Vasiliu, F., Pantelica, D., Negoita, F., & Alexandrescu, R. (2000). Synthesis and characterization of carbon nitride thin films obtained by laser induced chemical vapor deposition. *Surface and Coatings Technology*, *125*(1-3), 301-307.

94.Yu, H., Shi, R., Zhao, Y., Bian, T., Zhao, Y., Zhou, C., Waterhouse, G. I., Wu, L., Tung, C., & Zhang, T. (2017). Alkali-assisted synthesis of nitrogen deficient graphitic carbon nitride with tunable band structures for efficient visible-light-driven hydrogen evolution. *Advanced Materials*, *29*(16), 1605148.

95.Zhuge, G. Y., & Zhang, W. D. (2019). Boosting photocatalytic hydrogen evolution rate over carbon nitride through tuning its crystallinity and its nitrogen composition. *Journal of colloid and interface science*, *555*, 268-275.

96.Han, Q., Cheng, Z., Wang, B., Zhang, H., & Qu, L. (2018). Significant enhancement of visible-light-driven hydrogen evolution by structure regulation of carbon nitrides. *ACS nano*, *12*(6), 5221-5227.

97.Liu, J., Li, W., Duan, L., Li, X., Ji, L., Geng, Z., Huang, K., Lu, L., Zhou, L., Liu, Z., & Chen, W. (2015). A graphene-like oxygenated carbon nitride material for improved cycle-life lithium/sulfur batteries. *Nano letters*, *15*(8), 5137-5142.

98.Chen, L., Huang, H., Zheng, Y., Sun, W., Zhao, Y., Francis, P. S., & Wang, X. (2018). Noble-metal-free Ni 3 N/gC 3 N 4 photocatalysts with enhanced hydrogen production under visible light irradiation. *Dalton Transactions*, *47*(35), 12188-12196.

99.Kim, H. S., Lee, H., Han, K. S., Kim, J. H., Song, M. S., Park, M. S., Lee. J.Y., & Kang, J. K. (2005). Hydrogen storage in Ni nanoparticle-dispersed multiwalled carbon nanotubes. *The Journal of Physical Chemistry B*, *109*(18), 8983-8986.

100.McKenzie, D. R., McPhedran, R. C., Savvides, N., & Botten, L. C. (1983). Properties and structure of amorphous hydrogenated carbon films. *Philosophical magazine B*, *48*(4), 341-364.

101.Bahgat, M., Farghali, A. A., El Rouby, W. M. A., & Khedr, M. H. (2011). Synthesis and modification of multi-walled carbon nano-tubes (MWCNTs) for water treatment applications. *Journal of Analytical and Applied Pyrolysis*, *92*(2), 307-313.

102.Mungse, H. P., & Khatri, O. P. (2014). Chemically functionalized reduced graphene oxide as a novel material for reduction of friction and wear. *The Journal of Physical Chemistry C*, *118*(26), 14394-14402.

103.Stobinski, L., Lesiak, B., Kövér, L., Tóth, J., Biniak, S., Trykowski, G., & Judek, J. (2010). Multiwall carbon nanotubes purification and oxidation by nitric acid studied by the FTIR and electron spectroscopy methods. *Journal of Alloys and Compounds*, *501*(1), 77-84.

104.Li, Y., Zhao, D., Wang, Y., Xue, R., Shen, Z., & Li, X. (2007). The mechanism of hydrogen storage in carbon

materials. *International journal of hydrogen energy*, *32*(13), 2513-2517.

105.Jhi, S. H., & Kwon, Y. K. (2004). Hydrogen adsorption on boron nitride nanotubes: A path to room-temperature hydrogen storage. *Physical Review B*, *69*(24), 245407.

106.Chen, C. H., & Huang, C. C. (2009). Hydrogen adsorption in defective carbon nanotubes. *Separation and purification technology*, *65*(3), 305-310.

107.Wang, L., & Yang, R. T. (2009). Hydrogen storage properties of N-doped microporous carbon. *The Journal of Physical Chemistry C*, *113*(52), 21883-21888.

108.Zolfaghari, A., Pourhossein, P., & Jooya, H. Z. (2011). The effect of temperature and topological defects on H2 adsorption on carbon nanotubes. *International journal of hydrogen energy*, *36*(20), 13250-13254.

109.Li, J., Lin, J., Xu, X., Zhang, X., Xue, Y., Mi, J., ... & Zhang, J. (2013). Porous boron nitride with a high surface area: hydrogen storage and water treatment. *Nanotechnology*, *24*(15), 155603.

110.Aghababaei, M., Ghoreyshi, A. A., & Esfandiari, K. (2020). Optimizing the conditions of multi-walled carbon nanotubes surface activation and loading metal nanoparticles for enhanced hydrogen storage. *International Journal of Hydrogen Energy*, *45*(43), 23112-23121.

111.Tang, C., Bando, Y., Ding, X., Qi, S., & Golberg, D. (2002). Catalyzed collapse and enhanced hydrogen storage of BN nanotubes. *Journal of the American Chemical Society*, *124*(49), 14550-14551.

112.Wu, X., Yang, J., Hou, J. G., & Zhu, Q. (2006). Defects-enhanced dissociation of H_2 on boron nitride nanotubes. *The Journal of chemical physics*, *124*(5), 054706.

113.Leary, K. J., Michaels, J. N., & Stacy, A. M. (1988). Temperature‐programmed desorption: Multisite and subsurface diffusion models. *AIChE journal*, *34*(2), 263-271.

114.Madix, R. J. (1978). The application of flash desorption spectroscopy to chemical reactions on surfaces: Temperature programmed reaction spectroscopy. *Critical Reviews in Solid State and Material Sciences*, *7*(2), 143-152.

115.Sharma, H. N., Lenhardt, J. M., Loui, A., Allen, P. G., McLean, W., Maxwell, R. S., & Dinh, L. N. (2019). Moisture outgassing from siloxane elastomers containing surface-treated-silica fillers. *npj Materials Degradation*, *3*(1), 1-9.

116.Rakić, V., & Damjanović, L. (2013). Temperature-programmed desorption (TPD) methods. In *Calorimetry and thermal methods in catalysis* (pp. 131-174). Springer, Berlin, Heidelberg.

117.Wang, L., Yang, F. H., & Yang, R. T. (2009). Hydrogen storage properties of B‐and N‐doped microporous carbon. *AIChE journal*, *55*(7), 1823-1833.

118.Schmitz, B., Müller, U., Trukhan, N., Schubert, M., Férey, G., & Hirscher, M. (2008). Heat of Adsorption for Hydrogen in Microporous High-Surface-Area Materials. *ChemPhysChem*, *9*(15), 2181-2184.